Twisted light: Propagation properties and particle dynamics

Dissertation

zur Erlangung des akademischen Grades
Doktor rerum naturalium (Dr. rer. nat.)

vorgelegt der
Naturwissenschaftlichen Fakultät II
der Martin-Luther-Universität Halle-Wittenberg

von

Frau Anita Thakur

geboren am 30.04.1984 in Jalandhar City, Indien

angefertigt am Max-Planck-Institut für Mikrostrukturphysik
und an der Martin-Luther-Universität Halle-Wittenberg
in Halle an der Saale

Gutachterinen / Gutachter:

1. Prof. Dr. J. Berakdar
2. Prof. Dr. W. Hergert
3. Prof. Dr. H. A. Dürr

Halle an der Saale, den 12. September, 2012 verteidigt am 13. März, 2013

ABSTRACT

The present work examined the theoretical studies of nonlinear optical phenomena associated with light beams carrying orbital angular momentum which can be most realizable in the form of Laguerre Gaussian (LG) beams and also popularly dubbed as twisted light. The thesis is divided into two main parts. The first part explained the propagation properties of twisted light in a nonlinear medium. Under which, the self-focusing and defocusing of LG beams propagating in a nonlinear dielectric medium has been investigated. A differential equation for the beam width parameter is derived analytically as a function of the propagation distance, the angular frequency, the beam waist and the intensity of the beam utilizing the Wentzel-Kramers-Brillouin and the paraxial approximations. The predicted focusing and defocusing of LG beams can be used to manipulate the trapping spot size and the strength of the tweezers by crossing two LG beams at the focused distance. Next, the study on the transmission and the reflection of LG beams through a dielectric multilayer structure containing phase-conjugating interfaces has been demonstrated. Analytical expressions for the reflection and the transmission of the fields at individual layers are calculated. It is shown that the phase conjugation at the interfaces results in a characteristic angular and radial pattern of the reflected beam. These interference patterns have dependence on the thickness of the medium and can be varied on the scale of the incoming LG beam. This fact can be exploited in the field of characterization of refractive inhomogeneities in bulk optical materials. Whereas, the second part of the thesis focused on the particle dynamics in a focused, high intensity twisted light. It has been shown that the intensity distribution of twisted light results in the trapping, guiding and acceleration of neutral helium atoms to the centre of laser focus with a minimum intensity on axis via the ponderomotive potential, an effect which can be used for atom beam structuring and for lithographic applications.

Keywords: Orbital angular momentum, Laguerre Gaussian beam, Self-focusing, Wentzel-Kramers-Brillouin, Paraxial approximation, Phase conjugation, Refractive inhomogeneties, Ponderomotive potential.

ZUSAMMENFASSUNG

In der vorliegenden Arbeit werden nichtlineare optische Phänomene im Zusammenhang mit Licht, welches einen orbitalen Bahndrehimpuls besitzt, theoretisch untersucht. Dieses besondere Licht, auch bekannt unter dem Namen “twisted light (TL)”, wird meistens in Form von Laguerre-Gauß (LG) Lichtstrahlen realisiert. Die Arbeit ist in zwei Hauptteile gegliedert. Der erste Teil erläutert die Ausbreitungseigenschaften von TL in einem nichtlinearen Medium. Hier werden Selbst-Fokussierung und Defokussierung von TL Strahlen, welche sich in einem nichtlinearen dielektrischen Medium ausbreiten, untersucht. Eine Differentialgleichung für die Breite des Strahls als Funktion der Ausbreitungsstrecke, Kreisfrequenz, Strahltaille und der Intensität des Strahls wurde im Rahmen der Wentzel-Kramers-Brillouin und paraxialen Näherung analytisch hergeleitet. Die vorhergesagten Fokussierungs- und Defokussierungseffekte eignen sich hervorragend zur Manipulation der Größe und der Stärke von optischen Pinzetten, indem man zwei TL Strahlen kreuzt. Weiterhin wird die Transmission und Reflexion der LG Strahlen an einer dielektrischen mehrschichtigen Struktur bestehend aus phasenkonjugierenden Grenzflächen studiert. Dabei werden analytische Ausdrücke für die Reflexions- und die TransmissionsKoeffizienten hergeleitet. Es zeigt sich, dass die Phasenkonjugation an den Grenzflächen ein charakteristisches radiales Muster des reflektierten Strahls bewirkt. Diese Interferenzmuster stehen in Abhängigkeit zur Dicke des Mediums und können durch den einfallenden LG Strahl manipuliert genutzt werden. Dieser Effekt kann im Gebeit der Charakterisierung von lichtbrechenden Inhomogenitäten in optischen Materialien genutzt werden. Der zweite Teil der vorliegenden Arbeit konzentriert sich auf die Dynamik von Teilchen in einem fokussierten und sehr intensiven TL Strahl. Es wurde gezeigt, dass aufgrund des ponderomotiven Potenzials die Intensitätsverteilung von TL das Einfangen von neutralen Heliumatomen und eine gleichzeitige Beschleunigen dieser Atome hin zur Mitte des fokussierten Strahls, wo die Intensität minimal ist, bewirkt. Dieser Effekt könnte im Bereich der Atomstrahlstrukturierung und Lithographie Einsatz finden.

Schlagwörter: Optische Wirbel, Bahndrehimpuls, Laguerre-Gauß-Strahl, Selbst-Fokussierung, Wentzel-Kramers-Brillouin Näherung, paraxiale Näherung, Phasenkonjugation, Lichtbrechende Inhomogenitäten, ponderomotives Potenzial.

Dedicated

To

My Parents

My Teachers

&

Dear Friends

Contents

Abbreviations and Notations **xii**

1 Introduction **1**
1.1 Road map to this thesis 3

2 Introduction to Laguerre-Gaussian (LG) beams **5**
2.1 History of angular momentum of light 5
2.2 Laguerre-Gaussian (LG) beams 7
2.3 Applications of Laguerre-Gaussian (LG) beams 9
2.3.1 Optical manipulation 9
2.3.2 Quantum optics and quantum communication 11
2.4 Methods to generate twisted light 12
2.4.1 Spiral phase plate (SPP) 12
2.4.2 Diffractive optical elements (DOE) 14
2.4.3 Cylindrical lens mode convertors 16

3 Self-focusing and de-focusing of twisted light in non-linear media **21**
3.1 Basics of self-focusing 21
3.2 Mathematical background of self-focusing in dielectric media 24
3.2.1 Maxwell's equations 24
3.2.2 Propagation of EM waves in a linear isotropic medium 26
3.2.3 Propagation of EM waves through an inhomogeneous medium 27
3.3 Self-focusing of twisted light 28
3.3.1 Theoretical formulation 28
3.3.2 Results and discussion 32
3.3.3 Conclusions 35

4 Reflection and transmission of twisted light at phase conjugating interfaces **36**
4.1 Introduction to Optical phase conjugation (OPC) 36
4.2 Photo-refractive materials 39
4.3 Methods to produce phase conjugated waves (PCW) 41
4.3.1 Backward degenerate four wave mixing (DFWM) 41
4.3.2 Backward non-degenerate four wave mixing (NDFWM) . . . 42
4.3.3 Backward stimulated scattering (BSS) 43
4.4 Reflection and transmission of LG beams 46

4.4.1 Theoretical formulation 50
4.4.2 Results and discussion 53
4.4.3 Conclusions 57

5 Particle dynamics in twisted light **58**
5.1 Trajectory, acceleration and generation of magnetic field with twisted light 58
5.2 Dynamics of atoms and molecules in intense laser fields 62
5.2.1 Multi-photon ionization (MPI) 63
5.2.2 Above threshold ionization (ATI) 63
5.2.3 High harmonic generation (HHG) 65
5.3 Introduction to Optical trapping (OT) 66
5.3.1 Principle of optical trapping (OT) 67
5.3.2 Role of twisted light over Gaussian beams in optical tweezers (OT) 72
5.4 Optical trapping, guiding and acceleration of neutral atoms with twisted light 75
5.4.1 Results and discussion 76
5.4.2 Conclusions 80

6 Summary **81**

Appendix A: Reflection and transmission coefficients of twisted light **83**

Appendix B: Lagrangian equations of motion of the LG beam without Coulomb potential **87**

Appendix C: Lagrangian equations of motion of the LG beam with Coulomb potential **92**

Appendix D: Optical trapping of neutral atoms with the LG beam **97**

Bibliography **99**

Erklärung **110**

Acknowledgement **111**

Curriculum Vitae **113**

List of Publications **114**

Conference Contributions **115**

List of Figures

2.1 (a) The optical field structure of left and right circularly polarized beam, respectively. (b) The helical phase front of beams carrying different values of OAM (Here, propagation direction is indicated by a green arrow and regions of low and high intensity are denoted by red and yellow color respectively) 6

2.2 Intensity profiles of Laguerre-Gaussian beams with $p=0$ and (a) $\ell=0$, (b) $\ell=1$, (c) $\ell=2$, (d) $\ell=3$. The corresponding azimuthal phase is shown below the intensity profiles in (e), (f), (g) and (h), where the color chart shows the corresponding phase. Three dimensional representations of the phase fronts are shown in (i), (j), (k) and (l) with vertical propagation axis z 8

2.3 Schematic of a spiral phase plate (SPP) illuminated by a TEM_{00} beam and its outgoing wave i.e. Helical beam 14

2.4 The intensity density pattern of interference between two helical and a planar beam for several different values of the charge singularities . . 15

2.5 Beams generated by a sinusoidal pitch-fork hologram. A fraction of the power is diffracted on the first order and other part remains on the zeroth order. The topology of the hologram is objected to generate beams with $|\ell|=2$ 15

2.6 Different holograms pattern for the generation of a helical beam with $\ell=2$. (a) Sinusoidal, (b) Blazed, (c) Binary, and (d) Triangle holograms 16

2.7 Decomposition of the $LG_{0,1}$, $LG_{0,-1}$, $HG_{0,1}|_{@45^\circ}$ and $HG_{0,1}|_{@-45^\circ}$ modes in the HG basis 18

2.8 Schematic of the $\pi/2$ mode convertor. The distance between two cylindrical lenses is $\frac{f}{\sqrt{2}}$. The $\pi/2$ mode convertor converts diagonal $HG_{0,1}|_{@45^\circ}$ to $LG_{0,1}$, where f is the lens focal length 19

2.9 Schematic of the π mode convertor. The distance between two cylindrical lenses is $2f$. The π mode convertor converts $LG_{0,\ell}$ to $LG_{0,-\ell}$, where f is the lens focal length 19

3.1 Distortion of the wavefront of a laser beam (dashed curve) leading to self-focusing in a nonlinear medium. Here z_f is the self-focusing distance, defined as the distance between the position of self-focused spot (black dot) and the entrance face of the medium 22

3.2 Refraction ($\theta > \theta_c$) and total internal reflection ($\theta < \theta_c$) of rays in a nonlinear medium 23

3.3 a) Intensity (in CGS units) of the Gaussian beam (i.e. $\ell = 0$, and $p = 0$) verses the radial distance from the propagation direction (in cm). The angular frequency is $\omega = 2 \times 10^{14}$ rad/sec, $w_0 = 1$ cm, $\epsilon_0 = 1$, $\alpha = 1$, $E_0 = 0.3$ StatV/cm, $\rho = 0.66 \times 10^4$, b) Initial intensity profile (dotted curve) compared to the propagated intensity at $\xi = 4 \times 10^{-4}$. 32
3.4 a) Intensity (in CGS units) of the LG beam verses the radial distance from the propagation direction (in cm) for the $\ell = 1$, and $p = 0$. The angular frequency is $\omega = 2 \times 10^{14}$ rad/sec, $w_0 = 1$ cm, $\epsilon_0 = 1$, $\alpha = 1$, $E_0 = 0.3$ StatV/cm, $\rho = 0.66 \times 10^4$, b) Initial intensity profile (dotted curve) compared to the propagated intensity at $\xi = 4 \times 10^{-4}$. 33
3.5 a) Intensity (in CGS units) of LG beam verses the radial distance from the propagation direction (in cm) for the $\ell = 5$, and $p = 2$. The angular frequency is $\omega = 2 \times 10^{14}$ rad/sec, $w_0 = 1$ cm, $\epsilon_0 = 1$, $\alpha = 1$, $E_0 = 0.3$ StatV/cm, $\rho = 0.66 \times 10^4$, b) Initial intensity profile (dotted curve) compared to the propagated intensity at $\xi = 4 \times 10^{-4}$. 34

4.1 A comparison between reflection from a regular and phase conjugate mirror. 37
4.2 Reflection from a distorting glass in case of a regular mirror. 37
4.3 Reflection from a distorting glass in case of a phase conjugate mirror. . 38
4.4 Features of phase conjugating mirror (PCM) 38
4.5 Measured PC signal as a function of recording time 40
4.6 Backward phase conjugation wave generation by DFWM. 42
4.7 The generation of the backward non-degenerate PCW via partially degenerate FWM in a non-linear medium. 43
4.8 Experimental setup for observing phase conjugation behavior of backward stimulated scattering (BSS) 44
4.9 Normalized far field intensity distributions and photographs for the original pump beam, the aberrated pump beam, and the aberrated-corrected backward SBS beam 44
4.10 Schematic illustration of the non-degenerate FWM model for the phase formation of backward stimulated scattering 45
4.11 Comparison between a conventional mirror (M, bottom) and a wavefront reversal mirror (PCM, upper) from the point of view of angular momentum transformation in the photon's reflection 47
4.12 Interference pattern of the incident (pump) Gaussian mode wave E_p with field E_s reflected from a conventional mirror 48
4.13 Interference pattern of the incident 'right'(pump) first order LG wave E_p and phase conjugated 'right' replica E_s for a topological charge $\ell = +1$ 49
4.14 Interference pattern of $|m| = 2$ vortices (a,b) and $|m| = 3$ vortices (c,d). The left column shows a comparison between vortices reflected by a phase-conjugating mirror (left) and a conventional mirror (right). At the right column, both vortices are interfering, yielding a $2|m|$ multipole interference pattern 49

4.15 Schematic representation of the propagation of LG beam in a multi layer dielectric structure. The interfaces with PCM are indicated. . . . 50
4.16 For the structure depicted in Fig. 4.15 we show the calculated total radial (r) intensity (in CGS system) of the LG laser beam for a conventional mirror (Red curve), and a PCM (Dashed curve) in the medium 0 for $\ell = 1$, $p = 0$. The material parameters and laser properties are chosen as: $\phi = 30°$, $n_0 = 1$(air), $n_1 = 1.77$ (Al_2O_3), $n_2 = 1.457$ (SiO_2), $d_1 = 20\ \mu$m, $w_0 = 1\ \mu$m, $\lambda = 632.9$ nm. 53
4.17 For the structure depicted in Fig. 4.15 we show the calculated total radial (r) intensity (in CGS system) of the LG laser beam in the medium 0 for $\ell = 1$, $p = 0$ (a), and for $\ell = 10$, $p = 2$ (b). The material parameters and laser properties are chosen as: $\phi = 30°$, $n_0 = 1$(air), $n_1 = 1.77$ (Al_2O_3), $n_2 = 1.457$ (SiO_2), $d_1 = 20\ \mu$m, $w_0 = 1\ \mu$m, $\lambda = 632.9$ nm. . . . 54
4.18 The same as in Fig 4.17 for $\ell = 1$, $p = 0$ but here we show the angular (ϕ) distribution of the LG beam intensity (in CGS system) for a different thickness d_1 of the medium 1. The blue solid curve is for $d_1 = 11\pi\lambda/2$ and the dashed curve is for $d_1 = 4\pi\lambda$. The radial distance r is fixed to be $w_0/2$. 55
4.19 For the structure with additional one layer as depicted in Fig. 4.15 we show the calculated total radial (r) intensity (in CGS system) of the LG laser beam in the medium 0 (a) In case of $\ell = 1$, $p = 0$ for a conventional mirror (Red curve), and PCM (Dashed curve). (b) The total intensity of the LG beam in the medium 0 for $\ell = 10$, $p = 2$.The material parameters and laser properties are chosen as: $\phi = 30°$, $n_0 = 1$(air), $n_1 = 1.77$ (Al_2O_3), $n_2 = 1.457$ (SiO_2), $n_3 = 2.427$ ($BaTiO_3$),$d_1 = 20\ \mu$m, $d_1 = 30\ \mu$m w_0=1 μm, $\lambda = 632.9$ nm. (c) The angular (ϕ) distribution of the LG beam intensity for a different thicknesses d_1 and d_2 of the media 1 and 2 respectively. The blue solid curve corresponds for $d_1 = 11\pi\lambda/2$ and $d_2 = 13\pi\lambda/2$. The dashed curve is for $d_1 = 4\pi\lambda$ and $d_2 = 6\pi\lambda$. (d) The angular (ϕ) distribution of the LG beam intensity for a different thicknesses d_1 and d_2 of the media 1 and 2 respectively for $\ell = 5$, $p = 2$. The radial distance r is fixed to be $w_0/2$. 56

5.1 Trajectory of an electron in the LG beam with following parameters: $m_e = 9.1 \times 10^{-31}$kg, $w_0 = 1.05\ \mu$m, $\omega = 25.2 \times 10^{14}$ rad/s, $\phi_0 = 98.5°$, $E_0 = 0.6 \times 10^9$ V/m, $\ell = 1$, $p = 0$, $\mathbf{r}(t = 0) = (0.5\text{ nm}, 0, 0)$, $\dot{\mathbf{r}}(t = 0) = (10^6\text{ m/s}, 0, 0)$. 60
5.2 Acceleration of a charged particle in twisted light for the same parameters as in Fig. 5.1. The red and blue curve show the acceleration in ϕ and r direction respectively. 61
5.3 The magnetic field due to the LG beam for the same paramaters as in Fig. 5.1. 61

5.4 Case I: Tunneling ionization regime. Curve (a) shows the total potential energy U (x,t) of an atom in an intense laser field, the curve (b) represents the laser-electron interaction energy. Here, it shows that the laser field distorts the Coulomb potential. Case II: Multi-photon ionization regime. The figure shows the potential energy U (x) of an atom in presence of a weak external laser field. In this regime ($I < 10^{14}$ W/cm^2), the laser is not able to modify the Coulomb potential. Here, the arrows indicates that the ionization occurs through multi-photon absorption. Case III: OTBI regime. The curve (a) shows the potential energy U (x,t) of an atom in the presence of a strong external laser field, (b) represents the electron-laser interaction energy. In this regime ($I > 10^{15}$ W/cm^2), the ground state energy lies above the potential barrier. Here, in all the three cases, E_I and I are the ionization energy and the intensity of the field respectively. 62
5.5 Process of Multi-photon ionization (MPI): E_I is the ionization energy of the atom, E_e is the kinetic energy of the emitted electron and N, the number of photons at frequency(ω) absorbed. 64
5.6 A typical ATI process with the absorption of $(N + S)$ photons. S, the number of photons absorbed above the minimum number needed to overcome the ionization barrier. E_e, E_I are the electron energy emitted and the ionization energy respectively. 64
5.7 Process of three step model. 66
5.8 Single beam optical gradient force trap for a colloidal particle. Intensity gradients in the converging beam draw small objects, such as a colloidal particle, toward the focus, whereas the radiation pressure of the beam tends to blow them down the optical axis. Under conditions where the gradient force dominates, a particle can be trapped, in three dimensions, near the focal point 69
5.9 (1) Scattering force due to the radiation pressure, (2) Gradient force component of the radiation pressure, (3) Gradient force pulls the particle into the laser focus 70
5.10 Image (a) represents the Mie regime where the object is much larger than the laser wavelength (object size$> 10\lambda$). Image (b) represents the Lorentz-Mie regime where the object is approximately the same dimensions as the laser wavelength. Image (c) represents the Rayleigh regime where the object is much smaller than the laser wavelength (object size$< \lambda/20$). 71
5.11 Ray optics description of the gradient force (a) A transparent bead is illuminated by a parallel beam of light with an intensity gradient increasing from left to right, (b) The bead is illuminated by a focused beam of light with a radial intensity gradient to form a stable trap in three dimension. 71

5.12 Angular momentum transfer in optical tweezers. Rotation of a trapped object can be induced by (a), the transfer of spin angular momentum using a circular polarized beam or (b), the transfer of orbital angular momentum using a beam such as high order Laguerre-Gaussian or Bessel beam 73
5.13 Reversal of rotation of absorbing polystyrene spheres trapped in a helical beam 73
5.14 Relevant coordinates for a Rydberg atom immersed in an applied optical field. 76
5.15 Trajectory of an electron in the LG beam with Coulomb potential for following parameters: $m_e = 9.1 \times 10^{-31}$kg, $w_0 = 1.05\ \mu$m, $\omega = 25.2 \times 10^{14}$ rad/s, $\phi_0 = 98.5^\circ$, $E_0 = 0.7 \times 10^8$ V/m, $\ell = 1$, $p = 0$, $\mathbf{r}(t = 0) = (0.5\text{ nm}, 0, 0)$, $\dot{\mathbf{r}}(t = 0) = (10^6\text{ m/s}, 0, 0)$. 78
5.16 Dynamics of a neutral He atom in the LG beam for different initial conditions. (a) Ponderomotive potential of LG_0^1 mode (blue curve) and LG_2^1 mode (dashed curve) with the following parameters: M(He atom) = 6.68×10^{-27}kg, $w_0 = 16\ \mu$m, $\omega = 28.96 \times 10^{14}$ rad/s ($\lambda = 650$ nm), $E_0 = 5.3 \times 10^7$ V/m; (b) The neutral atom resides initially at $\mathbf{R}(t = 0) = 10\ \mu$m, $\dot{\mathbf{R}}(t = 0) = 0$ m/s for $\ell = 1$, $p = 0$ (black curve), $\ell = 1$, $p = 2$ (dashed red curve); (c) Scattering of atom at $\mathbf{R}(t = 0) = 30\ \mu$m, $\dot{\mathbf{R}}(t = 0) = 0$ m/s (indicated with the red curve) and with $\dot{\mathbf{R}}(t = 0) = 40 \times 10^3$ m/s (indicated with the dot-dashed curve). 79

A.1 Schematic representation of the propagation of LG beam in a multi layer dielectric structure. The interfaces with PCM are indicated. . . . 83

List of Tables

2.1 Ideal efficiency of different types of grating and different kind of holograms 16
2.2 Comparison of LG_p^ℓ beam characteristics using different generation methods of twisted light 20

4.1 Photorefractive materials and their characteristics. 39
4.2 Representative choices of wavelengths, corresponding CdS_xSe_{1-x} glasses, and third-order susceptibilities measured by DFWM 41

Abbreviations and Notations

Refractive index	n
Critical power	P_{cr}
Susceptibility	χ
Wavelength	λ
Speed of light	c
Free charge density	ρ
Free current density	$\mathbf{J}$
Electric field	$\mathbf{E}$
Magnetic field intensity	$\mathbf{H}$
Dielectric function	ε
Magnetic permeability	μ
Wave-vector	k
Frequency	ω
Azimuthal index or Winding no. or Topological charge	ℓ
Beam waist	w_0
Radial index	p
Eikonal	S
Radial coordinate	r
Azimuthal coordinate	ϕ
Rayleigh range	z_R
Ponderomotive force	F_{pond}
Ponderomotive potential	U_p
Electric charge	e
Mass of particle	m
Gradient force	F_{grad}
Scattering force	F_{scat}
Scattering power	P_{cr}
Tunneling time	T_{tun}
Laser period	T_L
Ionization energy	E_I
Planck constant	$\hbar$
Normalization constant	$C_p^{\lvert\ell\rvert}$

Wentzel-Kramers-Brillouin	WKB
Paraxial ray approximation	PRA
Electromagnetic	EM
Spiral phase plate	SPP
Spontaneous parametric down conversion	SPDC
Hermite-Gaussian	HG
Over the barrier ionization	OTBI
Intensity	I
Optical vortex tweezer	OVT
Multi-photon ionization	MPI
Above threshold ionization	ATI
High harmonic generation	HHG
Optical trapping or Optical tweezers	OT
Transverse electromagnetic	TEM
Orbital angular momentum	OAM
Optical phase conjugation	OPC
Conduction band	CB
Lithium niobate	$LiNbO_3$
Lithium tantalate	$LiTaO_3$
Potassium tantalate niobate	$KTa_{1-x}Nb_xO_3$
Bismuth silicon oxide	$Bi_{12}SiO_{20}$
Bismuth germanium oxide	$B_{12}GeO_{20}$
Gallium asenide	GaAs
Indium phosphide	InP
Phase conjugated wave	PCW
Degenerate four wave mixing	DFWM
Four wave mixing	FWM
Stimulated Brillouin scattering	SBS
Backward stimulated scattering	BSS
Helium	He
Laguerre-Gaussian	LG

If any notation differs from the above given list, then it would be stated separately in the following text.

Chapter 1

Introduction

Over the years, scientists have used the properties of light in a variety of disciplines to investigate various applications in biological and non-biological fields. It is a well known fact that light beams carries energy and both, linear and angular momentum. The total angular momentum can contain a spin contribution associated with light polarization, and an orbital contribution associated with the spatial and phase structure of the light. Although, both forms of angular momentum have been identified in electromagnetic theory for many years, it is only over the past decade that the orbital angular momentum (OAM) has drawn a major attention and became the subject of intense theoretical and experimental studies. Usually laser beams consists of spherical wavefronts whereas the light beams carrying orbital angular momentum i.e. Laguerre-Gaussian (LG) beam with helical wavefronts looks very different; its intensity profile consists of a ring of light as a result of the beam's particular phase profile. The profiles of the light beams carrying OAM can be twisted like a corkscrew about the axis of propagation and have zero intensity at their center, hence also dubbed as **twisted light (TL)**. For these helically phased beams, the Poynting vector has an azimuthal phase dependence of $\exp(-i\ell\phi)$ where ϕ is the azimuthal coordinate in the beam's cross-section and ℓ is the topological charge or winding number which can take any integer value either positive or negative. Thus, it is also called an optical vortex (OV) which represents the number of times the light twists in one wavelength. The higher this number, the faster the light spins around its axis and the larger the dark region at the center of the beam becomes. Wave dislocations and singularities were first explored by Nye and Berry in 1973 [1] and optical vortices were experimentally realized optically as carrying orbital angular momentum in the early 1990's [2–4].

The beams with helical wavefronts are shown to have OAM, much like circularly polarized light has spin angular momentum (SAM) which can be transferred to matter. The amount of OAM, a beam of light carries is proportional to how much the phase gradient of the light varies. Experimentally, the light beams with both spin and orbital angular momentum can be realized. In 1936, Beth [5] showed that the circular polarization of light is associated with SAM, when a birefringent plate was made to rotate by hitting with the circularly polarized light. Whereas, Allen et al. demonstrated the use of cylindrical lens to convert Hermite-Gaussian (HG) modes into LG modes and

showed experimentally that the intrinsic (SAM) and the extrinsic (OAM) nature of the light's angular momentum behaved differently. As the transfer of SAM to the particle results into the spinning rotation of the particle around its own axis, the transfer of OAM results into the orbital rotation of the particle around the beam axis. Unlike SAM, which has only two independent states (i.e. left and right circular polarization), OAM has an unlimited states corresponding to the integer value of ℓ. Thus, make it useful at both the classical and quantum levels. Still, a number of possible studies with useful applications using the OAM nature of light have yet to be exploited.

Various theoretical and experimental aspects of light beams that have angular momentum in linear and non-linear optics have been explored. In context to nonlinear optics, the major subject is related to the refractive index change by induced intense laser beam as well as the impact of this change on the laser beam itself. This self-action effect of the laser beam known as self-focusing. Immediately, after the consideration of the self-focusing process by Askar'yan [6] in 1962, it attracted a great deal of attention particularly using the LG mode due to its interesting spatial structure which will be reported in this thesis. The another important area is related to the studies of optical phase conjugation (OPC). In 1972, a Russian researcher reported the experimental observation of wavefront reversal property of backward stimulated Brillouin scattering [7] and soon after this experimental study, it was realized that OPC techniques are quite useful for many special applications, such as the high brightness lasing, the abberation compensation in a disturbing propagation medium, the real time optical holographic wavefront reconstruction, and the optical data storage and processing. Since then the process of OPC draw a major attention and consequently many studies have been carried out both at theoretical and experimental levels. Recently, the realization of OPC has been made using the LG beams by Okulov [8] and Denz [9] experimentally where they investigated OPC using the method of stimulated Brillouin scattering (SBS) and degenerated four wave mixing (DGFW) respectively where only single phase conjugated mirror (PCM) layer is taken into consideration. Whereas, in our work, we have considered the multilayered structure with phase conjugating interfaces which results in characteristic angular and radial pattern of the reflected beam, a fact that can be exploited for the detection and the characterization of phase conjugation in composite optical materials. The another major advantage of the LG beams can also be seen in the improvement of "Optical tweezers" set ups, where small objects are trapped and moved with the help of focused laser beams. The unique capability of the light with OAM, to rotate the trapped particle has found numerous applications in many fields of science. Especially, in the field of biophysics where the biological objects are prone to less thermal damage as the use of LG beams in optical trapping (OT) leads to the region of low intensity at the center of trapping beam. The high efficiency of the optical vortex (OV) trap over conventional Gaussian beam formed the basis of many theoretical and experimental studies. Recently, the OT of neutral atoms in a strong focused Gaussian beam have been observed by Eichmann and his team [10] where they identified the ponderomotive force on electrons leading to the ultra strong acceleration of neutral atoms. Our present work on OT, guiding and acceleration of neutral atoms is also motivated by this work using the LG beam.

1.1 Road map to this thesis

The primary aim of this Ph.D dissertation is to investigate nonlinear optical phenomena associated with the beams carrying OAM which are most realizable in the form of Laguerre-Gaussian (LG) modes popularly known as **twisted light (TL)**. The concept concerning light's OAM came into limelight over the last two decades and from then intensely explored in many classical and quantum applications. We have studied the propagation properties of the beams with helically phased wavefronts in nonlinear media (Chapter 3 and 4) and particle dynamics in twisted light (Chapter 5).

The thesis is organized as follows. Chapter 2 briefly introduces the concept of angular momentum of light which is then followed by a discussion on the important characteristics of the beams carrying OAM i.e. LG beams in Section 2.2 which are the root key of their popularity. Some major classical and quantum applications of TL have been discussed in Section 2.3. Then the novel techniques to generate OAM of a light beam such as spiral phase plate, diffractive optical elements, and cylindrical lens mode convertors are explained under section 2.4.

Chapter 3 presents the results on self-focusing and de-focusing of TL in nonlinear media by deriving the differential equation for the beam width parameter (f) as a function of the propagation distance (ξ), angular frequency (ω), beam waist (ω_0) and intensity of the beam (I). The chapter starts with a brief introduction to the concept of self-focusing in Section 3.1. Further, it is followed by a mathematical background related to the self-focusing in dielectric media which includes, in particular, the propagation of electromagnetic waves (EM) in a linear isotropic medium and in an inhomogeneous medium in Section 3.2. Then in the last Section 3.3, the results on the self-focusing of twisted light in a dielectric media are presented, while formulating the theoretical background on the analytical calculations followed by a discussion and conclusions.

Phase conjugation is a nonlinear optical process which is also known as wavefront reversal, time reversal reflection or retro-reflection. The study on calculating the reflection and transmission coefficients of twisted light at phase conjugating interfaces with a comparison with previous experiments is presented in Chapter 4. Followed by the properties of optical phase conjugate materials i.e. photo-refractive materials like lithium niobate ($LiNbO_3$), lithium tantalate ($LiTaO_3$), barium titanate ($BaTiO_3$) etc. in Section 4.2. Then, the methods to produce phase conjugated waves (PCW) like four wave mixing, stimulated scattering and stimulated emission processes have been reported in Section 4.3 and after that the theoretical formulation which leads to the results concerning reflection and transmission of TL at phase conjugating interfaces are addressed in Section 4.4.

Chapter 5 presents the results on the particles dynamics in TL. In Section 5.1, the calculations on the classical trajectory of a charged particle in TL and the generation of magnetic field with TL are shown. Immediately, after that the study on the optical trapping, guiding and acceleration of neutral atoms on the basis of recent experiment by Eichmann et al. [10] has been shown. The various multi-photon effects like multi-photon ionization (MPI), above threshold ionization (ATI) and high harmonic gener-

ation (HHG) are discussed in section 5.2. Then in Section 5.3, firstly, the concept of OT and its underlying principle of exerting a small force of the order of pico-Newton on the microscopic objects within the range of nm to μm and secondly, the role of TL over Gaussian beams in optical trapping or optical tweezers (OT) are explained. In the last section 5.4, the results on the optical manipulation of neutral atoms in twisted light have been presented in details. Finally, the last chapter 6 concludes the thesis.

Chapter 2

Introduction to Laguerre-Gaussian (LG) beams

2.1 History of angular momentum of light

In 19th century, a Scottish scientist named Sir James Clerk Maxwell smartly collected and corrected the four important laws of the electromagnetic theory which later became popularly known as Maxwell's equations (Eq. 2.1 in Gaussian units) [11]. He especially corrected the Ampere's law by adding an additional term i.e. drift current (**D**) to the free current source.

$$\nabla \cdot \mathbf{D} = 4\pi\rho \qquad \text{Coulomb law,} \qquad (2.1a)$$

$$\nabla \cdot \mathbf{B} = 0 \qquad \text{Gauss law,} \qquad (2.1b)$$

$$\nabla \times \mathbf{E} = -\frac{1}{c}\frac{\partial \mathbf{B}}{\partial t} \qquad \text{Faraday law,} \qquad (2.1c)$$

$$\nabla \times \mathbf{H} = \frac{4\pi}{c}\mathbf{J} + \frac{1}{c}\frac{\partial \mathbf{D}}{\partial t} \qquad \text{Ampere law,} \qquad (2.1d)$$

where ρ is the free charge density, **J** is the free current density, **E** is the electric field intensity, **D** is the electric displacement, **B** is the magnetic flux density or the magnetic induction, **H** is the magnetic field intensity and c is the speed of light in free space. It is a well known fact that the electromagnetic waves possess three important quantities i.e. linear momentum ($p = \hbar k$ per photon), energy ($E = \hbar\omega$ per photon) and angular momentum which can be further divided into two parts: Spin angular momentum (SAM) and orbital angular momentum (OAM). It was Poynting in 1909 who firstly realized that the spin angular momentum is related to light's polarization. According to him, each photon can possess $\sigma\hbar$ of angular momentum where σ can have two discrete states either $+1$ or -1 where the sign is given by the chirality and its experimental proof was given by Beth [5] by using birefringent wave plates. The SAM is inherent in light beams with circular or elliptical polarization and depends on the vectorial properties of the electric field (Fig. 2.1). It has been detected by Friese et al. [12] that the transfer of SAM to objects sets the objects in rotation about their own axis. On the contrary,

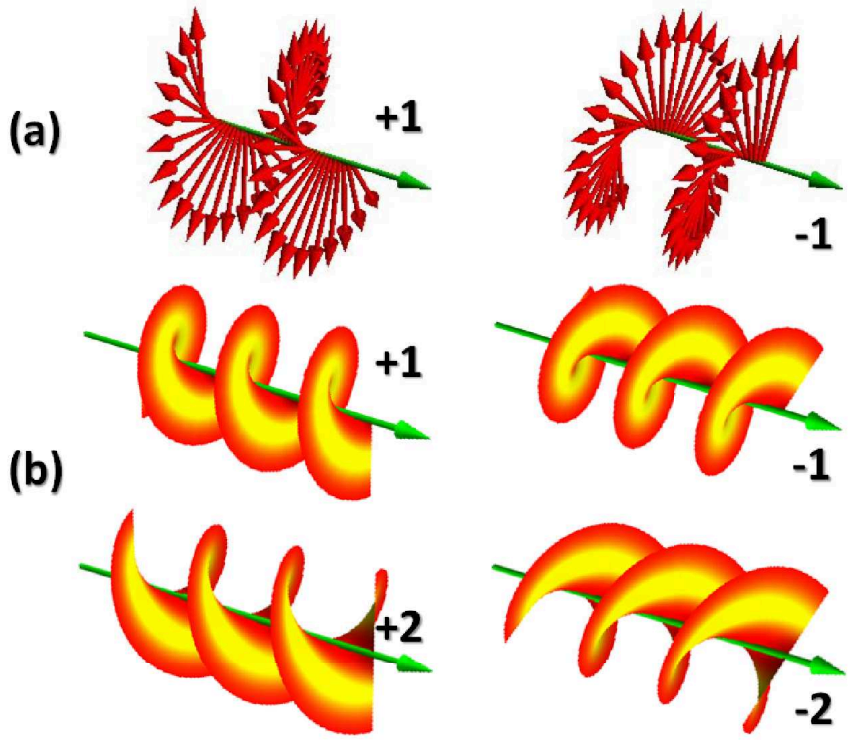

Figure 2.1: (a) The optical field structure of Left and Right circularly polarized beam, respectively. (b) The helical phase front of beams carrying different values of OAM (Here, propagation direction is indicated by a green arrow and regions of low and high intensity are denoted by red and yellow color respectively) [13].

OAM is independent of the polarization state and associated with the spatial structure of the optical field. Thus, the beam with a helical phase-front has a definite value of OAM in the propagation direction and given by the relation $\ell\hbar$ per photon (Fig. 2.1). Both SAM and OAM can be treated classically as well as quantum mechanically [2].

The most common form of a helically phased beam is the Laguerre-Gaussian (LG) mode, the details of which can be seen in Section 2.2. The Poynting vector **S** for any beam (which represents energy flux) is always perpendicular to the phase front but for the beam with a spiral phase front (i.e. LG beam), it rotates at an inclined angle with respect to the propagation direction and hence leads to 'twist of light'. The relation between the angular momentum density (**L**), momentum density (**P**) and Poynting vector (**S**) can be written as [14, 15]

$$\mathbf{L} = \mathbf{r} \times \mathbf{P}, \tag{2.2}$$

where

$$\mathbf{P} = \frac{1}{c^2}\mathbf{S}^2. \tag{2.3}$$

Therefore,

$$\mathbf{L} = \mathbf{r} \times \frac{1}{c^2 \mu_0} (\mathbf{E} \times \mathbf{B}). \tag{2.4}$$

Thus, the total angular momentum of the field ($\mathbf{L}_t$) is

$$\mathbf{L}_t = \int \mathbf{r} \times \mathbf{S} d\mathbf{r}, \tag{2.5}$$

where $\mathbf{r}$ is the radius vector of the field and ε_0 is the vacuum permittivity of free space. The total angular momentum of the field is equal to the sum of the orbital (ℓ) and spin angular momentum (σ). In case of linearly polarized light, $\sigma = 0$ and hence, the contribution to the total angular momentum ($\mathbf{L}_t$) can be given in the form of orbital angular momentum only and is denoted as $\mathbf{L}$. For the beam with helical phase-fronts, the Poynting vector ($\mathbf{S}$) has an azimuthal component given by $\exp(-i\ell\phi)$ where ϕ denotes the azimuthal co-ordinate in the beam's cross-section and ℓ is the topological charge or winding number. The transfer of OAM can be seen by focusing the LG beam into the samples of micro-spheres in the process of optical trapping, as explained in the chapter 5.

2.2 Laguerre-Gaussian (LG) beams

A realizable example of the beam carrying OAM is the Laguerre-Gaussian (LG) beam which came into existence after the introduction of the concept of OAM by Allen et al. [16, 17]. The LG beam is not the only example of the beam carrying helical phase-fronts, there are several other families of beams too which carry OAM such as Mathieu beams [18], Bessel beams [19, 20], Ince-Gaussian beams [21] and Hypergeometric beams [22] etc. However, this thesis aimed to address the issues concerning the LG beams only. The LG beam, (or phase singularity or optical vortex) has, in general, an annular transverse intensity profile and its polynomial i.e. $L_p^{|\ell|}$ is specified by the mode indices ℓ, related to the angular degree of freedom around the propagation direction, and p describes the number of radial nodes of the beam's radial profile. It has a spiral phase front with a $2\pi\ell$ phase shift around the circumference of the beam, where ℓ is an integer which can either be positive or negative. The phase at the center of the beam is undefined and hence, carries no energy or momentum and results in a dark central core or singularity. Thus, the transverse intensity profile of an optical vortex is just a ring of light. A vortex with a negative value of ℓ has a spiral phase front with the opposite helicity to that of a vortex with ℓ value of the same magnitude but positive polarity.

Just like Gaussian beam, the optical vortex is also able to trap objects with a higher refractive index than their surroundings into the most intense region of light. Objects that are small compared to the size of the beam become trapped off-axis in the bright ring of the beam whereas objects with larger size as compared to the beam are trapped on-axis. Below, the transverse intensity profiles and azimuthal phases of the LG beams (or optical vortex) with the changing values of ℓ are shown in Fig. 2.2. The amplitude distribution of the LG beam which is a solution to the paraxial wave equation can be

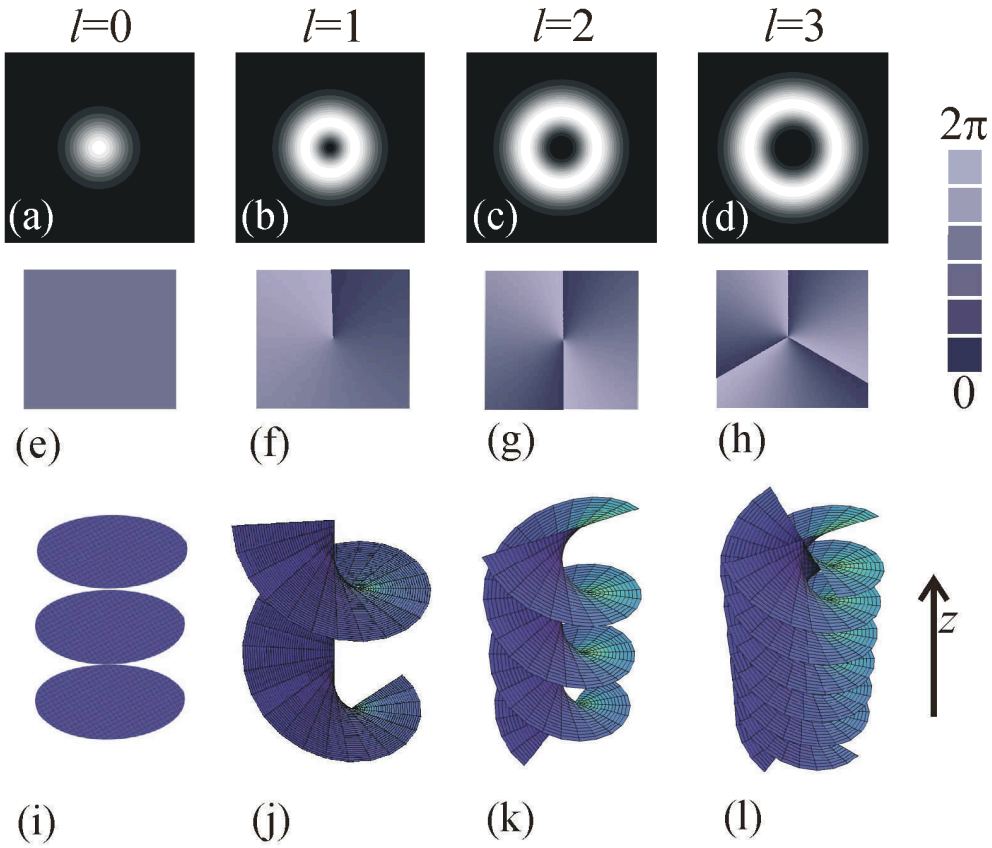

Figure 2.2: Intensity profiles of Laguerre-Gaussian beams with $p = 0$ and (a) $\ell = 0$, (b) $\ell = 1$, (c) $\ell = 2$, (d) $\ell = 3$. The corresponding azimuthal phase is shown below the intensity profiles in (e), (f), (g) and (h), where the color chart shows the corresponding phase. Three dimensional representations of the phase fronts are shown in (i), (j), (k) and (l) with vertical propagation axis z [23].

given as [24]

$$u_{\ell p}^{LG}(r,\phi,z) = \frac{C_p^{|\ell|}}{w(z)}\left(\frac{\sqrt{2}r}{w(z)}\right)^{|\ell|}\exp\left(\frac{-r^2}{w^2(z)}\right)L_p^{|\ell|}\left(\frac{2r^2}{w^2(z)}\right) \times \exp\left(-i\frac{kr^2z}{2(z^2+z_R^2)} - i\ell\phi + i(2p+\ell+1)\arctan\left(\frac{z}{z_R}\right)\right), \quad (2.6)$$

where r, ϕ and z are cylindrical coordinates, ℓ is the azimuthal index, p is the radial mode index, $z_R = \pi w_0^2/\lambda$ is the Rayleigh range, $w(z) = w_0\sqrt{1+(z^2)/(z_R^2)}$ is the radius of the beam at z, where w_0 is the beam waist at $z = 0$. $L_p^{|\ell|}(x)$ is the associated Laguerre polynomial, $C_p^{|\ell|}$ is the normalization constant, and $(2p+\ell+1)\arctan\left(\frac{z}{z_R}\right)$ is the Guoy phase. The radius of curvature of the wavefront, $R(z)$ is

$$R(z) = z\left(1+\left(\frac{z_R}{z}\right)^2\right). \quad (2.7)$$

At the beam waist, $z = 0$, the amplitude of the Laguerre- Gaussian beam simplifies to

$$u_{\ell p}^{LG}(r,\phi,z=0) = C_p^{|\ell|}\left(\frac{\sqrt{2}r}{w_0}\right)^{|\ell|}\exp\left(\frac{-r^2}{w_0^2}\right)L_p^{|\ell|}\left(\frac{2r^2}{w_0^2}\right)\exp(-i\ell\phi). \quad (2.8)$$

and the transverse intensity profile for the LG beam can be given by

$$I(r,z) = \frac{2p!}{\pi(p+|l|)!}\frac{P_0}{w^2(z)}\exp\left(\frac{-2r^2}{w^2(z)}\right)\left(\frac{-2r^2}{w^2(z)}\right)^{|\ell|}\left(L_p^{|\ell|}\left(\frac{2r^2}{w^2(z)}\right)\right)^2, \quad (2.9)$$

where P_0 is the power of the laser beam. The radius corresponding to the maximum intensity is [14]

$$r(z)_{max.\ int.} = \frac{\sqrt{w(z)\ell}}{2}. \quad (2.10)$$

2.3 Applications of Laguerre-Gaussian (LG) beams

There are wealth of applications which can be afforded by the beams carrying orbital angular momentum. For instance, in the field of optical manipulation, the orbital angular momentum can be transferred to trapped microscopic objects causing them to rotate, or to driven micro-machines, or in astrophysics and to encode quantum information due to its infinite dimensionality etc. Below, we have addressed an important classical (Section 2.3.1) and quantum application (Section 2.3.2) of twisted light.

2.3.1 Optical manipulation

The main idea behind implementing the optical vortices i.e. LG beams in the area of optical manipulation is that both angular as well as linear momentum can be transferred

to trapped objects. The azimuthal phase term i.e. exp($i\ell\phi$) associated with LG beams give rise to helical wavefronts and hence this azimuthal component of the Poynting vector leads to the origin of OAM [3, 25]. It has been observed that the OAM exerts torque on particles which can be increased by simply increasing the azimuthal index whereas the optical torque due to SAM is limited to $\hbar$ per photon and varies with optical power [26]. He and his colleagues [4] were the first one who conducted the first rotation experiments by the use of LG modes generated by holographic techniques on absorptive copper oxide particles in two dimensions. In a related work, Simpson and coworkers [27] used the cylindrical lens mode convertor to generate a trapping beam of the LG mode of single order to set the absorptive objects into rotation in three dimensions. Then in 1990's, Friese et al. [26] ensured the results on the optically absorptive particles using holographically generated LG modes with azimuthal index $\ell = 3$ and clearly showed the physical properties of the circularly polarized LG beams. The nature of the angular momentum of light can be understood by examining the motion of particles trapped off-axis in optical tweezers created with the vortex light field. The intrinsic and the extrinsic nature of light's angular momentum simultaneously on a single particle was achieved in 2003 [18]. The particles were placed off-axis within the circumference of the LG beams and showed that the different forms of motion are related to SAM (spinning of particle about its own axis) or OAM (rotation around the beam axis) [18]. Whereas Curtis and Grier [28] explored the dependence of rotations on the azimuthal index of the LG beam. They found that the annular radius of the beam scaled linearly with the winding number ℓ. Later on, Jesacher and colleagues [29] revealed the trapping of particles held at air-water surface with the LG modes. This study discussed the effect of the particle's shape on the momentum transfer in the LG beams, which was not considered in the previous studies. The two responsible factors: (i) asymmetric particle shape, (ii) confinement of the particle at the two dimensional air-water interface laid the foundation of this observation. On the other hand, Tao and colleagues [30] used the fractional optical vortex beams to rotate trapped particles. However, the fractional optical vortex beam significantly hinder the smooth orbital rotation of the particle as it shows the intensity discontinuity (low intensity gap) around the beam circumference. This fractional vortex was exploited in the guiding and transport of microscopic particles.

Later, in 2008, Dienerowitz et al. [31] for the first time showed the transfer and confinement of OAM from the LG beam to 100 nm gold particles at 514 nm, considered to be the smallest particles to set into rotation by the transfer of the OAM. They found the linear increase in rotation rate with respect to laser power, with a maximum rate of 3.6 Hz at 110 mW. In optical manipulation, it is not solely the phase structure of the LG beams but their annular intensity profile is also of interest in the optical trapping of particles with a higher refractive index than its surroundings. The LG beams also proved worth to trap low index particles which found applications in numerous chemical and biological processes where the target samples get repelled from the region of high light intensity. The trapping of low index particles was firstly observed by Arthur Ashkin [32]. He observed that the low index particles get repelled from the high intensity region of light while the high index particles get trap easily onto the region of high

intensity. Then, on the basis of this observation, he demonstrated the trapping of low index glass spheres against gravity while using the LG modes. Gahagan and Swatzlander [33] also confirmed the trapping of low index particles, in their studies they confined the 20 μm size hollow spheres. Immediately, after that other studies have also been conducted to show the trapping of both high and low index particles by the LG modes simultaneously [34]. The another important use of the LG beams can also be seen in the improvement of the axial confinement [35] where the LG modes exert less on-axis scattered force along the axial direction as compare to Gaussian beams where light leads to axial scattering forces that act against gradient forces to destabilize the trap. The light fields possessing optical vortices also allow the manipulation of droplets where the refractive indices of most liquids are smaller than their surrounding medium. Lee et al. [36] used this property of the beams with optical vortices in their study by misalignment of the spiral plate in a direction orthogonal to the beam propagation direction. This allowed the formation of an efficient stable asymmetrical optical light pattern which can be considered as an off-axis vortex beams. It is also observed that one can rotate a three dimensional cubic structure by interfering two LG beams of equal but opposite sign azimuthal index which generates an annular ray of spots that can be rotated with careful adjustment of relative path length between the two arms of interferometer [37]. Moreover, the trapped particle can also be spun with high frequency by applying the angular Doppler technique to create a frequency shift between the interfering LG beams [38]. Thus, indeed the optical manipulation with embedded optical vortex i.e. LG beams has its own importance which shed light on various applications in different fields of science. The chapter 5 of the thesis will address the same application of twisted light in more details while concluding the interesting results on it.

2.3.2 Quantum optics and quantum communication

The use of the OAM of light is not only limited to classical applications rather it has become the mode of important applications at quantum level as well, in particular, in the field of quantum information. From the point of view of quantum optics, the quantum excitations of electromagnetic waves can be described in terms of physical quantities like energy, momentum and angular momentum [39]. This set of quantities then gives rise to a family of modes of an electromagnetic field. The very first family mode are well known “plane waves” which consists of parameters like energy, linear momentum and transversal polarization. The second set of family mode are “electromagnetic multipolar mode or spherically symmetric electromagnetic modes” which are parameterized by energy, total angular momentum of the field, the z component of the angular momentum and the parity of the field. These modes are important in the processes like light-matter interactions but difficult to generate, control and measure which make them less used in the field of quantum information. The third family of modes belongs to “cylindrically symmetric paraxial modes” which can be defined in terms of the energy, the z component of the linear momentum, the z component of the OAM and the z component of the SAM. The important property of these modes

is that both the SAM and the OAM can be determined independently by controlling the spatial properties and the polarization of the field. The main obstacle in dealing with the SAM is its inherent binary dimensionality, therefore only a bit of information can be encoded, whereas the OAM dimensionality is infinite which results in the more alphabets in the OAM space which can be used in the field of space telecommunication more efficiently [40].

Aspect and his coworkers [41] showed that the angular momentum (AM) of two photons can be entangled in such a way that a measurement on the polarization of one of the photons appears to modify instantaneously the polarization state of the other photon irrespective of the distance between the particles. Thus, the polarization of the entangled photon pair can be written as

$$|\psi\rangle = \frac{1}{\sqrt{2}}(|\circlearrowleft\rangle_i|\circlearrowright\rangle_s + |\circlearrowright\rangle_i|\circlearrowleft\rangle_s), \tag{2.11}$$

where $|\circlearrowleft\rangle$, $|\circlearrowright\rangle$ denotes the left and right polarization states, and i, s are the idler and signal photons. The evidence of these experiments strongly supports the quantum mechanics and provides convincing existence of entangled states. The SAM entangled states are the basis of many impressive quantum information schemes such as; quantum cloning, quantum communication, quantum cryptography and many more.

However, the breakthrough in the OAM entanglement in photon pair was seen in 2001 by Zeilinger and coworkers [42]. They measured the OAM correlations between two photons with the help of a spontaneous parametric down-conversion source (SPDC) and showed that the photons could be entangled in their OAM degree of freedom.

The SPDC can generate an entangled state over the whole OAM states as,

$$|\psi\rangle = \frac{1}{\sqrt{2}}\sum_{\ell=-\infty}^{+\infty}(|-\ell\rangle_i|\ell\rangle_s + |\ell\rangle_i|-\ell\rangle_s), \tag{2.12}$$

where $|\ell\rangle$ denotes the OAM state. In this experiment, it has been confirmed that light's OAM is a quantum variable associated with a single photon. The major drawback in encoding OAM information in photons in communication is its non-reliability to transmit information over the large distances but besides that it is still quite useful in testing the properties of high dimensional spaces.

2.4 Methods to generate twisted light

In practice, there are many ways to generate the helically phased wavefronts. Out of them, few powerful ones have been described below in details.

2.4.1 Spiral phase plate (SPP)

SPP is a type of beam mode convertor. It has a thickness which varies with circumference around the plate but is uniform radially. The plate is made of a dielectric material

which is transparent in nature with one plane and one spiral surface. Such a thin transparent plate typically has strips or radial sectors that can be obtained by coating or etching a substrate [3]. The thickness of the spiral phase plate (SPP) increases proportional to the azimuthal angle, ϕ, around a point at the center of plate. Thus, the spiral surface forms a period of helix. Hence, when a fundamental mode i.e. Gaussian beam mode (TEM_{00}) of wavelength λ passes through the SPP, it undergoes a phase change which introduces a spiral element into its wavefront resulting into a generation of helical wavefront with OAM equal to $\hbar$ per photon (Fig. 2.3). The SPP introduces a phase shift in the output beam, δ, which depends on the azimuthal angle ϕ by a relation

$$\delta = \frac{(n_1 - n_2)d}{\lambda}\phi, \tag{2.13}$$

where n_1, n_2 are the refractive indices of the SPP and surrounding medium, respectively, and d is the physical step height at $\phi = 0$. In order to generate a beam with a well-defined value of OAM, e.g. $\ell\hbar$, the total phase delay around the SPP must be an integer multiple of 2π, i.e. $2\pi\ell$. Thus, to produce this beam, the thickness of the SPP is given as

$$d = \frac{\ell\lambda}{(n_1 - n_2)}. \tag{2.14}$$

It is important to have the step height 'd' of the SPP to be an integer number of wavelength otherwise the phase of beam gets discontinuous at 'd' and this discontinuity breaks the ring intensity pattern. Later, Beijersbergen et al. [43] shown that the convertor only changes the phase pattern of beam and it does not change the beam's intensity by taking small angle approximation into account. Thus, the beam produced is not a pure LG mode, but is an infinite superposition of the LG modes [44] which leads to the observation that a rigorous calculation of the SPP operation would require vector-diffraction theory. Thus, for a beam with a small divergence and with a sufficiently small step height, we remain in the paraxial regime. So, the effect of the SPP is considered to be an operation acting on the field phase only. Although the OAM is a property of the beam as a whole, it is useful to consider this in terms of two equivalent angular momentum per photon. Let us, consider a ring of radius r is projected on the spiral surface. Then, the angle, θ, of the local azimuthal slope of the spiral surface is given as [13]

$$\tan\theta = \frac{d}{2\pi r}. \tag{2.15}$$

A ray parallel to, but at a distance $\mathbf{r}$ from, the optical axes will be refracted as it emerges from the spiral surface. By using Snell's law, one can give the deflection angle, α, as

$$n_2 \sin(\alpha + \theta) = n_1 \sin\theta. \tag{2.16}$$

It has been seen that before refraction, the beam has a linear momentum of $n_2\hbar/2\pi\lambda$ per photon and after refraction, there is a component of linear momentum in the azimuthal direction

$$P_\phi = \frac{n_2\hbar}{2\pi\lambda}\sin\alpha. \tag{2.17}$$

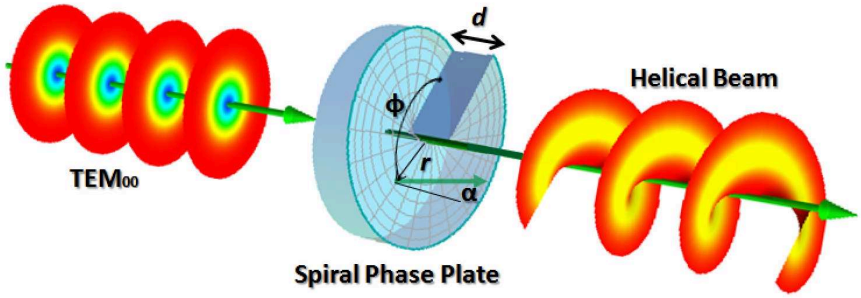

Figure 2.3: Schematic of a spiral phase plate (SPP) illuminated by a TEM_{00} beam and its outgoing wave i.e. Helical beam [13].

Thus, there is a transfer of angular momentum, L, between the SPP and the beam of light of

$$L_z = \frac{n_2 \hbar r}{2\pi\lambda} \sin\alpha. \tag{2.18}$$

per photon in the beam. For a small angle, it can be shown that the OAM transfer from the plate to the light is equal to

$$L_z = \ell\hbar \tag{2.19}$$

per photon in the direction of the beam which will result into two important effects. First, the beam now has a non-zero angular momentum. Second, the beam must has a null field amplitude on its axis. This non-zero angular momentum has some interesting consequences such as the ability for trapping and rotating of particles, as mentioned in the Section (2.3.1).

2.4.2 Diffractive optical elements (DOE)

The LG beams can also be generated by using diffractive optical elements i.e. numerically computed holograms. Such holograms can generate beams with any desired values of OAM which cannot be achieved by using the spiral phase plates (Fig. 2.4). These holograms can be formed by recording onto a photographic film, the interference pattern between a plane wave and the beam one seeks to produce with the same uniform and equal intensities.

Consider a plane reference wave in the $x-y$ plane, $E_r = E_0 e^{i(k_x x + k_z z)}$ with an incident angle $\alpha = \arcsin\left(\frac{k_x}{k}\right)$ and intensity $|E_0|^2$. At the $z=0$ plane, the interference pattern with a helical beam, $E_\ell = E_0 e^{i\ell\phi}$ is given by

$$I = 2|E_0|^2(1 + \cos(k_x x - \ell\phi)). \tag{2.20}$$

At the exit of the hologram, the optical field is given as:

$$E_t = \frac{A_0}{2}(1 + \cos(k_x x - \ell\phi)). \tag{2.21}$$

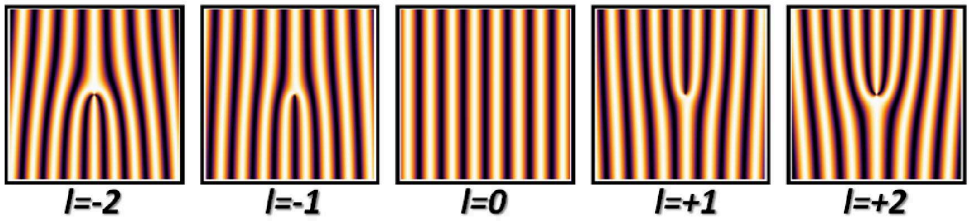

Figure 2.4: The intensity density pattern of interference between two helical and a planar beam for several different values of the charge singularities [13].

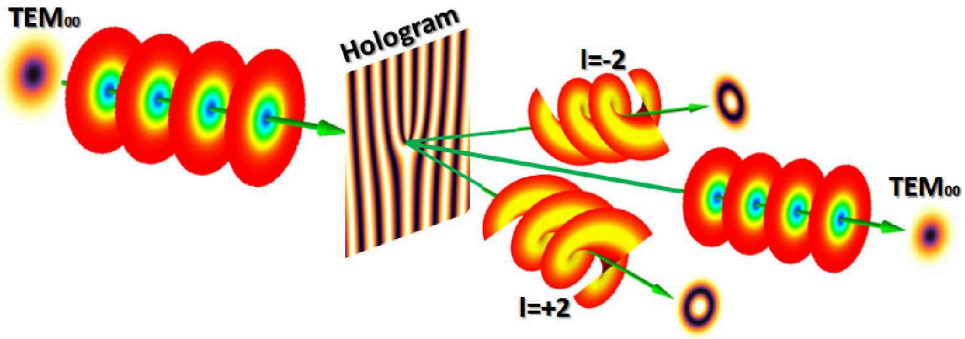

Figure 2.5: Beams generated by a sinusoidal pitch-fork hologram. A fraction of the power is diffracted on the first order and other part remains on the zeroth order. The topology of the hologram is objected to generate beams with $|\ell|=2$ [13].

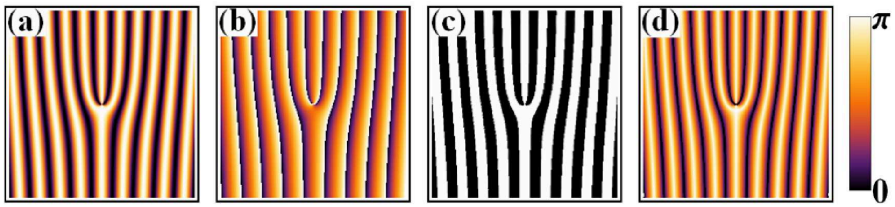

Figure 2.6: Different holograms pattern for the generation of a helical beam with ℓ=2. (a) Sinusoidal, (b) Blazed, (c) Binary, and (d) Triangle holograms [13].

Type of grating	Amplitude Hologram		Phase Hologram	
	Generated order	Efficiency	Generated order	Efficiency
sinusoidal	zero + first orders	6.25%	all	33.85%
blazed	all	2.53%	Just first order	100%
squared	odd	10.13%	odd	40.52%
triangle	odd	4.10%	all	29.81%

Table 2.1: Ideal efficiency of different types of grating and different kind of holograms [13].

This optical field can be recognized as consisting of a zero-order beam propagating along the axes and two (conjugate) first-order diffracted beams each of them containing a singularity of opposite charge ($+\ell$) and ($-\ell$) (Fig. 2.5). The grating's shape (Fig. 2.6), that is fringe's shape patterns of a hologram also plays an important role in determining the efficiency of a given hologram, in addition to the way of encoding either in amplitude or phase. There are mainly four types of gratings which are summarized in the table (Table. 2.1) along with their efficiencies which leads to the LG beams generation. The diffractive optical elements can also be found in the form of spatial light modulator commercially [45]. These are pixellated liquid crystal devices that can be programmed through the video interface of a computer to act as holograms. Changing their design is very simple as by just changing the image displayed by the computer interfacing the device. Usually, a spatial light modulator (SLM) modulates the intensity of the light beam. However, it is also possible to produce devices that modulate the phase of the beam or both the intensity and the phase simultaneously.

2.4.3 Cylindrical lens mode convertors

The other powerful method of generating the LG beams is the use of cylindrical lens mode convertor. It is an optical device which alters the polarization state of a light wave traveling through it. Its work is to shift the phase between perpendicular polarization components of the light wave. The Woerdman's group [46] was the first one who demonstrated how the LG modes can be generated with the help of cylindrical lens mode convertor while using the Hermite-Gaussian (HG) modes as the primary source.

The mechanism of the cylindrical lens mode converter can be understood on the

basis of LG and HG mode relations. The HG mode is given as:

$$|HG\rangle_{m,n} = \sqrt{\frac{2}{2^{(m+n)}\pi m!n!}}\frac{1}{\sqrt{1+\zeta^2}}e^{-i(m+n+1)\arctan\zeta} \times e^{-\left(\frac{1+i\zeta}{1+\zeta^2}\right)(\eta^2+\xi^2)}H_m\left(\sqrt{\frac{2}{1+\zeta^2}}\eta\right)H_n\left(\sqrt{\frac{2}{1+\zeta^2}}\xi\right) \quad (2.22)$$

where $H_n(x)$ is the Hermite polynomials of the order n, ($\xi = \frac{x}{w_0}, \eta = \frac{y}{w_0}, \zeta = \frac{z}{z_R}$) are the dimensionless coordinates in the paraxial waves where, w_0 is the beam waist and z_R is the Rayleigh parameter. The HG modes are an orthogonal set of modes

$$_{m',n'}\langle HG|HG\rangle_{m,n} = \delta_{m,m'}\delta_{n,n'}. \quad (2.23)$$

and can carry finite power. According to the mode order $N = m + n$, the LG mode is written as

$$|LG\rangle_{m,n} = (-1)^{min(m,n)}\sqrt{\frac{2}{\pi m!n!}}\frac{1}{\sqrt{1+\zeta^2}}e^{-i(m+n+1)\arctan\zeta} \times e^{-\left(\frac{1+i\zeta}{1+\zeta^2}\right)\rho^2}e^{i(m-n)\phi}\left(\sqrt{\frac{2}{1+\zeta^2}}\right)^{|m-n|}L^{|m-n|}_{min(m,n)}\left(\frac{2\rho^2}{1+\zeta^2}\right) \quad (2.24)$$

where $\zeta = (\eta + \xi)$ and $min(m, n)$ denotes the minimum between m and n. The radial index p of the LG beam normally used is $min(m, n)$ and the azimuthal index m is $m-n$. The generation of the LG modes using mode convertors is based on the fact that a $HG_{m,n}$ mode at an angle of 45° is decomposed onto a set of HG modes and then this set of HG modes when re-phased can combine to form a particular LG mode. The re-phasing occurs because as each HG mode is focused by the lenses it undergoes a different Gouy phase shift (ζ) depending on its modes indices and orientation with respect to the cylindrical lenses [46, 47]. As, both HG and LG modes carry finite power, they form an orthogonal and complete set of modes. So, it is possible to expand the LG beam into a set of HG modes of the same order with the help of the following relation:

$$|LG\rangle_{m,n} = \sum_{k=0}^{N} i^k b(m,n;k)|HG\rangle_{N-k,k} \quad (2.25)$$

and similarly HG mode is expanded in the HG basis by rotating its principal axis about 45° around the propagation axis i.e. ζ by using the following relation:

$$|HG\rangle_{m,n}|_{@45^\circ} = \sum_{k=0}^{N} i^k b(m,n;k)|HG\rangle_{N-k,k}, \quad (2.26)$$

where $b(m, n; k)$ is the real expansion coefficient and is given as

$$b(m,n;k) = \sqrt{\frac{(N-k)!k!}{2^{(m+n)}m!n!}}\frac{1}{k}\frac{d^k}{dt^k}[(1-t)^n(1+t^m)]|_{t=0} \quad (2.27)$$

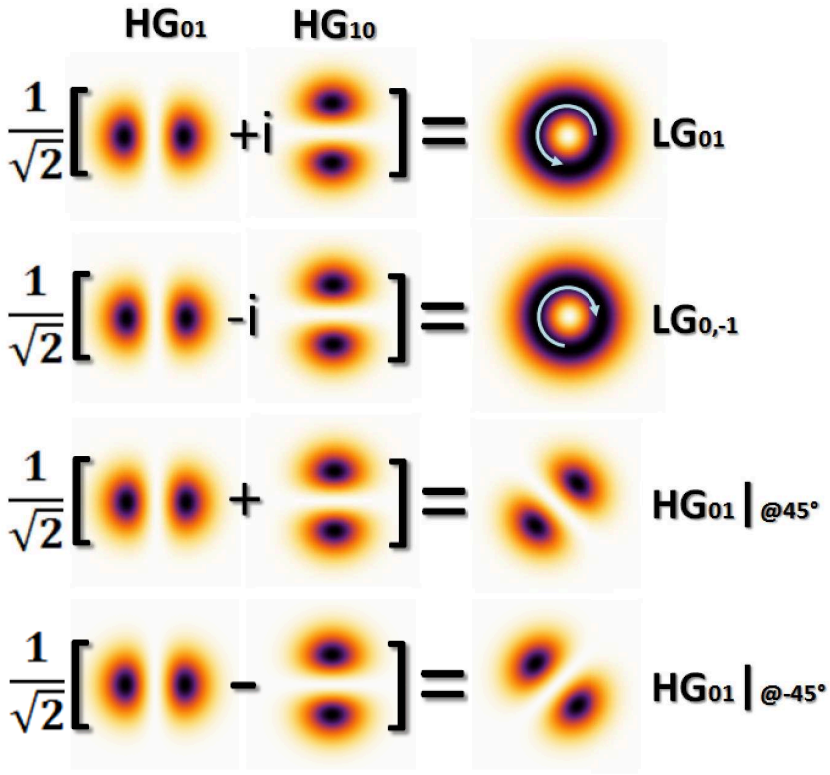

Figure 2.7: Decomposition of the $LG_{0,1}$, $LG_{0,-1}$, $HG_{0,1}|_{@45^\circ}$ and $HG_{0,1}|_{@-45^\circ}$ modes in the HG basis [13].

where N indicates the mode order. The factor i^k corresponds to a $\pi/2$ relative phase difference between the successive components. The only difference between Eq. 2.25 and Eq. 2.26 is the relative phase between successive terms and in the expansion given by Eq. 2.26, all the terms are in phase which can be seen in the last rows of Fig. 2.7

The cylindrical lens mode convertors have two main forms: the $\pi/2$ mode convertor and the π mode convertor. The $\pi/2$ mode convertor transforms any incident HG modes with indices m, n oriented at 45° to the cylindrical axis of the lens, into an LG mode with indices $l = m - n$ and $p = min(m, n)$ (Fig. 2.8). On the other hand, the π mode convertor (Fig. 2.9), transforms any mode into its own mirror image and is optically equivalent to a Dove prism. These cylindrical lens convertors are mathematically analogous to the action on polarization of a birefringent $\lambda/4$ plate and a $\lambda/2$ plate respectively. Their advantage over diffractive optical elements (Section 2.4.3) is that the optical efficiency of the conversion is much higher, limited only by the quality of the anti-reflection coatings of the lenses.

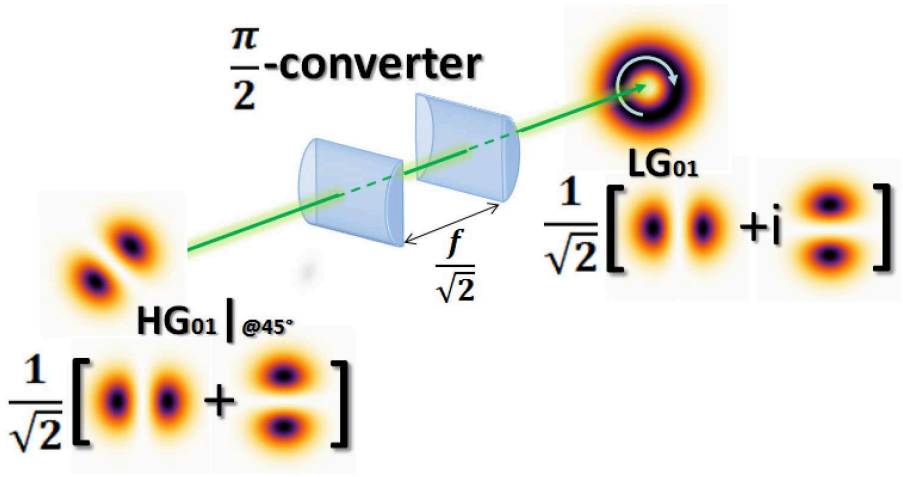

Figure 2.8: Schematic of the $\pi/2$ mode convertor. The distance between two cylindrical lenses is $\frac{f}{\sqrt{2}}$. The $\pi/2$ mode convertor converts diagonal $HG_{0,1}|_{@45^\circ}$ to $LG_{0,1}$, where f is the lens focal length [13].

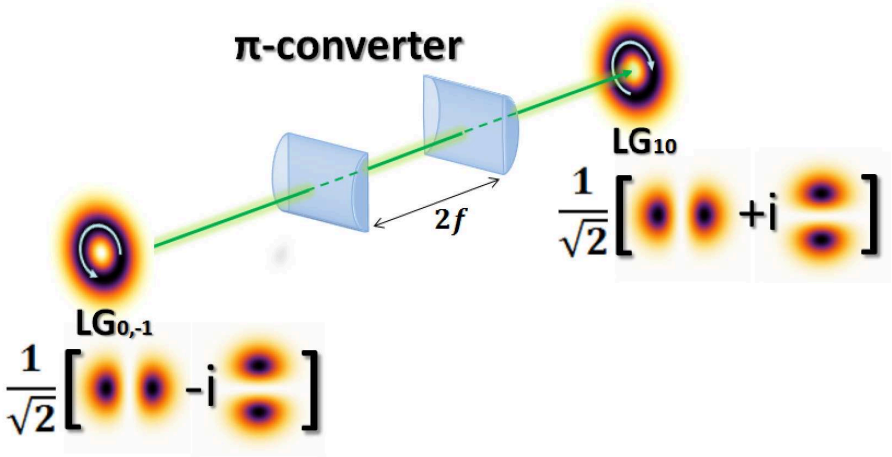

Figure 2.9: Schematic of the π mode convertor. The distance between two cylindrical lenses is $2f$. The π mode convertor converts $LG_{0,\ell}$ to $LG_{0,-\ell}$, where f is the lens focal length [13].

The table (Table. 2.2) compares the three above explained methods of generating LG beams on the ground of their efficiencies [48].

Creation method	ℓ mode	Mode purity $p=0$	Mode purity $p=1$	Conversion efficiency	Extinction ratio
Spiral phase plate	1	78.5% [14]			
	2	50% [14]			
Computer generated	1	93% [17]	80% [16]	40%	
holograms	3	77% [17]			
	6	62.8% [17]			
Diffractive optics	1	92.9%		40%	$(2.5\pm0.8)\times10^{-2}$
(this work)	2		99.3%	60%	$(3.3\pm0.8)\times10^{-2}$

Table 2.2: Comparison of LG_p^ℓ beam characteristics using different generation methods of twisted light [48].

Chapter 3

Self-focusing and de-focusing of twisted light in non-linear media

The self-focusing of electromagnetic waves in nonlinear optical media has been a fascinating topic and inspired many theoretical and experimental studies from the past few decades [6, 49–55]. It is regarded as a basic phenomena in nonlinear optics with a variety of important applications that rely on the manipulation and control of the photon beam. The phenomenon of self-focusing and de-focusing of electromagnetic beams in nonlinear media was reviewed by Akhmanov et al. [54]. The theoretical formulation of self-focusing is well known for many years and is found to be dependent on the propagation characteristics, the properties of the medium and to the pulse width of laser beams. Recently, several investigations were conducted to study the propagation properties of Cosh-Gaussian and Hermite-Gaussian beams in different media [56, 57]. Here, in this chapter, we study the self-focusing and de-focusing of the light beam carrying orbital angular momentum (called twisted light) propagating in a nonlinear medium [58]. We have derived a differential equation for the beam width parameter (f) as a function of the propagation distance (ξ), angular frequency (ω), beam waist (ω_0) and intensity of the beam (I). The method is based on the Wentzel-Kramers-Brillouin (WKB) and the paraxial approximations. Analytical expressions for f are obtained, analyzed and illustrated for the typical experimental situations.

3.1 Basics of self-focusing

The invention of the first laser in 1960$'s$, revolutionized the field of nonlinear optics. In nonlinear effects, the polarization of a material, **P**, is no longer a linear function of the electric field **E** and can be written as a series expansion of the electric field [59]

$$P_i = \chi_{ij}^{(1)} E_j + \chi_{ijk}^{(2)} E_j E_k + \chi_{ijkl}^{(3)} E_j E_k E_l + ..., \tag{3.1}$$

where $\chi_{ij}^{(1)}$ denotes the linear susceptibility tensor, $\chi_{ijk}^{(2)}$ is the second-order susceptibility tensor and $\chi_{ijkl}^{(3)}$ is the third-order susceptibility tensor and so on. The self-focusing

effect, arises from the third order nonlinearity (i.e. $\chi^{(3)}$) and it is known that the susceptibility of the material is related to the refractive index of the material which can be written as

$$n = n_0 + n_2|E|^2 + n_4|E|^4 + ..., \tag{3.2}$$

where n_i are generally complex-valued which implies absorption as well as refraction.

Askar'yan [6] in 1962 was the first one who considered the self-focusing of an electromagnetic beam when he showed that an intense optical beam could induce a difference between the medium, outside the beam and inside the beam which could create conditions which are favorable for the wave-guiding of the beam thus counteracting the beam's natural diffraction. It has been observed that in a nonlinear medium like dielectric, semiconductors and plasmas. If a high power electromagnetic beam increases the electrical susceptibility and thus the refractive index with wave intensity, then in a region where the wave amplitude is amplified, the refractive index gets enhanced. The beam thus creates a refractive index profile across its wavefront corresponding to its own intensity profile and focuses itself. This nonlinear optical self-action effect is called the **self-focusing** [60]. It is an induced lens effect which results from the wavefront distortion imposed on the beam by itself while passing through a nonlinear medium as seen in Fig. 3.1.

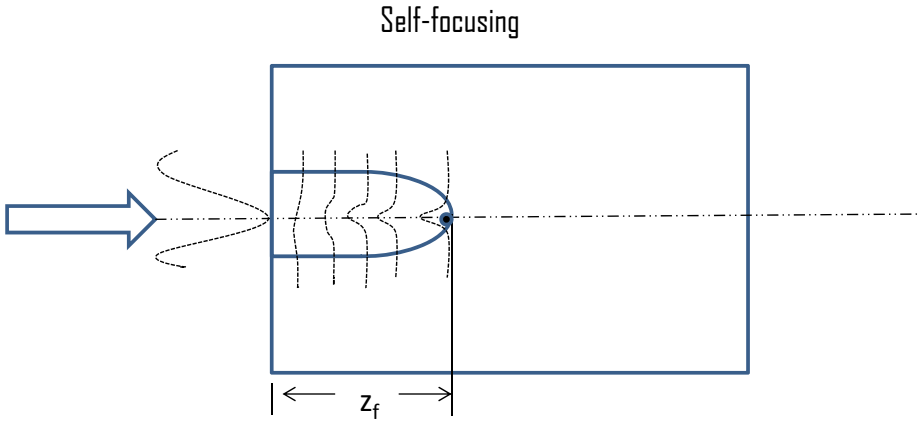

Figure 3.1: Distortion of the wavefront of a laser beam (dashed curve) leading to self-focusing in a nonlinear medium. Here z_f is the self-focusing distance, defined as the distance between the position of self-focused spot (black dot) and the entrance face of the medium.

In order to understand the basic phenomena of self-focusing of an intense electromagnetic beam, consider the propagation of a parallel cylindrical beam of uniform intensity with the circular cross-section of radius 'a' (Fig. 3.2).

The refractive index of the illuminated region is given by

$$n = n_0 + n_2\langle E \cdot E^* \rangle$$

where $\langle\rangle$ denotes the time average and $\langle E^2 \rangle = \frac{1}{2}E_0^2 = \frac{1}{2}(E^*E)$.

If the amplitude of the electric field vector is E_0 and the absorption by the material is negligible, then the refractive index is

$$n = n_0 + \frac{1}{2} n_2 E_0^2.$$

Here n_0 and n_2 are the linear and the non-linear components of the refractive index. Therefore, the waves diverging at an angle θ with the axis will suffer total internal reflection when $\theta < \theta_c$ where θ_c is obtained from

$$\cos\theta_c = \left(\frac{n_0}{n_0 + \frac{1}{2} n_2 E_0^2} \right)$$

or the angle of incidence 'i' is greater than

$$\sin^{-1}\left(\frac{n_0}{n_0 + \frac{1}{2} n_2 E_0^2} \right) = \frac{\pi}{2} - \cos^{-1}\left(\frac{n_0}{n_0 + \frac{1}{2} n_2 E_0^2} \right)$$

We assume that the nonlinearity is weak i.e. $\frac{1}{2} n_2 E_0^2 \ll n_0$, which is indeed true for most systems, consequently θ_c will also be small and we will have

$$1 - \frac{\theta_c^2}{2} \cong 1 - \frac{1}{2} \frac{n_2}{n_0} E_0^2,$$

$$\theta_c \approx \left(\frac{n_2}{n_0} E_0^2 \right)^{1/2}.$$

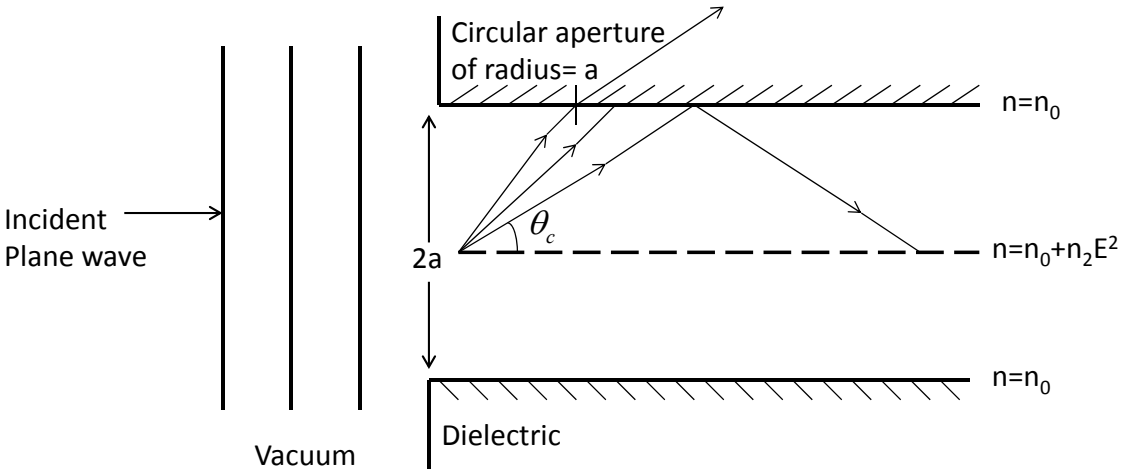

Figure 3.2: Refraction ($\theta > \theta_c$) and total internal reflection ($\theta < \theta_c$) of rays in a nonlinear medium [60].

Now, a beam that is limited by an aperture of radius 'a' will undergo diffraction, we know that the large fraction of the power will be carried by the rays that make an angle less than θ_d with axis, where

$$\theta_d \cong \frac{0.61\lambda}{2a} = \frac{0.61\lambda_0}{2an_0}. \tag{3.3}$$

where $\lambda = \lambda_0/n_0$ represents the wave length in the medium, λ_0 is the wavelength in vacuum and n_0 is the linear component of the refractive index.
If $\theta_d < \theta_c$, then the diffracted rays will make an angle less than θ_c with axis. Hence, the rays will suffer total internal reflection at the boundary and will return to the beam. When $\theta_d > \theta_c$, the beam will spread by diffraction. The critical power of the beam for self-focusing corresponds to $\theta_c = \theta_d$ is given by

$$P_{cr} = \frac{(1.22)^2 \lambda_0^2 c}{128 n_2} \tag{3.4}$$

where P_{cr} is the critical power of the beam.

There are three possibilities:

1. When $P < P_{cr}$ *or* $\theta_d > \theta_c$. In this case, the beam will diverge.
2. When $P = P_{cr}$ *or* $\theta_d = \theta_c$. In this case, the beam propagates without divergence or convergence.
3. When $P > P_{cr}$ *or* $\theta_d < \theta_c$. In this case, the convergence of the beam takes place.

Due to the Kerr effect, an intense laser pulse, while propagating in a nonlinear medium, can experience self-focusing (or de-focusing): depending upon the nonlinear susceptibility (χ) of the medium. In the case of Kerr nonlinearity with positive χ, the higher optical intensities on the beam axis cause an effectively increased refractive index of the beam which results in the focusing effect whereas a negative χ nonlinearity, leads to the self de-focusing effect, where the Kerr lens has a reduced refractive index on the beam axis. In 1964, Chiao and Townes [61] showed that there are two main consequences of the self-focusing as given by Eq. 3.4. They observed that the beam power exactly at the self-focusing limit exhibits self-trapping, where the beam profile stays constant over a longer distance, because divergence gets compensated by the nonlinear focusing effect and for optical powers far above the self-focusing limit, filamentation can occur, where the beam breaks up into several beams with smaller powers.

3.2 Mathematical background of self-focusing in dielectric media

3.2.1 Maxwell's equations

The phenomena in electromagnetism are governed by Maxwell's equations, expressed in the Gaussian system of units followed by most of the scientists engaged in the study of self-focusing of electromagnetic (EM) beams. The Maxwell's equations are

$$\nabla \cdot \mathbf{D} = 4\pi\rho, \tag{3.5}$$
$$\nabla \cdot \mathbf{B} = 0, \tag{3.6}$$
$$\nabla \times \mathbf{E} = -\frac{1}{c}\frac{\partial \mathbf{B}}{\partial t}, \tag{3.7}$$
$$\nabla \times \mathbf{H} = \frac{4\pi}{c}\mathbf{J} + \frac{1}{c}\frac{\partial \mathbf{D}}{\partial t}, \tag{3.8}$$

where ρ is the free charge density, $\mathbf{J}$ is the free current density, $\mathbf{E}$ is the electric field intensity, $\mathbf{D}$ is the electric displacement, $\mathbf{B}$ is the magnetic flux density or the magnetic induction, $\mathbf{H}$ is the magnetic field intensity and c is the speed of light in free space. The fields $\mathbf{E}, \mathbf{D}$ and $\mathbf{B}, \mathbf{H}$ are related through the constitutive relations:

$$\mathbf{D} = \varepsilon\mathbf{E}, \tag{3.9}$$
$$\mathbf{H} = \frac{\mathbf{B}}{\mu}. \tag{3.10}$$

The dielectric function ε and the magnetic permeability μ are properties of the medium in which the fields are measured and are scalars for isotropic media.

For small field intensities, the scalars ε and μ can be considered to be constants and the relations (Eq. 3.9 and Eq. 3.10) are then linear. However, in general, these properties depend on the corresponding fields making the constitutive relations nonlinear. We shall mainly be concerned with non-magnetic materials ($\mu = 1$, $\mathbf{B}$=$\mathbf{H}$), with non-linear dielectric response i.e. $\varepsilon = \varepsilon(\mathbf{E})$. To start with, we shall further assume that the medium does not carry free charges and is non-conducting so that there are no free currents (no dielectric losses). The Maxwell equations therefore, reduce to

$$\nabla \cdot \mathbf{D} = 0 \tag{3.11}$$
$$\nabla \cdot \mathbf{B} = 0 \tag{3.12}$$
$$\nabla \times \mathbf{E} = -\frac{1}{c}\frac{\partial \mathbf{B}}{\partial t} \tag{3.13}$$
$$\nabla \times \mathbf{H} = \frac{1}{c}\frac{\partial \mathbf{D}}{\partial t} \tag{3.14}$$

Substituting $\mathbf{D} = \varepsilon\mathbf{E}$ and $\mathbf{H} = \mathbf{B}$ in Eq. 3.11 and Eq. 3.14 one obtains

$$\nabla \cdot (\varepsilon\mathbf{E}) = \nabla\varepsilon \cdot \mathbf{E} + \varepsilon\nabla \cdot \mathbf{E} = 0, \tag{3.15}$$

and

$$\nabla \times \mathbf{B} = \frac{\varepsilon}{c}\frac{\partial \mathbf{E}}{\partial t}. \tag{3.16}$$

3.2.2 Propagation of EM waves in a linear isotropic medium

Let us first consider the propagation through a linear, uniform, isotropic medium. For such a medium the dielectric function is constant, i.e. $\varepsilon = constant$.
So that Eq. 3.15 gives

$$\nabla \cdot (\varepsilon \mathbf{E}) = \varepsilon \nabla \cdot \mathbf{E} = 0. \tag{3.17}$$

Taking the curl of Eq. 3.13, one obtains

$$\nabla \times (\nabla \times \mathbf{E}) = -\frac{1}{c} \nabla \times \frac{\partial \mathbf{B}}{\partial t} \tag{3.18}$$

The left hand side (L.H.S.) of this equation can be expressed as

$$\nabla \times (\nabla \times \mathbf{E}) = \nabla(\nabla \cdot \mathbf{E}) - \nabla^2 \mathbf{E}$$

On the right hand side (R.H.S.) of Eq. 3.18, the operator ∇ being a space operator, commutes with the time operator $\partial/\partial t$ so that

$$\nabla \times \frac{\partial \mathbf{B}}{\partial t} = \frac{\partial (\nabla \times \mathbf{B})}{\partial t},$$

which, in view of Eq. 3.16 reduces to

$$\nabla \times \frac{\partial \mathbf{B}}{\partial t} = \frac{\varepsilon}{c^2} \frac{\partial^2 \mathbf{E}}{\partial t^2}$$

Substituting these two relations in Eq. 3.18, one obtains

$$\nabla(\nabla \cdot \mathbf{E}) - \nabla^2 \mathbf{E} = -\frac{\varepsilon}{c^2} \frac{\partial^2 \mathbf{E}}{\partial t^2}. \tag{3.19}$$

Eq. 3.17 then reduces the above equation to the wave equation

$$\nabla^2 \mathbf{E} - \frac{\varepsilon}{c^2} \frac{\partial^2 \mathbf{E}}{\partial t^2} = 0. \tag{3.20}$$

A solution of this equation is

$\mathbf{E} = \mathbf{E_0} \exp i(\omega t - \mathbf{k} \cdot \mathbf{r})$ which represents a plane wave propagating in the direction of the wave vector $\mathbf{k}$ with

$$k^2 = \frac{\varepsilon \omega^2}{c^2}, \tag{3.21}$$

ω/k is the phase speed of the wave.

For purely transverse waves, the wave vector $\mathbf{k}$ and the fields $\mathbf{E}$ and $\mathbf{B}$ are mutually perpendicular. Henceforth, we shall assume that the EM wave is purely transverse and propagating in the positive z direction so that it can be represented as

$$\mathbf{E} = \mathbf{E_0} \exp i(\omega t - \mathbf{kz}), \mathbf{k} \cdot \mathbf{E} = 0. \tag{3.22}$$

3.2.3 Propagation of EM waves through an inhomogeneous medium

In an inhomogeneous medium the dielectric function depends on the space coordinates; the inhomogeneity may be partly or wholly on account of the dependence of ε on $\mathbf{E}$ and the non-uniform distribution of $\mathbf{E}$ in space. The space coordinates may be cartesian (x, y, z) or cylindrical polar (r, θ, z). In either case, the z direction is the direction of propagation of the EM wave as stated before.

Let us first consider the propagation of a plane wave of uniform irradiance (intensity) profile through non-absorbing medium for which the dielectric function is given by $\varepsilon = \varepsilon(z)$.
In this case, Eq. 3.15 simplifies to

$$\nabla \cdot (\varepsilon \mathbf{E}) = \frac{\nabla \varepsilon \cdot E}{\varepsilon} = -\frac{1}{\varepsilon}\hat{\mathbf{k}}\frac{\partial \varepsilon}{\partial z} \cdot \mathbf{E}$$

where, $\hat{\mathbf{k}}$ is a unit vector in the z direction. The field $\mathbf{E}$ is perpendicular to the wave vector which is also directed along the z axis therefore, $\hat{\mathbf{k}} \cdot \mathbf{E} = 0$. Hence, the wave equation reduces to the form (Eq. 3.20) with $\varepsilon = \varepsilon(z)$. The Laplacian operator reduces to $\nabla^2 = \partial^2/\partial z^2$, since the field $\mathbf{E}$ is independent of the transverse space coordinates. Therefore, the wave equation Eq. 3.19 takes an one dimensional form

$$\frac{\partial^2 \mathbf{E}}{\partial z^2} - \frac{\varepsilon(z)}{c^2}\frac{\partial^2 \mathbf{E}}{\partial t^2} = 0. \tag{3.23}$$

Putting $\mathbf{E}(z, t) = \mathbf{E_0}(z)\exp(\pm i\omega t)$ in the above equation, where ω is the wave frequency, one obtains

$$\frac{d^2 \mathbf{E_0}(z)}{dz^2} - \frac{\omega^2}{c^2}\varepsilon(z)\mathbf{E_0}(z) = 0. \tag{3.24}$$

Writing

$$\frac{\omega^2}{c^2}\varepsilon(z) = k^2(z), \tag{3.25}$$

Eq. 3.24 can be put in the form

$$\frac{d^2 \mathbf{E_0}(z)}{dz^2} - k^2(z)\mathbf{E_0}(z) = 0 \tag{3.26}$$

or in the scalar form

$$\frac{d^2 \mathbf{E_{0i}}(z)}{dz^2} - \frac{\omega^2}{c^2}\varepsilon(z)\mathbf{E_{0i}}(z) = 0, \tag{3.27}$$

in terms of scalar components ($i = x, y$). Eq. 3.24 is encountered in the several areas of physics and engineering and can be solved by the Wentzel-Kramers-Brillouin (commonly known as WKB) method with $k(z)$ satisfying

$$\left|\frac{1}{k(z)}\frac{dk(z)}{dz}\right| \ll k(z).$$

The solution obtained is

$$E_0(z) = \frac{constant}{\sqrt{k(z)}} \exp\left(i\int_0^z k(z)dz\right). \tag{3.28}$$

Hence

$$E(z,t) = E_0\sqrt{\frac{k(0)}{k(z)}} \exp\left[i\left(\omega t - \int_0^z k(z)dz\right)\right]. \tag{3.29}$$

The signs of ω and $k(z)$ in the exponential term have been so chosen such that the solution represents a wave progressing in the forward z direction.

3.3 Self-focusing of twisted light

Here, we investigate the self-focusing of the LG beams [2, 16, 46, 62] in a nonlinear medium using the Wentzel-Kramers-Brillouin (WKB) and the paraxial approximations [54, 60]. The Laguerre-Gaussian (LG) beams with a central hole singularity have been shown to play an important role in several areas of optics [3, 63]. Here, in this chapter, we have shown the self-focusing while taking into the account the LG modes with $p = 0$ and $\ell \neq 0$. In this case, the intensity cross-section perpendicular to the propagation direction consists of one bright ring with no on-axis intensity. This feature makes them ideal for applications in optical trapping and optical tweezers. Furthermore, as the LG beam can transfer the orbital angular momentum to the trapped particle, it can also act with a torque on the trapped particle [12, 27, 33, 64]. The LG tweezers can also trap metallic particles with a refractive index higher than that of the surrounding medium [65, 66].

All of these applications rely on the light scattering and hence they are related to the strength and the distribution of the intensity. The focusing and de-focusing are thus important, e.g. in the above context they allow the manipulation of the trapping spot size and the strength of the tweezers. This section is structured as follows: starting from the amplitude distribution of the LG beams propagating in a nonlinear dielectric medium, we derive a general differential equation for the beam width parameter. Utilizing the WKB and paraxial approximations, we derive an analytical expression for the intensity distribution as a function of the beam's parameters and the results are presented graphically and discussed. Finally a brief conclusion and future prospectives are also given.

3.3.1 Theoretical formulation

For investigation of the self-focusing phenomenon, mainly three theories are provided in the literature, which are:

1. Paraxial ray approximation
2. Moment theory
3. Variational approach

Here, we make use of the paraxial ray approximation (PRA) in the analytical derivations.

Paraxial ray approximation

The interaction of the electromagnetic Gaussian beams with a nonlinear medium is usually explained under the paraxial approximation, in which the irradiance and the eikonal (S) is expanded upto the first order in r^2 (r being the radial coordinate in a cylindrical polar system with the axis z chosen along the axis of the beam). This approximation ensures that the radial profile of the irradiance of a beam retains its nature during propagation in the nonlinear medium. Actually on account of the paraxial approximation, the eikonal (S) compensates for any distortion in the irradiance of the wave front during propagation and leads to an exact solution for the irradiance maintaining the Gaussian nature of the beam profile.

Self-focusing and de-focusing in a nonlinear medium

The amplitude distribution of the LG beam $u_{\ell p}^{LG}(r,\phi,z)$ in a cylindrical coordinate with z axis being along the beam propagation direction, is given as (for more details, see chapter 2)

$$\begin{aligned} u_{\ell p}^{LG}(r,\phi,z) &= \frac{C_p^{|\ell|}}{w(z)}\left(\frac{\sqrt{2}r}{w(z)}\right)^{|\ell|}\exp\left(\frac{-r^2}{w^2(z)}\right)L_p^{|\ell|}\left(\frac{2r^2}{w^2(z)}\right) \\ &\quad\times\exp\left(-i\frac{kr^2z}{2(z^2+z_R^2)} - i\ell\phi + i(2p+\ell+1)\arctan\left(\frac{z}{z_R}\right)\right), \end{aligned} \tag{3.30}$$

where r is the radial coordinate and ϕ is the azimuthal angle. $w(z) = w_0\sqrt{1+(z^2)/(z_R^2)}$ is the radius of the beam at z, and z_R is the Rayleigh range. w_0 is the beam waist at $z=0$. $L_p^{|\ell|}(x)$ is the associated Laguerre polynomial, $C_p^{|\ell|}$ is the normalization constant, and $(2p+\ell+1)\arctan\left(\frac{z}{z_R}\right)$ is the Guoy phase. At the beam waist, $z=0$, the amplitude of a Laguerre-Gaussian beam simplifies to

$$u_{\ell p}^{LG}(r,\phi,z=0) = \frac{C_p^{|\ell|}}{w_0}\left(\frac{\sqrt{2}r}{w_0}\right)^{|\ell|}\exp\left(\frac{-r^2}{w_0^2}\right)L_p^{|\ell|}\left(\frac{2r^2}{w_0^2}\right)\exp(-i\ell\phi). \tag{3.31}$$

We consider a nonlinear medium characterized by the dielectric function $\varepsilon = \varepsilon_0 + F(EE^*)$, i.e. $\varepsilon(r,z)$ depends upon the beam irradiance; the functional dependence of F is determined by the physical situation/mechanism under study. In turn $|E|^2$ depends on z in a manner yet to be determined. In the spirit of the paraxial approximation, we expand F in a Taylor series in powers of r^2 and retain terms up to r^2. This leads to

$$\varepsilon(r,z) \approx \varepsilon_0(z) - r^2\varepsilon_2(z). \tag{3.32}$$

In the wave equation governing the propagation of the laser beam

$$\nabla^2 E + \frac{\omega^2}{c^2}\varepsilon E + \nabla\left(\frac{E\,\nabla\varepsilon}{\varepsilon}\right) = 0 \tag{3.33}$$

the third term can be neglected if $k^{-2}\nabla^2(\ln\varepsilon) \ll 1$, where k is the wave number. This inequality is satisfied in almost all cases of practical interest. For a cylindrically symmetric beam a solution for

$$\nabla^2 E + \frac{\omega^2}{c^2}\varepsilon E = 0 \tag{3.34}$$

we obtain using WKB and the paraxial approximation Refs. [54, 60] as

$$E(r,\phi,z) = A(r,\phi,z)\exp[i(\omega t - kz)], \tag{3.35}$$

where $k = \frac{\omega}{c}\sqrt{\varepsilon_0}$ and $A(r,\phi,z)$ is the complex amplitude of the electric field. Substituting for $E(r,\phi,z)$ and neglecting $\frac{\partial^2 A}{\partial z^2}$ on the basis of WKB approximation which implies that the characteristic distance of intensity variation is much greater than the wavelength. We obtain

$$2ik\frac{\partial A}{\partial z} = \frac{\partial^2 A}{\partial r^2} + \frac{1}{r}\frac{\partial A}{\partial r} + \frac{1}{r^2}\frac{\partial^2 A}{\partial \phi^2} - \frac{\omega^2}{c^2}\varepsilon_2 r^2 A. \tag{3.36}$$

To solve Eq. 3.36 we express $A(r,\phi,z)$ as

$$A(r,\phi,z) = A_0(r,z)\exp[i(-kS(r,z) - \ell\phi)] \tag{3.37}$$

where A_0 and S are real functions of r, ϕ and z. The eikonal S is

$$S = \frac{r^2}{2}\beta(z) + \Theta(z). \tag{3.38}$$

$\Theta(z)$ is an additive function whereas

$$\beta(z) = \frac{1}{f}\frac{df}{dz}. \tag{3.39}$$

The parameter $\beta(z)$ is the curvature of the wavefront. Substituting for $A(r,\phi,z)$ and S from Eq. 3.38 and Eq. 3.39 in Eq. 3.37, one obtains

$$2\frac{\partial S}{\partial z} + \left(\frac{\partial S}{\partial r}\right)^2 = \frac{1}{k^2 A_0}\left[\frac{\partial^2 A_0}{\partial r^2} + \frac{1}{r}\frac{\partial A_0}{\partial r} - \frac{\ell^2}{r^2}A_0\right] - \frac{\varepsilon_2}{\varepsilon_0}r^2, \tag{3.40}$$

$$\frac{\partial A_0^2}{\partial z} + \frac{\partial A_0^2}{\partial r}\frac{\partial S}{\partial r} + A_0^2\left(\frac{\partial^2 S}{\partial r^2} + \frac{1}{r}\frac{\partial S}{\partial r}\right) = 0. \tag{3.41}$$

The solution of Eq. 3.40 for the LG beam can be written as

$$A_0(r,z) = \frac{E_0}{f}\left(\frac{\sqrt{2}r}{w_0 f}\right)^{|\ell|}\exp\left(\frac{-r^2}{w_0^2 f^2}\right)L_P^{|\ell|}\left(\frac{2r^2}{w_0^2}\right). \tag{3.42}$$

For $\ell = 1$ and $p = 0$, substituting for S and A_0 from Eq. 3.38, Eq. 3.42 in Eq. 3.40, yields

$$\frac{1}{f}\frac{d^2 f}{dz^2} = \frac{4c^2}{\omega^2 \varepsilon_0(z) w_0^4 f^4} - \frac{\varepsilon_2(z)}{\varepsilon_0(z)}. \tag{3.43}$$

Eq. 3.43 can always be solved by considering the conditions

$$f = 1 \quad \text{and} \quad \frac{df}{dz} = 0 \text{ at } z = 0. \tag{3.44}$$

It is, however, convenient to reduce Eq. 3.43 to a dimensionless form by transforming the coordinate z to the dimensionless distance of propagation

$$\xi = \frac{zc}{w_0^2 \omega} \tag{3.45}$$

and the beam width w_0 to the dimensionless beam width

$$\rho = \frac{w_0 \omega}{c} \tag{3.46}$$

Substituting Eq. 3.45 and Eq. 3.46 in Eq. 3.43 yields

$$\frac{\varepsilon_0(z)}{f}\frac{d^2 f}{d\xi^2} = \frac{4}{f^4} - \rho^2 w_0^2 \varepsilon_2(z). \tag{3.47}$$

In case of a parabolic nonlinearity, that is when the nonlinear term is proportional to E^2, we have the r dependent term

$$\varepsilon_2(f) r^2 = \frac{\alpha E_0^2}{f^2}\frac{r^2}{w_0^2 f^2} \tag{3.48}$$

where α is a constant. Substitution of $\varepsilon_2(f)$ in Eq. 3.47 yields

$$\frac{d^2 f}{d\xi^2} = \frac{1}{\varepsilon_0 f^3}(4 - \rho^2 \alpha E_0^2). \tag{3.49}$$

The analytical solution of Eq. 3.49 under the conditions Eq. 3.44 is

$$f = \sqrt{\frac{\varepsilon_0 + 4\xi^2 - E_0^2 \alpha \xi^2 \rho^2}{\varepsilon_0}}. \tag{3.50}$$

For further analysis, it is useful to write Eq. 3.49 in the form

$$\frac{d^2 f}{dz^2} = \frac{c^2}{\varepsilon_0 w_0^4 \omega^2}\left(4 - \frac{\alpha w_0^2 \omega^2}{c^2} E_0^2\right) f^{-3}. \tag{3.51}$$

3.3.2 Results and discussion

Eq. 3.49, or Eq. 3.51 is the fundamental second order differential equation governing self-focusing/defocusing of the LG beams in a parabolic medium. Essentially, the effect of the non-linearity is dictated by the second term on the right side of Eq. 3.49, or Eq. 3.51.

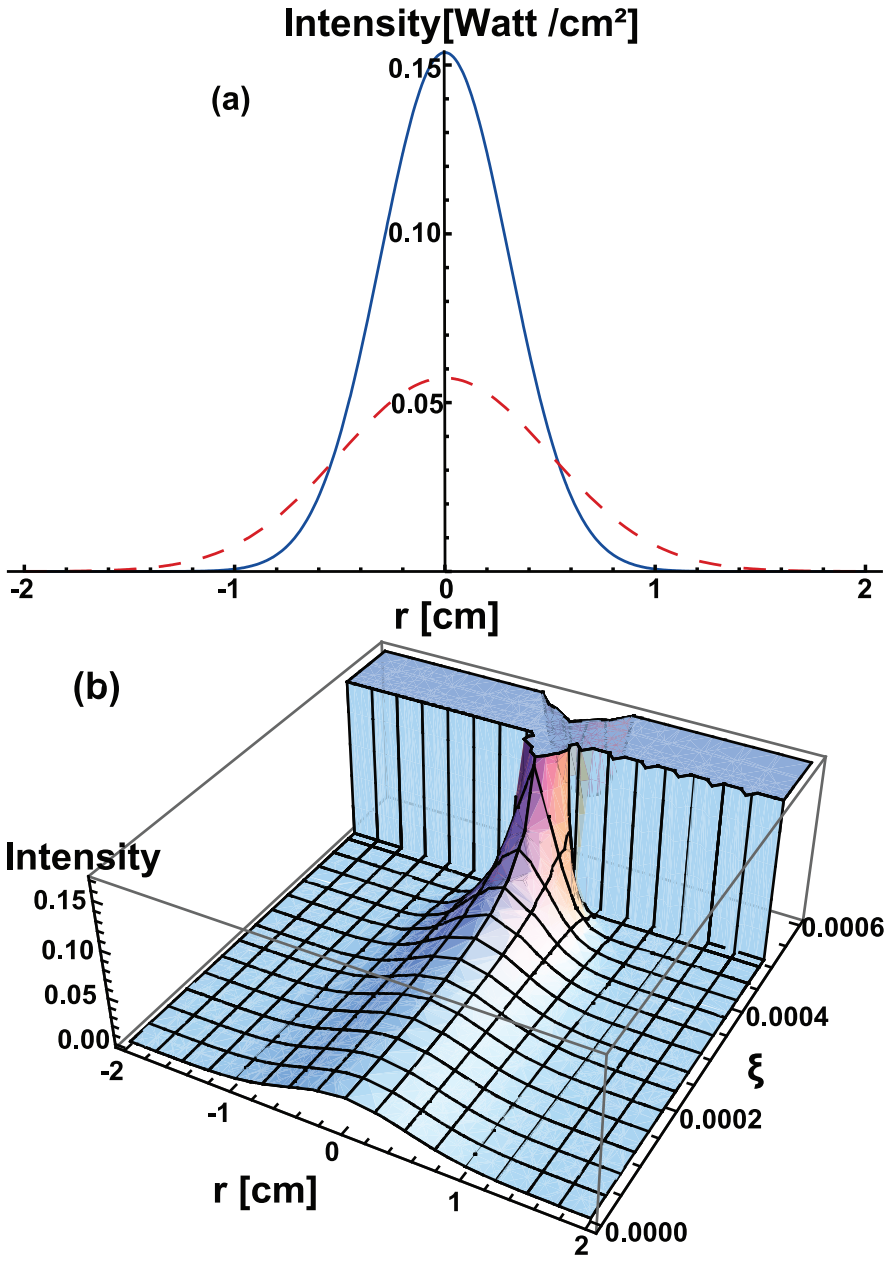

Figure 3.3: a) Intensity (in CGS units) of the Gaussian beam (i.e. $\ell = 0$, and $p = 0$) verses the radial distance from the propagation direction (in cm). The angular frequency is $\omega = 2 \times 10^{14}$ rad/sec, $w_0 = 1$ cm, $\epsilon_0 = 1$, $\alpha = 1$, $E_0 = 0.3$ StatV/cm, $\rho = 0.66 \times 10^4$, b) Initial intensity profile (dotted curve) compared to the propagated intensity at $\xi = 4 \times 10^{-4}$.

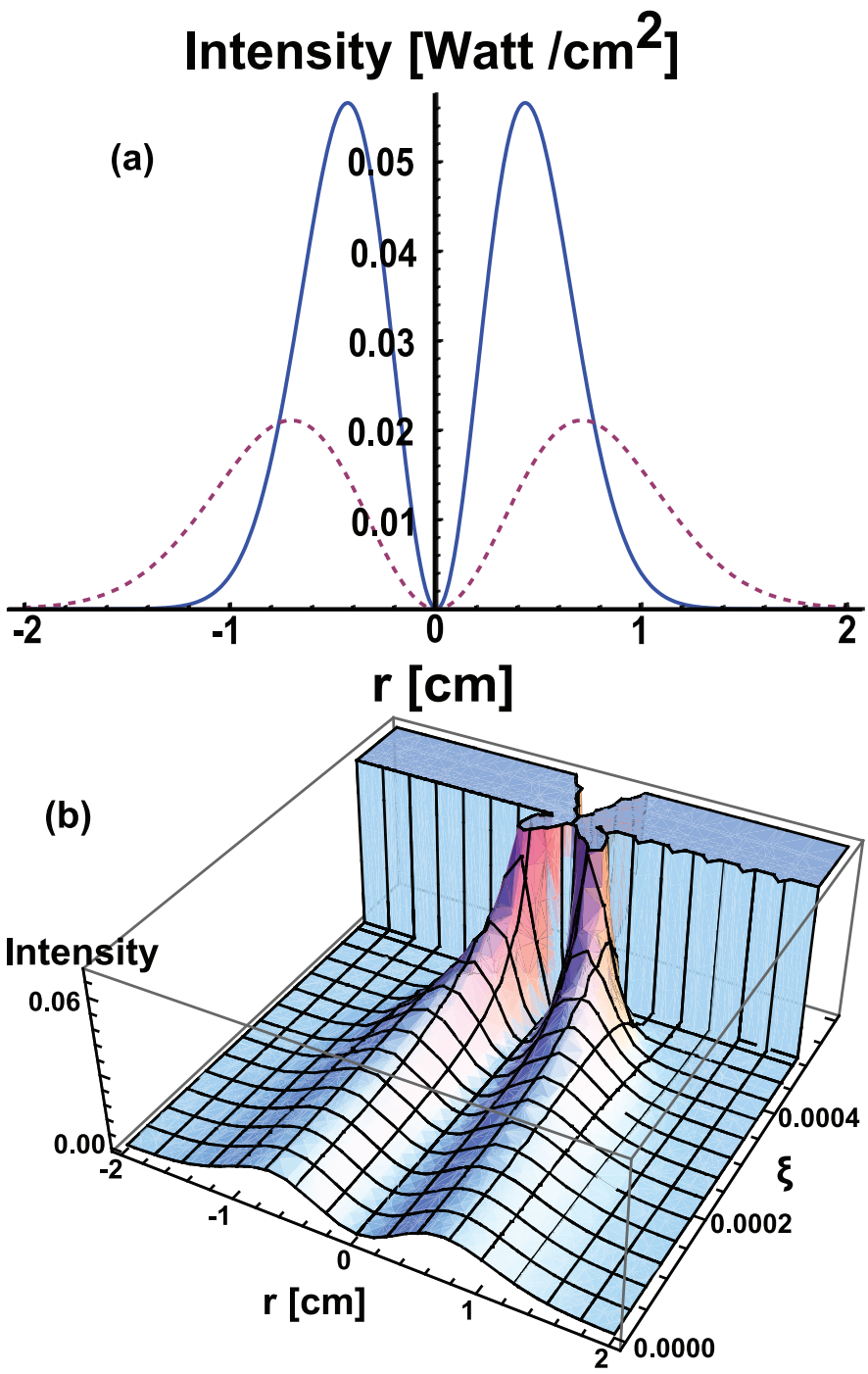

Figure 3.4: a) Intensity (in CGS units) of the LG beam verses the radial distance from the propagation direction (in cm) for the $\ell = 1$, and $p = 0$. The angular frequency is $\omega = 2 \times 10^{14}$ rad/sec, $w_0 = 1$ cm, $\epsilon_0 = 1$, $\alpha = 1$, $E_0 = 0.3$ StatV/cm, $\rho = 0.66 \times 10^4$, b) Initial intensity profile (dotted curve) compared to the propagated intensity at $\xi = 4 \times 10^{-4}$.

In the absence of this term $\frac{d^2 f}{d\xi^2}$ remains positive causing the beam width parameter

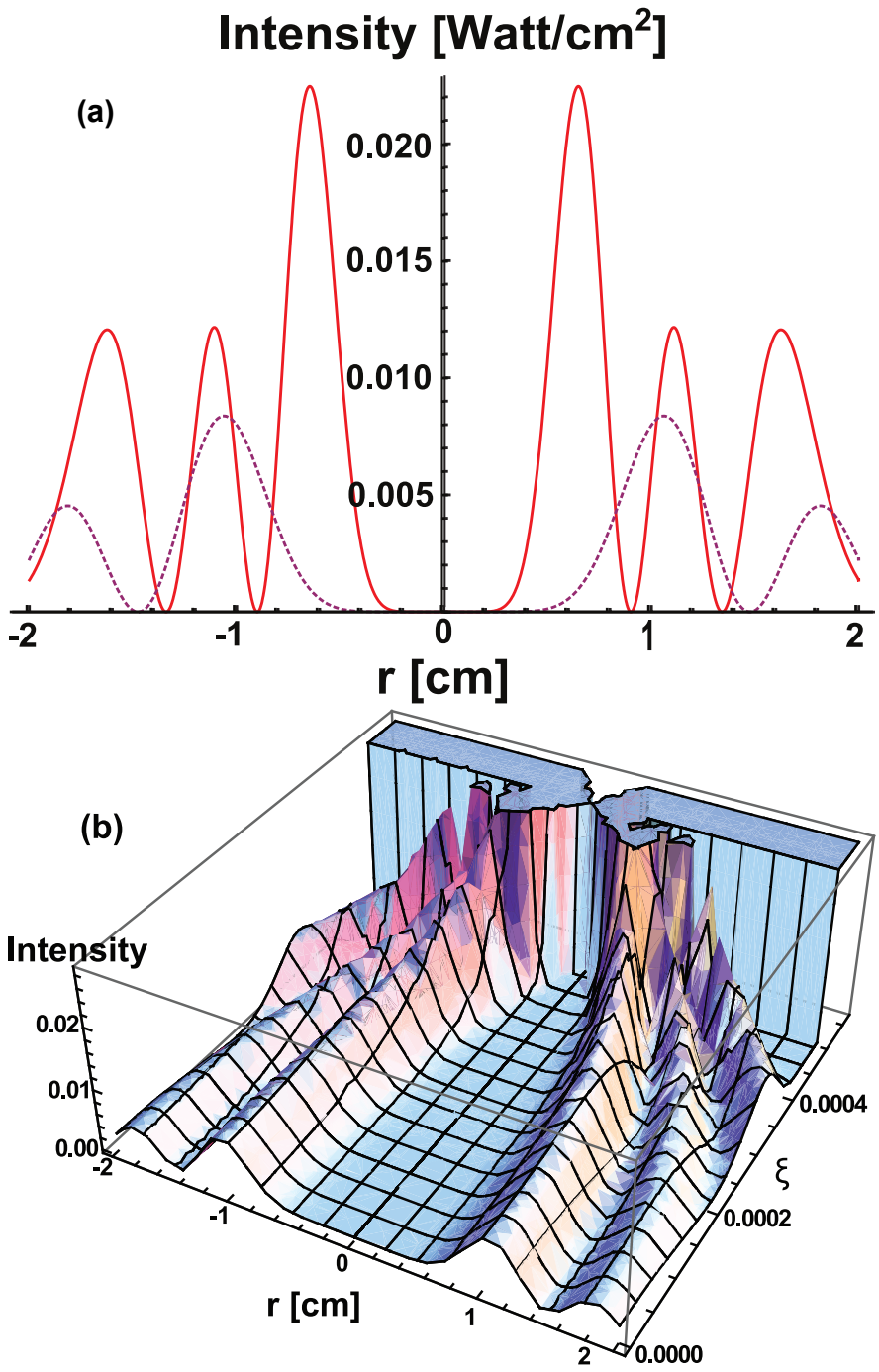

Figure 3.5: a) Intensity (in CGS units) of LG beam verses the radial distance from the propagation direction (in cm) for the $\ell = 5$, and $p = 2$. The angular frequency is $\omega = 2 \times 10^{14}$ rad/sec, $w_0 = 1$ cm, $\epsilon_0 = 1$, $\alpha = 1$, $E_0 = 0.3$ StatV/cm, $\rho = 0.66 \times 10^4$, b) Initial intensity profile (dotted curve) compared to the propagated intensity at $\xi = 4 \times 10^{-4}$.

(f) to increase continuously leading to a steady divergence. This effect is the natural diffraction divergence. The second term containing the nonlinear effect is negative and acts in the opposite direction tending to converge the beam. The convergence (fo-

cusing) or divergence (de- focusing) of the beam depends on which of the two terms predominates. Eq. 3.51 makes also clear that for the focusing the product $(w_0\omega E_0)^2$ is relevant, i.e. for a focused beam the frequency has to be increased when the intensity (or the waist) is lowered to maintain focusing. Fig. 3.3, Fig. 3.4 and Fig. 3.5 illustrate the focusing effects for the Gaussian and the LG beam for typical feasible parameters. In the case of Gaussian beam (Fig. 3.3), the maximum intensity can be seen at center due to its beam's profile structure whereas Fig. 3.4 proves the concept of minimum intensity at the center of the LG beam. Fig. 3.5 reveals the focusing effects for the higher modes LG beam where the intensity is decreasing with an increase in the value of a radial mode, p, which is due to the intensity distribution of electric field. From these figures (Figs. 3.3, 3.4, 3.5), it is clear that the focusing and an intensity increase occur until a certain value of the normalized distance of propagation (ξ) = 0.00062, after that de-focusing sets in. This is due to the fact that at higher intensity nonlinear refractive term dominates over the diffractive term for some initial distance of propagation after that the diffractive term strongly overcomes the nonlinear refractive term and therefore the beam de-focuses. From Fig. 3.4 and Fig. 3.5, it is also obvious that the focusing effect can be utilized, e.g. for creating tighter and stronger three-dimensional optical traps by crossing the two LG beams at the focused distance.The predicted focusing effect can also be used for the realization of more versatile optical tweezers. From Eq. 3.51, we infer that to achieve results similar to those in Fig. 3.4 and Fig. 3.5 for a smaller starting waist one has either to increase the intensity (or the frequency) by roughly the same amount.

3.3.3 Conclusions

We studied the self-focusing of twisted light in a nonlinear dielectric medium by using the WKB and paraxial approximations. The differential equation for the beam width parameter (f) is solved analytically. The occurrence of the focusing is pointed out and its dependence on the beam's parameters is worked out analytically and illustrated by numerical calculations. We have compared the focusing effects for both the Gaussian and the higher modes LG beam and shown that the focusing can be seen only at certain value of distance of propagation and after that the de-focusing occur. It can be explained either on the basis of excess heating of the laser beam which results into the breakdown of the system or by the paraxial approximation which drops down after a certain limit of the propagation distance . The practical applications of the predicted effect are pointed out in the field of optical trapping and will be explained thoroughly in chapter 5.

Chapter 4

Reflection and transmission of twisted light at phase conjugating interfaces

In the recent years, the light beam with the orbital angular momentum (OAM) [3, 17, 46, 58, 67–69] has emerged as a new and exciting form of light that has a varying phase structure as it propagates through space. They occur as a particular solution to the wave equation in cylindrical coordinates and have drawn a major attention, particularly in the field of the optical manipulation and characterization of materials. So, in this chapter while introducing the concept of optical phase conjugation and the methods of generating it. We will report the study on the transmission and the reflection of the light beams carrying orbital angular momentum (OAM) considering a dielectric multilayered structure (Fig. 4.15) with phase conjugating interfaces [70]. We will present the results analytically and demonstrate numerically that the phase conjugation at the interfaces results in a characteristic angular and radial pattern of the reflected beam (Fig. 4.17 and Fig. 4.18). A fact which can be exploited for the detection and the characterization of phase conjugation in composite optical materials.

4.1 Introduction to Optical phase conjugation (OPC)

Optical phase conjugation (OPC) is a process which involves the use of nonlinear optical effects to precisely reverse the direction of propagation of each plane wave in an arbitrary beam of light, thereby causing the return beam to exactly retrace the path of the incident beam. This nonlinear optical process is also known as **wavefront reversal**, **time reversal reflection** or **retro-reflection** [71, 72]. When the light strikes the mirror normal to its surface, gets reflected straight back the way it came which is true for both the cases, i.e, either from the plane mirror (Fig. 4.1(A)) or the phase conjugate mirror (Fig. 4.1(B)). However, when the light strikes the plane mirror at an angle, it reflects back in the opposite direction such that the angle of incidence (i) is equal to the angle of reflection (r) Fig. 4.1(C) which is not true in case of the phase conjugate mirror(as it doesn't matter what the angle of incidence) Fig. 4.1(D). The reflection from both the mirrors have significant consequences which can be explained while placing an irregu-

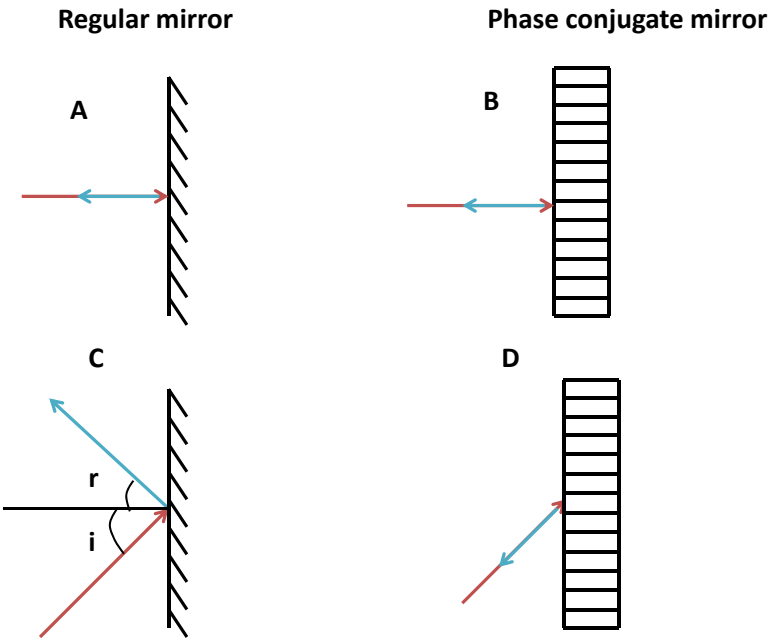

Figure 4.1: A comparison between reflection from a regular and phase conjugate mirror.

lar distorting glass in the path of a beam of light. In the normal mirror, the parallel rays get bent in random directions, and after reflection, each ray of light is bent even farther, and the beam is scattered as depicted in Fig. 4.2. But the situation, in case of the phase

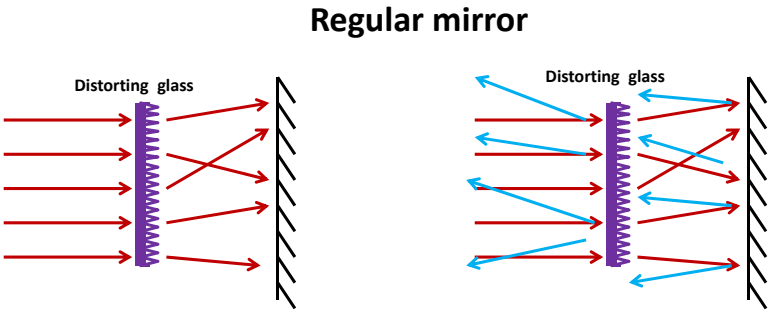

Figure 4.2: Reflection from a distorting glass in case of a regular mirror.

conjugate mirror is entirely different, each ray is reflected back in the direction it came from and therefore reflected conjugate wave propagates backwards through the distorting medium, and removed the influence of the distortion, and returns to a coherent beam of parallel rays traveling in the opposite direction as shown in Fig. 4.3. These remarkable image-transformation properties (even in the presence of a distorting optical element) are of interest for potential applications such as holography, mirror optics, optical fibers, optical trapping and many more [73]. These unique features of the phase conjugating mirrors are also confirmed by various experimental studies [74, 75]. The optical phase conjugated waves can be categorized into two main classes i.e., degen-

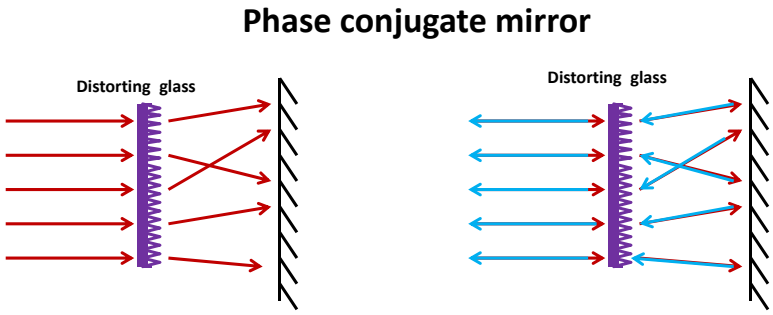

Figure 4.3: Reflection from a distorting glass in case of a phase conjugate mirror.

erate and non-degenerate backward PCW and forward PCW and their mathematical definitions are summarized below in the flow chart (Fig. 4.4) [73].

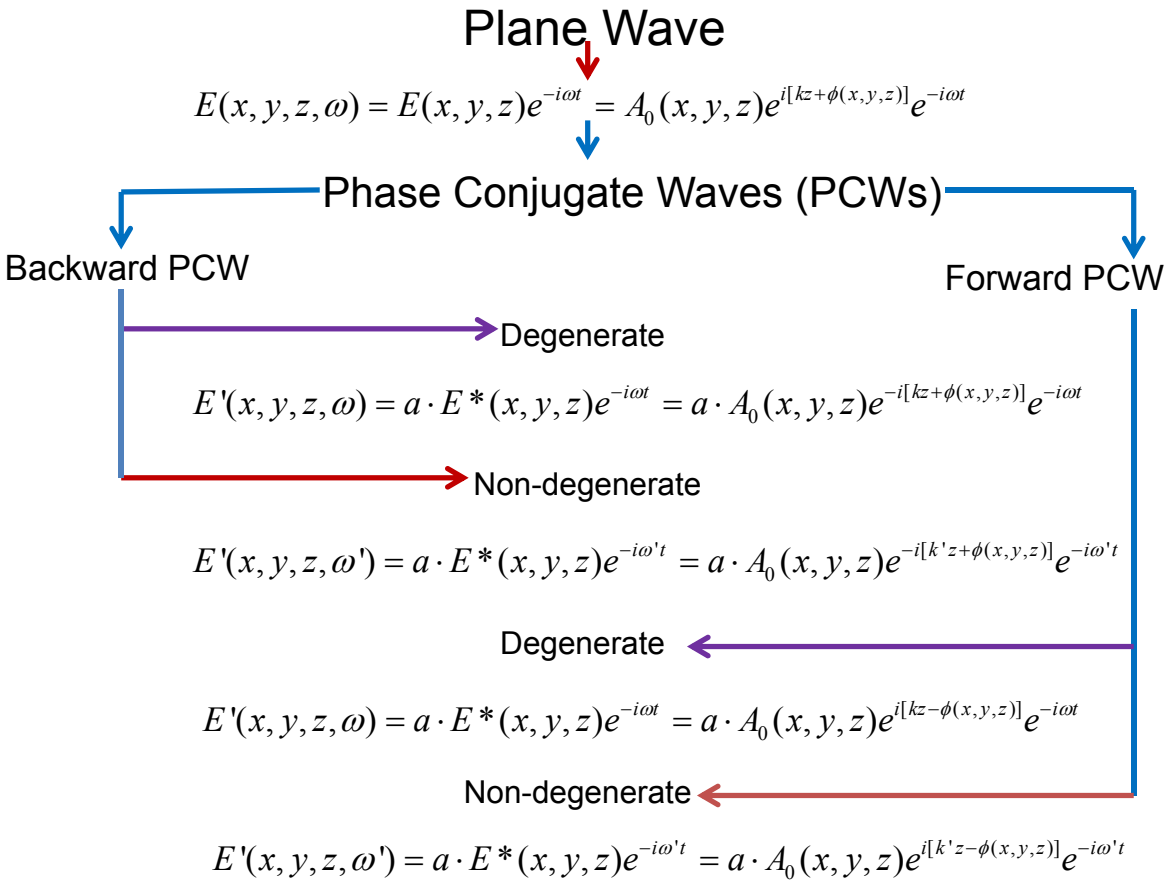

Figure 4.4: Features of phase conjugating mirror (PCM).

4.2 Photo-refractive materials

The photo-refractive effect is a nonlinear process which refers to a change in the refractive index of a material caused by light. This effect occurs due to the interference pattern of dark and light fringes by coherent beams of light while illuminating on photo-refractive materials. The photo-refractive materials like lithium niobate ($LiNbO_3$), lithium tantalate ($LiTaO_3$), barium titanate ($BaTiO_3$), potassium tantalate niobate ($KTa_{1-x}Nb_xO_3$), bismuth silicon oxide ($Bi_{12}SiO_{20}$), bismuth germanium oxide ($Bi_{12}GeO_{20}$), gallium arsenide (GaAs) and indium phosphide (InP) etc. [76] are the excellent materials for recording volume phase holograms in real-time as they are considered to be rich in resolution, efficiency, storage capacity, sensitivity and reversibility. The table (Tab. 4.1) gives the comparison between the extended class of photo-refractive materials.

Photorefractive Materials

	Ferroelectric Oxides	Cubic Oxides of the Sillenite family	Semi-insulating compound semiconductors
Electro-optic Coefficients	Large electro-optic coefficients which leads to large nonlinear effects.	Small electro-optic coefficients.	They have electro-optic coefficients similar in magnitude to the sillenites.
Photo-Sensitivity	Small charge carrier mobilities and large dielectric constants cause poor sensitivity.	Better sensitivity than ferroelectric because of larger photo-conductivities.	They are near the theoretical limit of sensitivity.
Wavelength	They are sensitive at visible wavelengths.	They are sensitive at Infra red wavelengths.	They are sensitive near Infra red wavelength band.
Examples	For e.g: Lithium Niobate ($LiNbO_3$), Barium Titanate ($BaTiO_3$), Potassium Niobate ($KNbO_3$).	For e.g: $Bi_{12}SiO_{20}$, $Bi_{12}GeO_{20}$, $Bi_{12}TiO_{20}$.	For e.g: GaAs, InP, CdTe, CdS, SbSI.

Table 4.1: Photorefractive materials and their characteristics.

In the above mentioned materials, the OPC can be generated at low light intensities using a degenerate four-wave mixing (DFWM) process with a lower power He-Ne laser at 633 nm and holographic processes with a maximum phase conjugated beam reflectivity of about 0.24 %. The generation of the phase conjugated (PC) wave from both the processes i.e. DFWM and holographic process can be differentiated on the behavior of intensity of PC signal as a function of time as shown in Fig. 4.5 via illu-

minating the material with three waves E_1 (forward pump beam), E_2 (backward pump beam) and E_3 (probe beam) from He-Ne laser. It has been observed that initially there will be a rise in the peak corresponding to the intensity of PC signal for few minutes due to the presence of both DFWM and holographic processes. But if the waves E_1 and E_3 get switched off, one can see the slow decay in the intensity of PC signal which shows that the waves E_1 and E_3 are due to DFWM whereas the beam E_2 is the contribution from holographic process as PC signal still remains present even in the absence of other two beams (i.e. E_1 and E_3).

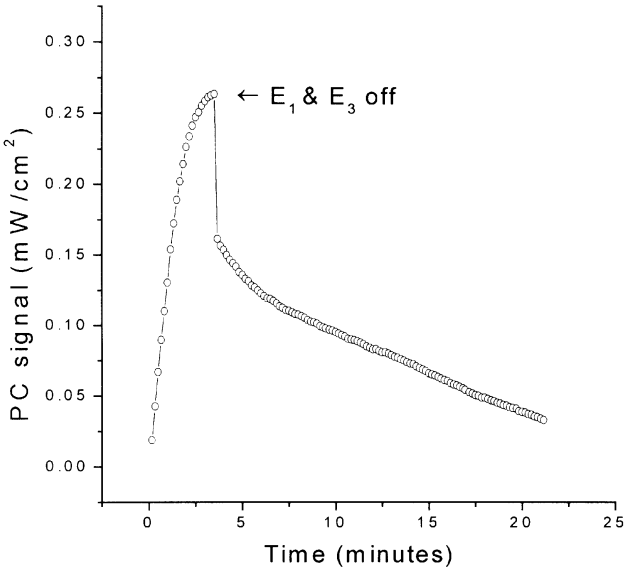

Figure 4.5: Measured PC signal as a function of recording time [77].

Similar studies have also been carried out in the semiconductor doped glasses (for e.g. CdS_xSe_{1-x} [78]) which can be commercially found in the form of colored glass filters. These glasses also referred as Selenium ruby glasses which are able to exhibit third order nonlinearities of $10^{-9}-10^{-8}$ esu using DFWM with short (10 nsec) laser pulses at various visible wavelengths and efficient to observe a phase conjugated beam reflectivity up-to 10 %. Table. 4.2 summarizes the third order susceptibilities measured by DFWM in CdS_xSe_{1-x} glasses at different wavelengths. Even, the OPC has also been observed by the picosecond pulses using photo-refractive $Sn_2P_2S_6$ crystals [79]. The phase conjugated reflectiveness up to 45 % is achieved by 7.2 ps pulses at 1.06 μm with an intensity 23 W/cm^2 which is two orders of magnitude faster as $BaTiO_3$:Rh [80].

Wave-length λ (nm)	Appropriate Glass Composition (Sulfur Fraction) (x)	Representative Commercial Glass	Measured $\chi^{(3)}$ (esu)
532.0	~0.9	Corning #3484 (CS3-68)	$\sim 1.3 \times 10^{-8}$
580.0	~0.7	Corning #2434 (CS2-73)	$\sim 5 \times 10^{-9}$
694.3	~0.1	Schott RG 695	$\sim 3 \times 10^{-9}$

Table 4.2: Representative choices of wavelengths, corresponding CdS_xSe_{1-x} glasses, and third-order susceptibilities measured by DFWM [78].

4.3 Methods to produce phase conjugated waves (PCW)

Generally, there are three major methods for the generation of backward phase conjugated waves (PCW) which are explained in the below subsections.

1. Degenerate four wave mixing process [81, 82].
2. Various stimulated (Brillouin, Raman, Rayleigh-wing or Kerr) scattering processes [7, 83].
3. Stimulated emission (lasing) processes which exhibit the same phase conjugation property as backward stimulated scattering under appropriate conditions [73, 84, 85].

Whereas, the forward PCW [73, 86] are generated by the forward wave mixing in the similar fashion as backward within appropriate conditions. Here, we have confined ourselves in explaining the generation method of backward phase conjugated waves (PCWs) only.

4.3.1 Backward degenerate four wave mixing (DFWM)

It was Hellwarth in 1977 who firstly proposed the backward DFWM process [81]. In DFWM, a nonlinear medium is illuminated simultaneously with two counter propagating strong plane waves and a signal beam with an arbitrary wavefront distortion and different propagation direction as shown in Fig. 4.6. Then, if all these incident beams have the same frequency ω, one may observe a newly generated wave with the same frequency ω along the opposite propagation direction of the signal beam. This newly generated wave is then called the backward frequency degenerate PCW of the incident signal beam. In order to realize the whole process, let's consider a signal beam propagating along the z-axis, then the three incident monochromatic waves can be written

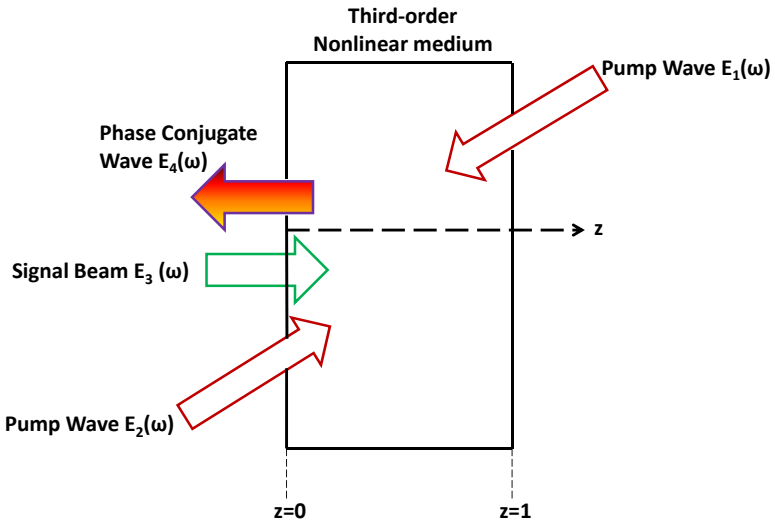

Figure 4.6: Backward phase conjugation wave generation by DFWM.

as

$$\mathbf{E}_1(\omega) = \mathbf{a}_1 A_1(\mathbf{r}) e^{-i(\omega t - \mathbf{k}_1 \cdot \mathbf{r})}, \tag{4.1a}$$
$$\mathbf{E}_2(\omega) = \mathbf{a}_2 A_2(\mathbf{r}) e^{-i(\omega t - \mathbf{k}_2 \cdot \mathbf{r})}, \tag{4.1b}$$
$$\mathbf{E}_3(\omega) = \mathbf{a}_3 A_3(z) e^{-i(\omega t - k_3 z)}. \tag{4.1c}$$

Here, $\mathbf{a}_1$ is a unit vector along the light's polarization direction of the ith wave, $\mathbf{k}_1 = -\mathbf{k}_2$ is the wave vector of the pump wave, k_3 is the absolute value of the wave vector of the signal beam, A_1 and A_2 are the real amplitude functions of the two plane pump waves, and A_3 is the complex amplitude function of the signal wave. The fourth coherent wave will be produced through the third order nonlinear polarization response of the medium according to the working principle of four wave mixing process. Thus, the newly generated phase conjugated wave with propagation direction along $-z$ axis can be written as

$$\mathbf{P}_4^{(3)}(\omega) = \varepsilon_0 \chi^{(3)}(\omega, \omega, -\omega) \mathbf{a}_1 \mathbf{a}_2 \mathbf{a}_3 A_1 A_2 A_3^* e^{-i(\omega t + k_3 z)}, \tag{4.2a}$$
$$\mathbf{E}_4(\omega) = \mathbf{a}_4 A_4(z) e^{-i(\omega t + k_3 z)}. \tag{4.2b}$$

In the above process, the phase matching condition is always satisfied because $\mathbf{k}_1 + \mathbf{k}_2 = \mathbf{k}_3 + \mathbf{k}_4 = 0$, as a result, the signal wave will always get amplified while the wave $\mathbf{E}_4$ is created.

4.3.2 Backward non-degenerate four wave mixing (NDFWM)

The generation of PCW via non-degenerate FWM process can be explained on the basis of induced holographic model [86]. According to the principle of holography, the two beams of the same frequency are used to produce the hologram while the

another beam with a different frequency is used to read the hologram. In this case, the diffracted beam has the same frequency as the reading beam, but the reconstructed spatial structure of this beam may be influenced by the wavelength difference between the recording beam and the reading beam. Fig. 4.7(a) shows the generation of the backward non-degenerate PCW via partially degenerate FWM in a non-linear medium where the pump wave $A_1(\omega_1)$ and the signal wave $A_3(\omega_1)$ have the same frequency and the same polarization state (which is the essential condition to produce the phase grating) and thus create an induced phase grating. While, the reading wave $A_2(\omega_2)$ with another frequency will create the diffracted wave $A_4(\omega_2)$ through the induced grating. The spatial information carried by the signal wave $A_3(\omega_1)$ can be restored in the wave $A_4(\omega_2)$; in other words, the latter is the frequency non-degenerate PCW of the former. Similarly, in the case shown in Fig. 4.7(b) the waves $A_2(\omega_1)$ and $A_3(\omega_1)$ have the same frequency and polarization state and can produce the grating, while the reading wave $A_1(\omega_2)$ with another frequency will create the diffracted wave $A_4(\omega_2)$. In this case, the wave $A_4(\omega_2)$ is phase-conjugated with $A_3(\omega_1)$ [87].

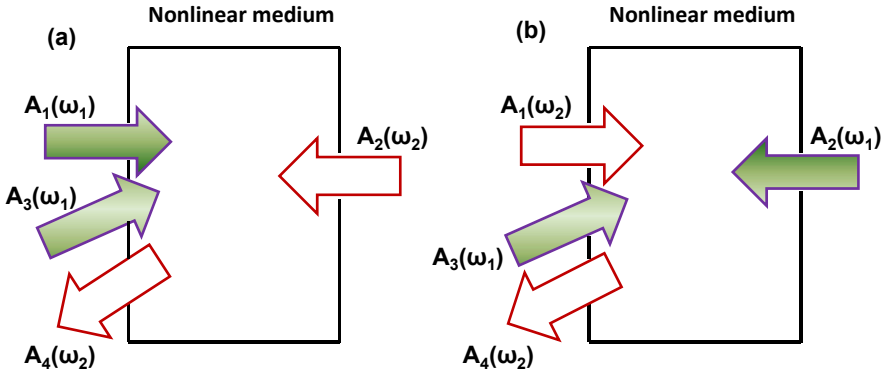

Figure 4.7: The generation of the backward non-degenerate PCW via partially degenerate FWM in a non-linear medium.

4.3.3 Backward stimulated scattering (BSS)

This method of producing phase conjugated wave was firstly observed by Zel'dovich et. al [7] in 1972 which required a strongly focused laser beam to pump a given scattering medium, which results into the generation of the backward stimulated scattering beam, which is exactly a phase conjugate of the input pump beam, under appropriate conditions. Fig. 4.8 shows an experimental set up, where a single axial mode ruby laser is taken as a pump source and the pump beam is made to pass through an abberation plate. The pump beam is then focused onto the scattering medium (here, in the above shown set-up a high pressure CF_6 gas filled in a 94 cm long cell has been taken as a scattering medium) which induces a special holographic process due to the intensity dependent refractive index changes of the medium. Thus, after passing through the same abberation plate, the spatial structure of the backward stimulated Brillouin scattering (SBS) is a phase conjugated wave of the incident pump beam. It has also been

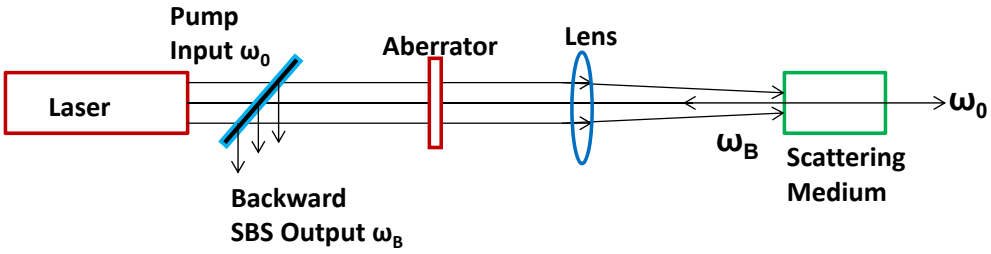

Figure 4.8: Experimental setup for observing phase conjugation behavior of backward stimulated scattering (BSS) [7].

observed that the divergence of the input beam which was 0.182 mrad at wavelength $\lambda_0 = 694.3$ nm after passing through the abberation plate get increased to ~ 3.5 mrad. If a plane wave is put in the path of pump beam and after allowing the reflected pump beam to pass the aberrator second time, it would further increase the beam divergence to ~ 6.5 mrad. On the contrary, it has been seen that the abberation influence imposed on an input pump beam automatically gets canceled in the backward SBS beam after passing through the same aberrator [7]. A clear picture of the abberation correction by backward SBS is shown in Fig 4.9 [88] which shows the intensity distributions and photographs of far field patterns of the original pump beam, the aberrated beam and the aberrated-corrected backward SBS beam from CS_2 liquid.

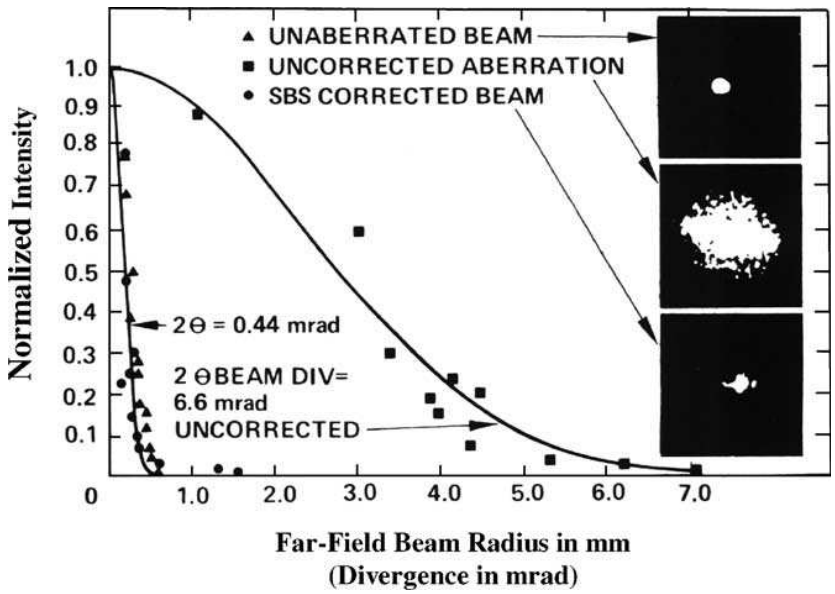

Figure 4.9: Normalized far field intensity distributions and photographs for the original pump beam, the aberrated pump beam, and the aberrated-corrected backward SBS beam [88].

All the various scattering mechanisms which clearly demonstrate the phase conju-

gation properties of backward stimulated scattering can be explained on the basis of a quasi collinear FWM model (Fig. 4.10) proposed in 1985 – 1986 [89–91]. This model is based on Gabor's idea of holograph which states that "When a coherent light wave pass through a transparent object (phase object), the object is assumed to be such that a considerable part of the wave penetrates undisturbed through it, and a hologram is formed by the interference of the secondary wave arising from the presence of the object with the strong background wave" [91]. According to this principle, after passing through a phase object, the total optical field can be expressed as a superposition of two portions [91]:

$$U = U^{(i)} + U^{(s)} = A^{(i)}e^{i\phi_i} + A^{(s)}e^{i\phi_s} = e^{i\phi_i}[A^{(i)} + A^{(s)}e^{i(\phi_s-\phi_i)}]. \tag{4.3}$$

where $U^{(i)}$ is the undisturbed part of the transmitted field, $U^{(s)}$ is the disturbed part arising from the presence of the object, $A^{(i)}$ and $A^{(s)}$ are their amplitude functions, and ϕ_i and ϕ_s are the corresponding phase functions respectively.

Fig. 4.10 shows the non-degenerate FWM model for the phase formation of backward stimulated scattering. Here $E(\omega_0)$ is a quasi-plane pump wave which after pass-

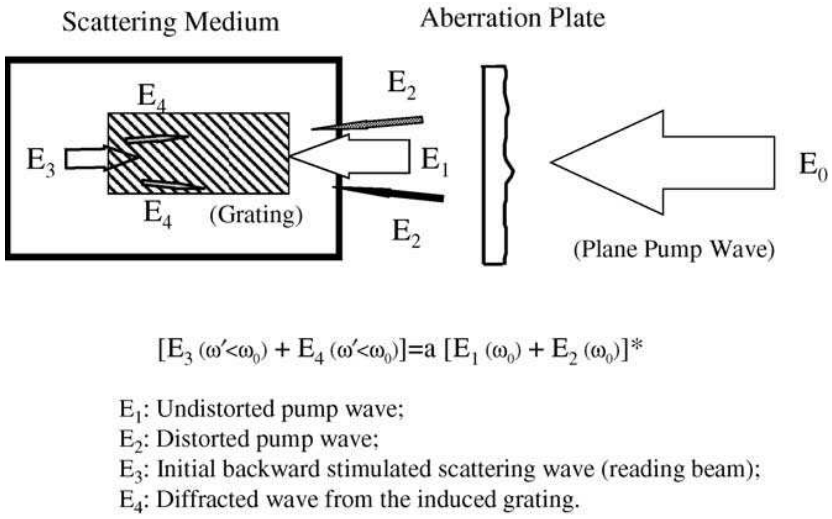

Figure 4.10: Schematic illustration of the non-degenerate FWM model for the phase formation of backward stimulated scattering [73].

ing through an aberration plate or a phase subject decomposes itself as a superposition of two portions; $E_1(\omega_0)$ (a stronger undisturbed wave) and $E_2(\omega_0)$ (a weaker distorted wave). The interference of these two waves ($E_1(\omega_0)$, $E_2(\omega_0)$) in a scattering medium will then create an induced volume holographic grating due to the intensity-dependent refractive index changes of the medium. In this process, only the undisturbed pump wave $E_1(\omega_0)$ (also named as reference beam) is strong enough to fulfill the threshold requirement and to generate an initial BSS wave $E_3(\omega')$ (referred as reading beam) that exhibits a regular wavefront as wave $E_1(\omega_0)$. When wave $E_3(\omega')$ passes back through the induced holographic grating region, a diffracted wave $E_4(\omega')$ which will be the

phase conjugate replica of the $E_2(\omega_0)$ wave can be created. Moreover, the wave $E_4(\omega')$ will experience an amplification with the wave $E_3(\omega')$ together because both the waves have the same scattering frequency.

From the above explanation, it can be concluded that the pump field-induced holographic grating is the common mechanism for the generation of the phase-conjugation by using either FWM or BSS method except the difference in the former, only two waves (the signal wave and the backward diffracted wave) are phase-conjugate to each other whereas in the latter, the sum of the two portions of the BSS beam should be phase-conjugated to the sum of the two portions of the input pump beam.

4.4 Reflection and transmission of LG beams

Recently, the behavior of the LG beams at dielectric interfaces have been the subject of several studies showing that the beam-interface interactions are dependent on the incident angles of the LG beams. In the case of normal incidence, the azimuthal index of the reflected or the transmitted LG beam is increased and decreased by the cross-polarization coupling in the beam component of the incident beam [92–94]. In this section, we have shown the results on the propagation of twisted light in a multilayered dielectric medium containing interfaces which act as phase-conjugating mirrors (PCM) [7–9,71]. There are several popular methods for the realization of optical phase conjugation which have already been described in Section 4.3 thoroughly. The treatment of the propagation of the LG beam for a single PCM has also been addressed previously [8,9]. As in the work of Okulov [8], the time reversal property of the phase conjugating mirror has revealed experimentally on the basis of stimulated brillouin scattering (SBS). They demonstrated the hidden anisotropy of an SBS mirror due to excitation of internal helical waves whose existence has been proved for MHz range sound [95].

A very nice comparison between a conventional mirror (M, bottom) and a wavefront reversal mirror (PCM, upper) can be seen from the point of view of angular momentum transformation in the photon's reflection in Fig. 4.11. It has been shown that while reflecting from a conventional mirror, the incident 'right' photon with spin $S_z = +\hbar$ and momentum $p_z \approx \hbar|\mathbf{k}|$ moving in the positive direction of the z-axis is transformed into a 'left' photon having $p_z \approx -\hbar|\mathbf{k}|$, with same spin projection $S_z = +\hbar$ and vice-versa. This was explained on the basis of a mechanical effect on the mirror i.e. light pressure [26,96], whose major component is normal to the mirror surface as a result of which, the conventional mirror accepts momentum $\triangle p_z \approx 2\hbar\mathbf{k}$ as a single entity and does not change both the spin **S** and orbital momentum **L**. Whereas the situation changes drastically in case of reflection from the PCM, in this case, the conjugated photon with 'right' OAM remains 'right' and the photon with 'left' OAM remains 'left' due to the time reversal property of the phase conjugated mirror which makes the retro-reflected photon to pass all the states of the incident one in reverse sequence. Consequently, the accurate wavefront match of the incident and the reflected photon occurs which turned the OAM to 180° and changed the OAM projection $L_z = +\ell\hbar$ to the opposite one $L_z = -\ell\hbar$ without changing the sign of topological charge or winding

number (ℓ) in the propagation direction (Fig 4.11).

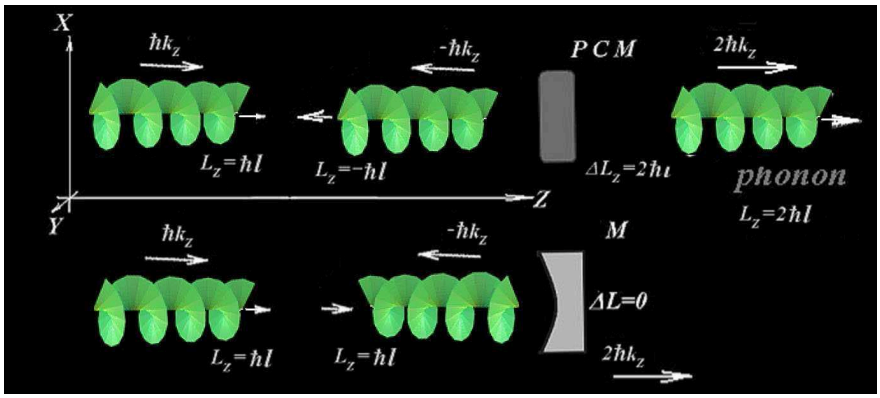

Figure 4.11: Comparison between a conventional mirror (M, bottom) and a wavefront reversal mirror (PCM, upper) from the point of view of angular momentum transformation in the photon's reflection [8].

In order to differentiate the reflection of the Gaussian and the first order LG beam from a conventional mirror, they considered the interference patterns produced by two counter-propagating fields i.e. incident (pump) E_p and reflected (stokes) E_s with equal amplitudes $E^o_{p,s}$ in case of both the Gaussian (Eq. 4.4) and the first order LG beam (Eq. 4.5). It is shown that for the Gaussian beam and the first order LG beam, the reflection through a conventional mirror results in the pancake like rotational ellipsoids structure and toroidal rings respectively.

$$\begin{aligned}
\mathbf{E}_{(p,s)}(r,\phi,z,t) &\approx E^o_{p,s}\exp\left[-i\omega_{(p,s)}t \pm ik_{(p,s)}z - \frac{r^2}{D^2(1\pm iz/(k_{(p,s)}D^2))}\right], \\
\mathbf{I}_{isosurface} &= |\mathbf{E}(r,\phi,z,t)|^2 = |\mathbf{E}_p(r,\phi,z,t)+\mathbf{E}_s(r,\phi,z,t)|^2 \\
&\cong 2|E^o_{p,s}|^2\left[1+\cos\left[(\omega_p-\omega_s)t-(k_p+k_s)z\right]\right]\exp\left[-\frac{2r^2}{D^2(1+z^2/(k_p^2D^4))}\right].
\end{aligned} \tag{4.4}$$

$$\begin{aligned}
\mathbf{E}_{(p,s)}(r,\phi,z,t) &\approx E^o_{p,s}r^\ell\exp[-i\omega_{(p,s)}t \pm ik_{(p,s)}z + i\ell\phi] - \left[\frac{r^2}{(D^2(1\pm iz/(k_{(p,s)}D^2)))}\right], \\
\mathbf{I}_{isosurface} &= |\mathbf{E}(r,\phi,z,t)|^2 = |\mathbf{E}_p(r,\phi,z,t)+\mathbf{E}_s(r,\phi,z,t)|^2 \\
&\cong 2|E^o_{p,s}|^2\left[1+\cos\left[(\omega_p-\omega_s)t-(k_p+k_s)z\right]\right]r^\ell\exp\left[-\frac{2r^2}{D^2(1+z^2/(k_p^2D^4))}\right].
\end{aligned} \tag{4.5}$$

where $\mathbf{E}_p$, $\mathbf{E}_s$ are incident (pump) and reflected (stokes) fields respectively, D is the diameter of the beam, ℓ is the topological charge or winding number, z is the distance passed along the z-axis, $r=|\mathbf{r}|$ is the length of the radius vector perpendicular to z-axis, ϕ is the azimuthal angle, ω_p, ω_s are the frequencies of the pump and stokes fields, E^o_s

and E_p^o are the maximal electric field amplitudes and k_p, k_s are propagation direction of pump and stokes fields respectively.

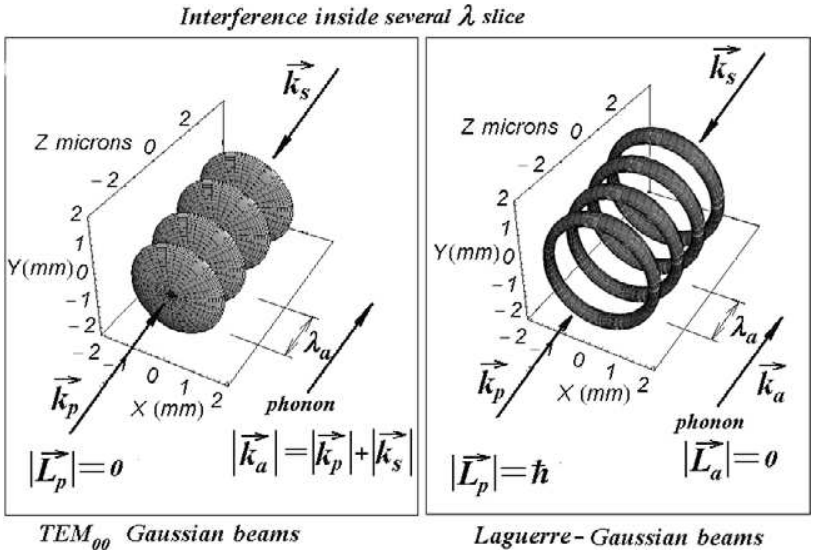

Figure 4.12: Interference pattern of the incident (pump) Gaussian mode wave E_p with field E_s reflected from a conventional mirror [8].

In the case of PCM, the interference pattern changes from a sequence of toroidal rings to a double helix for first order LG beam as shown in Fig. 4.13 and can be calculated on the basis of Eq. 4.6 which is given as

$$\begin{aligned}
\mathbf{E}_{(p,s)}(r,\phi,z,t) &\approx E^o_{p,s} r^\ell \exp[-i\omega_{(p,s)}t \pm ik_{(p,s)}z \pm i\ell\phi] - \left[\frac{r^2}{(D^2(1 \pm iz/(k_{(p,s)}D^2)))}\right] \\
\mathbf{I}_{isosurface} &= |\mathbf{E}(r,\phi,z,t)|^2 = |\mathbf{E}_p(r,\phi,z,t) + \mathbf{E}_s(r,\phi,z,t)|^2 \\
&\cong 2|E^o_{p,s}|^2 \left[1 + \cos\left[(\omega_p - \omega_s)t - (k_p + k_s)z + 2\ell\phi\right]\right] r^{2\ell} \exp\left[-\frac{2r^2}{D^2(1 + z^2/(k_p^2 D^4))}\right].
\end{aligned} \tag{4.6}$$

The spiral interference pattern (Fig. 4.13) has two maxima because the azimuthal dependence contains the doubled azimuthal angle ϕ and it rotates with angular velocity equal to the acoustical frequency $\Omega_a = (\omega_p - \omega_s)$. The angular velocity ($\Omega$) depends on the physical mechanism of the wavefront reversal and it could span from units of Hz for the photo-refractive crystals to the range of THz for Raman phase conjugators [7]. Denz et. al [9] have reported the method of degenerate four wave mixing (Section 4.3.1) in nonlinear media which produces a very stable and high fidelity interference pattern. They also showed the interference patterns for the higher order LG beams in case of conventional and PCM (Fig. 4.14) are comparable to the

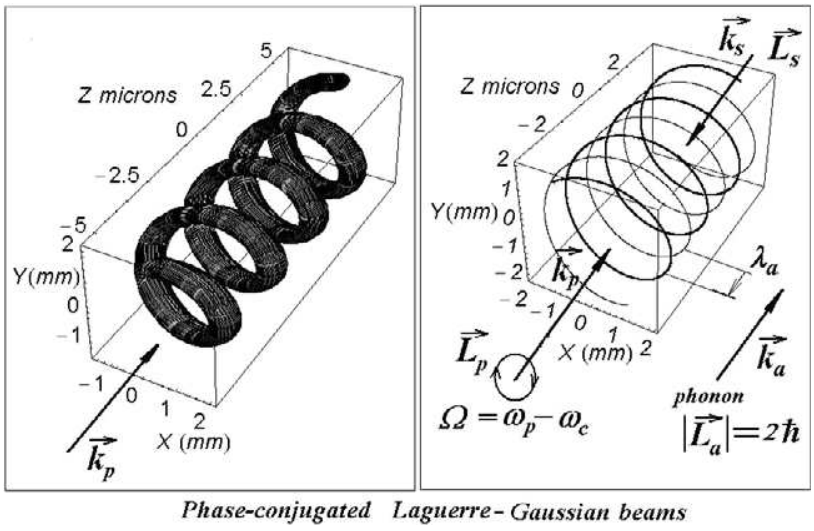

Figure 4.13: Interference pattern of the incident 'right'(pump) first order LG wave E_p and phase conjugated 'right' replica E_s for a topological charge $\ell = +1$ [8].

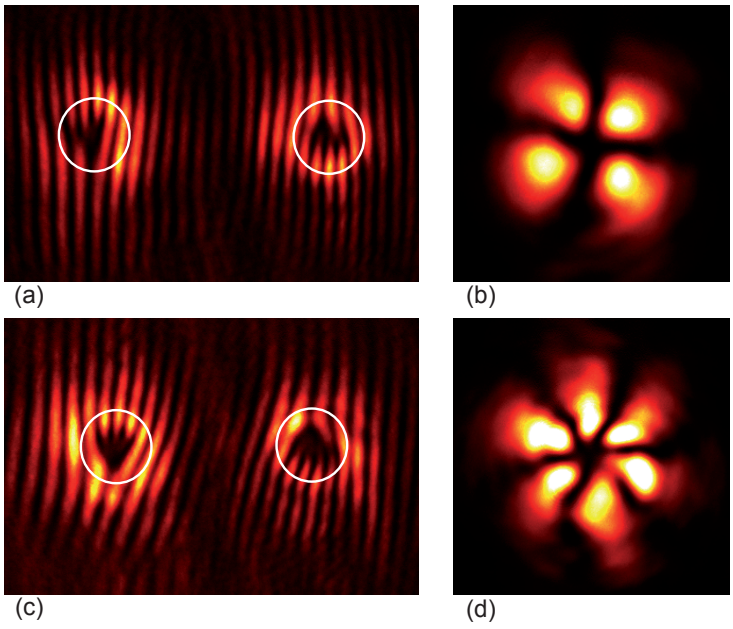

Figure 4.14: Interference pattern of $|m| = 2$ vortices (a,b) and $|m| = 3$ vortices (c,d). The left column shows a comparison between vortices reflected by a phase-conjugating (left) and a conventional mirror (right). At the right column, both vortices are interfering, yielding a $2|m|$ multi-pole interference pattern [9].

interference patterns shown in Fig. 4.12 and Fig. 4.13. Hence, proved the theoretical investigations [8] that during reflection from the PCM, the spin angular momentum (SAM) remains conserved and the orbital angular momentum (OAM) get reversed. Thus, the law of conservation of angular momentum requires the phase conjugating mirror (PCM) to accept the difference in the orbital angular momentum (OAM).

In contrast to the above mentioned works by Okulov and Denz et al., in the next section, we treat a multilayered structure (Fig. 4.15) to see the effect on the reflection and transmission of twisted light through it which is a special case of above described works [8, 9] where medium 1 and medium 2 (Fig. 4.15) are absent. We checked that our results are in good agreement in this case with the previous studies. The key idea behind the present work is that when the light is reflected from the interface between medium 1 and medium 2 (Fig. 4.15), it interferes with the field reflected at the interface at $z = 0$ and thus, the interference pattern carries information on the depth profile of refractive inhomogeneities. It is also shown that the structure containing several PCM interferences leads to a characteristic angular and radial pattern of the reflected beam. This pattern can in turn serve as an indicator for the phase conjugation of composite optical materials.

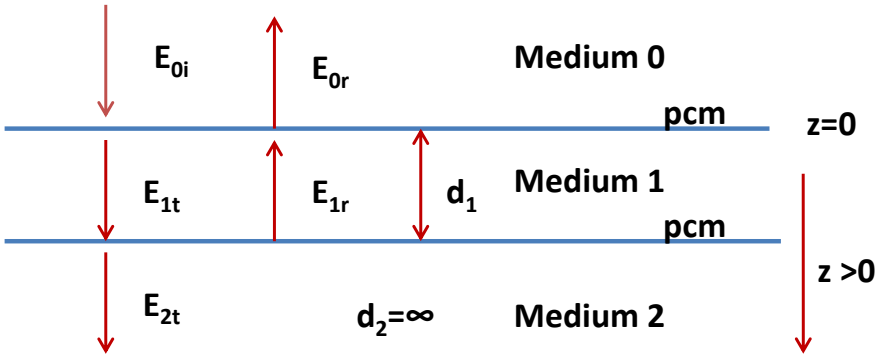

Figure 4.15: Schematic representation of the propagation of LG beam in a multi layer dielectric structure. The interfaces with PCM are indicated.

In our work, we have considered a trilayered dielectric structure (the layers and related quantities are indexed by 0, 1, 2) as sketched in Fig. 4.15. All the layers are parallel and infinitely extended. The monochromatic LG beam with the frequency ω propagates in the medium 0 and impinges onto the medium 1. The interface between medium 0 and medium 1 as well as the interface between medium 1 and medium 2 are phase conjugating and d_1 is the thickness of the layer 1 (our treatment is also valid when the whole medium 1 is phase conjugating). We denote the incident, the reflected and the transmitted fields by i, r and t respectively and n_0, $n_1$and n_2 are the refractive indices of the media 0, 1 and 2, respectively. We operate within the paraxial approximation, i.e. we assume that the transverse beam profile varies slowly along the direction of propagation. Beams with this property are collimated and have a well defined

direction of propagation. We restrict the consideration to the case of a large Rayleigh range, corresponding to a well collimated beam with a relatively little divergence. The electric field E (at the beam waist, $z = 0$) of the LG beam in cylindrical coordinates (with the z axis chosen to be along the incident beam propagation direction) is given by [24, 97].

$$E = \frac{C_p^{|\ell|}}{w_0}\left(\frac{\sqrt{2}r}{w_0}\right)^{|\ell|}\exp\left(\frac{-r^2}{w_0^2}\right)L_p^{|\ell|}\left(\frac{2r^2}{w_0^2}\right)\exp i(k_0 nz - \omega t)\exp(i\ell\phi), \tag{4.7}$$

where r and ϕ are the radial and azimuthal coordinates, ℓ can take any integer value either positive or negative and means physically the topological charge of the optical vortex. $L_p^{|\ell|}$ is the associated Laguerre polynomial, $C_p^{|\ell|}$ is a normalization constant, w_0 is the half beam width, and $k_0 = \omega/c$ is the wave number in vacuum.

The well known time reversal property of the phase conjugating mirror plays a key role in determining the behavior of the scattered beam's electric fields. As detailed in Refs. [8, 9], the orbital angular momentum changes sign upon a wavefront reversal at PCM, i.e. ℓ changes sign (this goes with excitations in the PCM material such that the total angular momentum balance is guaranteed [8, 9, 98, 99]). This ℓ property has to be imposed as an additional requirement on the beam when traversing the structure. To keep the notation simple we can incorporate this condition on ℓ by the ansatz

$$E_{0i} = \bar{E}_{0i}e^{i\ell\phi} = \frac{C_p^{|\ell|}}{w_0}\left(\frac{\sqrt{2}r}{w_0}\right)^{|\ell|}\exp\left(\frac{-r^2}{w_0^2}\right)L_p^{|\ell|}\left(\frac{2r^2}{w_0^2}\right)e^{i(k_0 n_0 z+\ell\phi)}, (z \le 0) \tag{4.8}$$

$$E_{0r} = \bar{E}_{0r}e^{-i\ell\phi} = r_0\frac{C_p^{|\ell|}}{w_0}\left(\frac{\sqrt{2}r}{w_0}\right)^{|\ell|}\exp\left(\frac{-r^2}{w_0^2}\right)L_p^{|\ell|}\left(\frac{2r^2}{w_0^2}\right)e^{-i(k_0 n_0 z+\ell\phi)}, (z \le 0) \tag{4.9}$$

$$E_{1t} = \bar{E}_{1t}e^{i\ell\phi} = t_1\frac{C_p^{|\ell|}}{w_0}\left(\frac{\sqrt{2}r}{w_0}\right)^{|\ell|}\exp\left(\frac{-r^2}{w_0^2}\right)L_p^{|\ell|}\left(\frac{2r^2}{w_0^2}\right)e^{i(k_0 n_1 z+\ell\phi)}, (0 \le z \le d_1) \tag{4.10}$$

$$E_{1r} = \bar{E}_{1r}e^{-i\ell\phi} = r_1\frac{C_p^{|\ell|}}{w_0}\left(\frac{\sqrt{2}r}{w_0}\right)^{|\ell|}\exp\left(\frac{-r^2}{w_0^2}\right)L_p^{|\ell|}\left(\frac{2r^2}{w_0^2}\right)e^{-i(k_0 n_1 z+\ell\phi)}, (0 \le z \le d_1) \tag{4.11}$$

$$E_{2t} = \bar{E}_{2t}e^{i\ell\phi} = t_2\frac{C_p^{|\ell|}}{w_0}\left(\frac{\sqrt{2}r}{w_0}\right)^{|\ell|}\exp\left(\frac{-r^2}{w_0^2}\right)L_p^{|\ell|}\left(\frac{2r^2}{w_0^2}\right)e^{i[k_0 n_2(z-d_1)+\ell\phi]}, (z \ge d_1). \tag{4.12}$$

Here, the temporal factor $\exp(-i\omega t)$ is omitted for the sake of simplicity. To evaluate the reflection and the transmission coefficients, we shall apply the condition of the continuity and smoothness of the field at the boundaries within the structure [100, 101] (note the behavior of ℓ upon scattering is already accounted for by the ansatz (Eq. 4.8-Eq. 4.12))

$$\left[\bar{E}_{0i} + \bar{E}_{0r}\right]_{z=0} = \left[\bar{E}_{1t} + \bar{E}_{1r}\right]_{z=0}, \tag{4.13a}$$

$$\left[\bar{E}_{1t} + \bar{E}_{1r}\right]_{z=d_1} = \left[\bar{E}_{2t}\right]_{z=d_1}. \tag{4.13b}$$

and

$$\left[\frac{\partial \bar{E}_{0i}}{\partial z}+\frac{\partial \bar{E}_{0r}}{\partial z}\right]_{z=0} = \left[\frac{\partial \bar{E}_{1t}}{\partial z}+\frac{\partial \bar{E}_{1r}}{\partial z}\right]_{z=0}, \tag{4.14a}$$

$$\left[\frac{\partial \bar{E}_{1t}}{\partial z}+\frac{\partial \bar{E}_{1r}}{\partial z}\right]_{z=d_1} = \left[\frac{\partial \bar{E}_{2t}}{\partial z}\right]_{z=d_1}. \tag{4.14b}$$

Eqs.(4.13) and (4.14) lead to

$$1+r_0 = t_1+r_1, \tag{4.15a}$$

$$t_1 e^{i\alpha_1}+r_1 e^{-i\alpha_1} = t_2, \tag{4.15b}$$

and

$$n_0[1-r_0] = n_1[t_1-r_1], \tag{4.16a}$$

$$n_1[t_1 e^{i\alpha_1}-r_1 e^{-i\alpha_1}] = n_2 t_2. \tag{4.16b}$$

With the notation

$$\alpha_1 = k_0 n_1 d_1.$$

On solving Eq. 4.15 and Eq. 4.16, we obtain the reflection coefficient r_0 related to the propagation in the medium 0, and the reflection and the transmission coefficients related to the propagation in the medium 1 and 2 denoted by r_1, t_1, r_2 and t_2, respectively. Explicitly, the reflection and the transmission coefficients are

$$r_0 = \left(\frac{n_0 A^- + n_1 A^+}{n_0 A^- - n_1 A^+}\right), \tag{4.17}$$

$$r_1 = \frac{1+r_0}{1-e^{-2i\alpha_1}N}, \tag{4.18}$$

$$t_1 = -r_1 e^{-2i\alpha_1}N, \tag{4.19}$$

$$t_2 = \frac{n_1}{n_2}[t_1 e^{i\alpha_1}-r_1 e^{-i\alpha_1}]. \tag{4.20}$$

where

$$A^+ = 1+e^{-2i\alpha_1}N,$$

$$A^- = 1-e^{-2i\alpha_1}N,$$

$$N = \left(\frac{n_2+n_1}{n_2-n_1}\right).$$

After substituting for the reflection and the transmission coefficients in the Eqs. (4.8-4.12), we can obtain the electromagnetic fields that describe the propagation of the LG beam through the system depicted in Fig. 4.15.

4.4.2 Results and discussion

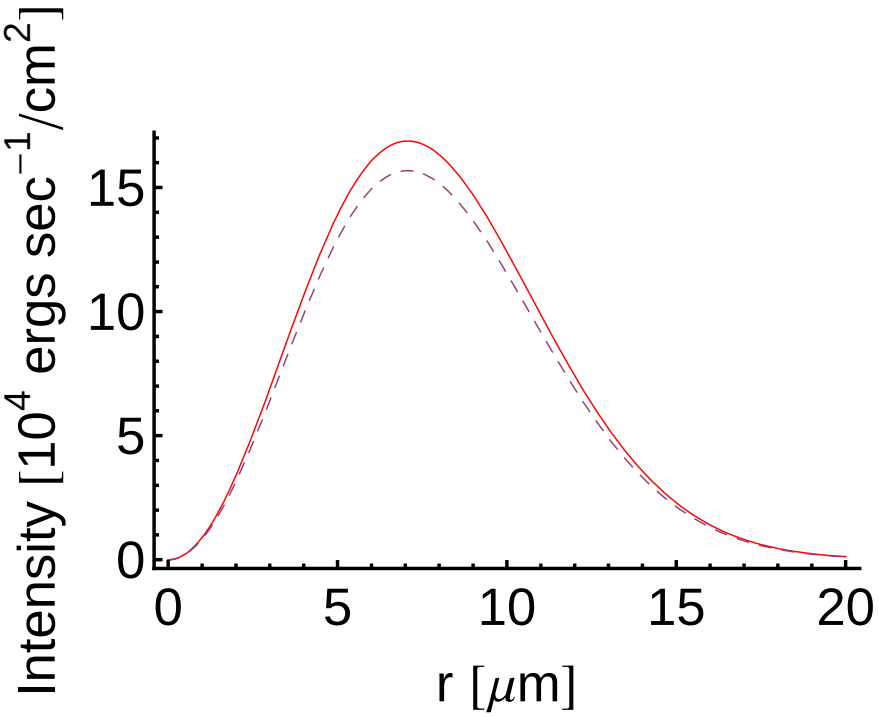

Figure 4.16: For the structure depicted in Fig. 4.15 we show the calculated total radial (r) intensity (in CGS system) of the LG laser beam for a conventional mirror (Red curve), and a PCM (Dashed curve) in the medium 0 for $\ell = 1$, $p = 0$. The material parameters and laser properties are chosen as: $\phi = 30°$, $n_0 = 1$(air), $n_1 = 1.77$ (Al_2O_3), $n_2 = 1.457$ (SiO_2), $d_1 = 20\ \mu$m, $w_0 = 1\ \mu$m, $\lambda = 632.9$ nm.

Experimentally, we imagine a situation where the reflected beam perpendicular to the structure (i.e. along the $-z$ axis) is detected. This case has been studied recently experimentally and theoretically for a single PCM in [8,9]. The results of these studies can be recovered from the above formula as a special case when only one PCM is present. The clear difference in the intensity of LG beam reflected from one PCM layer and multilayered structure can be seen in Fig. 4.16. In a multilayered structure interference effects are to be expected. The particular interest for us are those effects which are related to ℓ and the phase conjugating properties, say of the interface to medium 2. The idea is to infer from the detected reflected beam on the properties of the inhomogeneities (medium 1) in a bulk optical material.

To this end, we show in Fig. 4.17 the radial distribution of the total intensity of the reflected field (Eq. 4.9) from the structure in Fig. 4.15 for the LG beam with $\lambda =$ 632.9 nm. We consider a situation where the medium 0 is air ($n_0 = 1$), medium 1 is Al_2O_3 ($n_1 = 1.77$), and medium 2 is SiO_2 ($n_2 = 1.457$). The thickness of Al_2O_3 is $d_1 = 20\ \mu$m. A very thin PCM is deposited on Al_2O_3 and another thin PCM is deposited on SiO_2. Fig. 4.17 show that the reflected beam maintains the initial beam shape upon traversing the whole structure for different values of ℓ and p. As discussed in Refs.

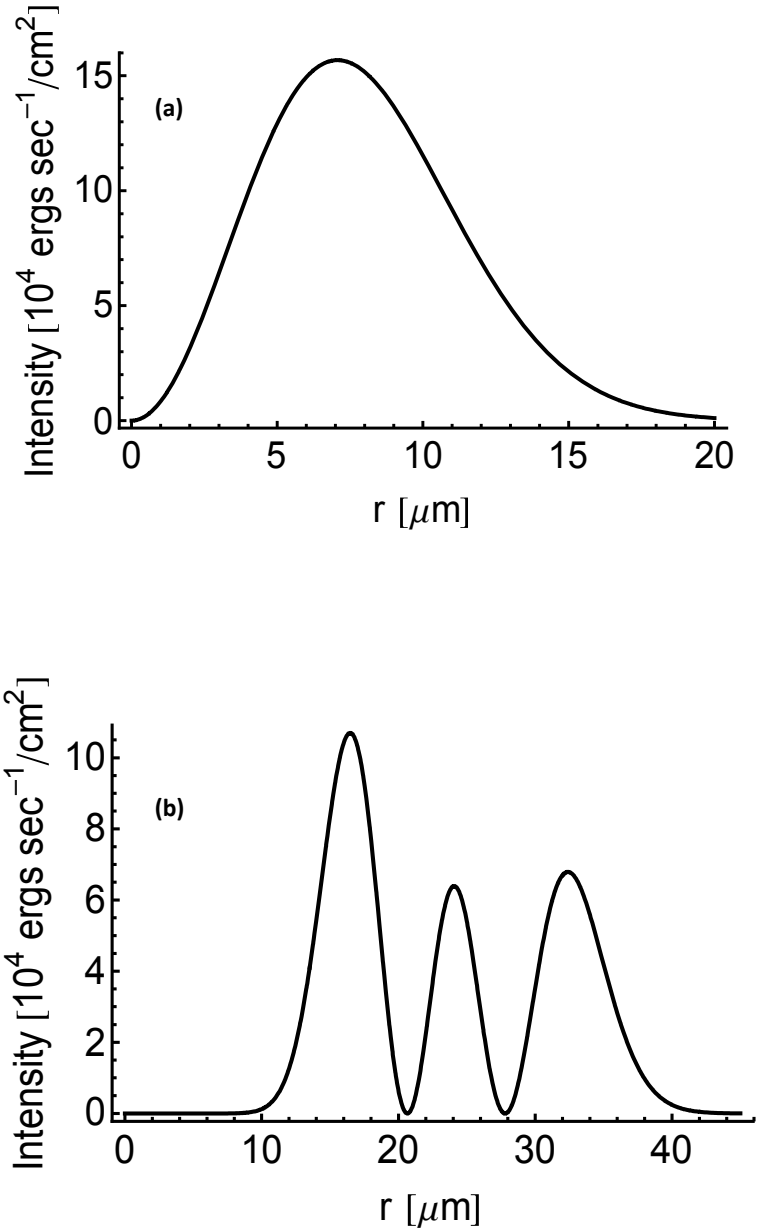

Figure 4.17: For the structure depicted in Fig. 4.15 we show the calculated total radial (r) intensity (in CGS system) of the LG laser beam in the medium 0 for $\ell = 1$, $p = 0$ (a), and for $\ell = 10$, $p = 2$ (b). The material parameters and laser properties are chosen as: $\phi = 30°$, $n_0 = 1$(air), $n_1 = 1.77$ (Al_2O_3), $n_2 = 1.457$ (SiO_2), $d_1 = 20\ \mu$m, $w_0 = 1\ \mu$m, $\lambda = 632.9$ nm.

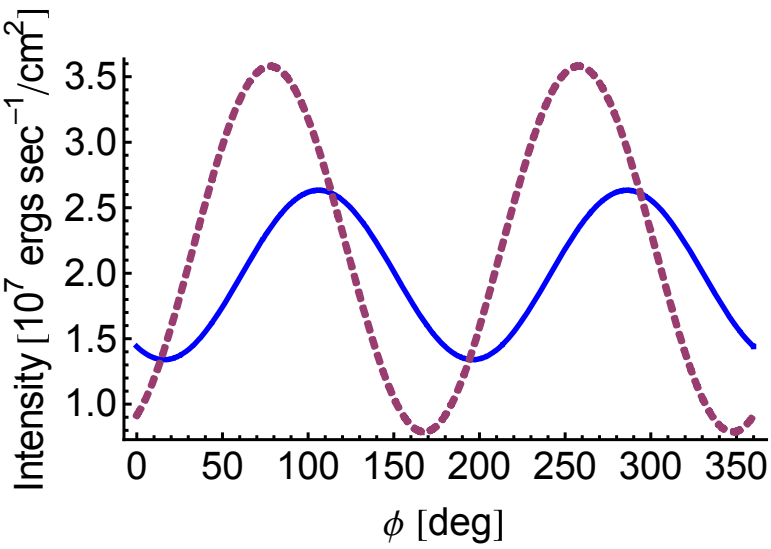

Figure 4.18: The same as in Fig 4.17 for $\ell = 1$, $p = 0$ but here we show the angular (ϕ) distribution of the LG beam intensity (in CGS system) for a different thickness d_1 of the medium 1. The blue solid curve is for $d_1 = 11\pi\lambda/2$ and the dashed curve is for $d_1 = 4\pi\lambda$. The radial distance r is fixed to be $w_0/2$.

[8,9], the angular distribution of the LG beam leads a special interference pattern upon reflection from one PCM. Qualitatively, we can thus expect a characteristic change of this pattern when the LG beam reflected from the interface to medium 2 contributes to the total reflected intensity. Obviously, this change depends on the thickness d_1 and varies on the scale of the wave length of the incoming LG beam. This behavior is confirmed by Fig. 4.18 from which we can conclude that the reflected LG carries depth information on phase conjugating inhomogeneity.

The similar interesting effects for the reflected LG light beams can also been seen after adding one additional layer to the structure shown in Fig. 4.15. A visible effect of an additional layer in the structure (Fig. A.1) on the total radial intensity distribution of the reflected LG beam (in medium 0) is shown in Fig. 4.19(a) for the conventional mirror and the PCM indicated by red curve and dashed curve respectively (for more details on the calculation for this case, refer Appendix A). The Fig. 4.19(b) depicts the increase in total radial intensity distribution in medium 0 for $\ell = 10$, $p = 5$. There is a drastic effect of the thickness of medium on the angular distribution of the LG beam which can be seen in Fig. 4.19(c) and Fig. 4.19(d) for $\ell = 1$, $p = 0$ and $\ell = 5$, $p = 2$ respectively. A similar kind of investigations in the case of localized wave like Bessel beams in the presence of an absorbing media have also been reported in [102, 103] where they predicted out the use of Bessel beams over plane waves, in the detection of buried objects, in particular, inside very dry material such as sandy or clayey ground.

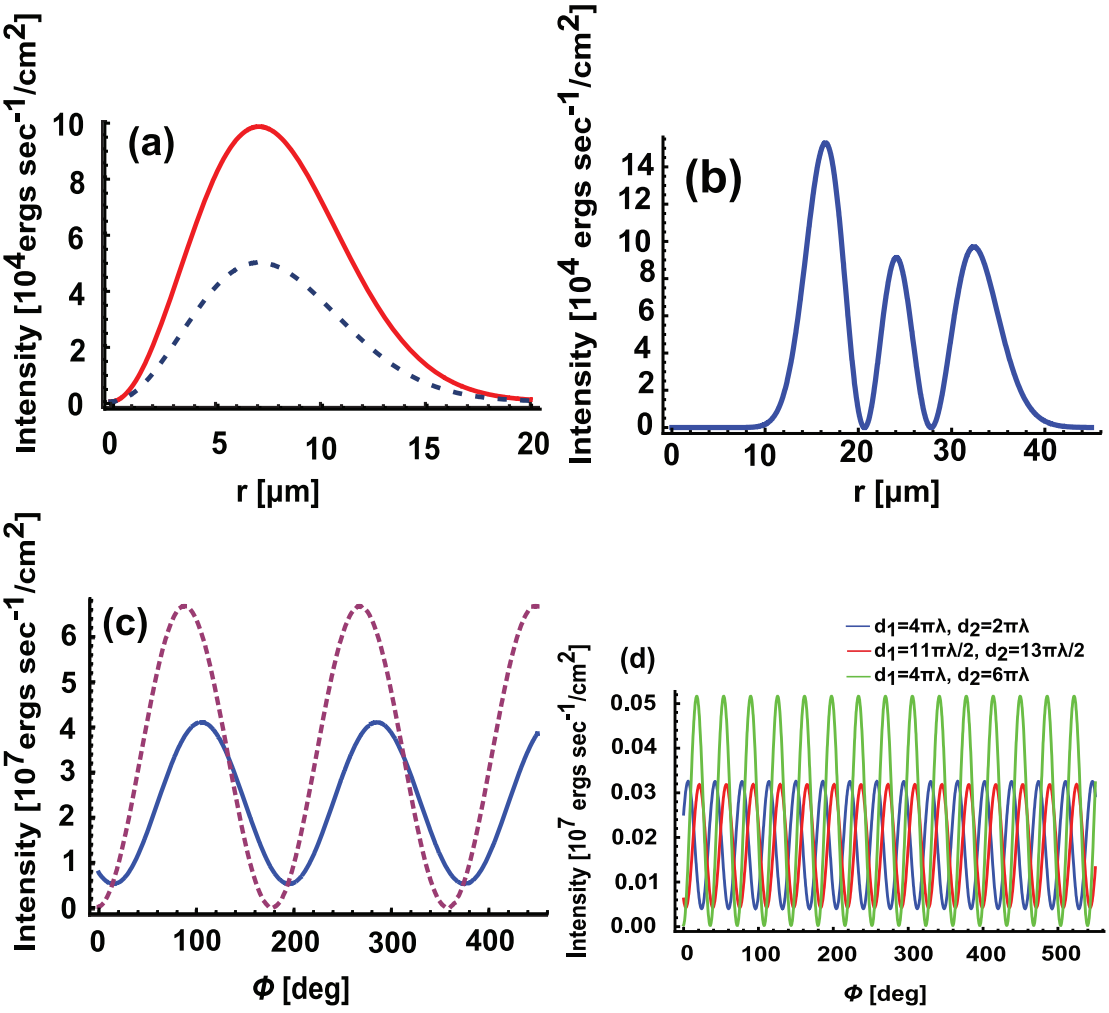

Figure 4.19: For the structure with additional one layer as depicted in Fig. 4.15 we show the calculated total radial (r) intensity (in CGS system) of the LG laser beam in the medium 0 (a) In case of $\ell = 1$, $p = 0$ for a conventional mirror (Red curve), and PCM (Dashed curve). (b) The total intensity of the LG beam in the medium 0 for $\ell = 10$, $p = 2$.The material parameters and laser properties are chosen as: $\phi = 30°$, $n_0 = 1$(air), $n_1 = 1.77$ (Al_2O_3), $n_2 = 1.457$ (SiO_2), $n_3 = 2.427$ ($BaTiO_3$),$d_1 = 20\ \mu$m, $d_1 = 30\ \mu$m w_0=1 μm, $\lambda = 632.9$ nm. (c) The angular (ϕ) distribution of the LG beam intensity for a different thicknesses d_1 and d_2 of the media 1 and 2 respectively. The blue solid curve corresponds for $d_1 = 11\pi\lambda/2$ and $d_2 = 13\pi\lambda/2$. The dashed curve is for $d_1 = 4\pi\lambda$ and $d_2 = 6\pi\lambda$. (d) The angular (ϕ) distribution of the LG beam intensity for a different thicknesses d_1 and d_2 of the media 1 and 2 respectively for $\ell = 5$, $p = 2$. The radial distance r is fixed to be $w_0/2$.

4.4.3 Conclusions

We have studied the propagation of the light beams carrying orbital angular momentum (OAM) in a dielectric multi layer structure with phase conjugating properties. Analytical expressions for the reflection and the transmission of the fields at individual layers are provided and we have demonstrated that the scattering of the OAM beams from phase conjugating refractive inhomogeneities leads to characteristic interferences that depend on the depth profile which can be tested, e.g. by varying the light wave length. Thus, this fact can be exploited to detect and characterize buried objects of non-metallic nature. Specially, the reflection properties of the beam with OAM from phase conjugating materials can be exploited in the identification of inhomogeneities of the bulk materials under ground by quantifying the amount of ℓ absorbed by the materials.

Chapter 5

Particle dynamics in twisted light

The optical manipulation of atoms and ions has been the subject of interest in many fields of physics. Especially the dynamics of charged particles have found a wide field of applications in particle accelerator [104], electron microscopes, magnetron, geophysics and in plasma physics [105]. In this chapter, we address the dynamics of a charged particle and neutral atoms with the help of twisted light. We have divided the present work into two main parts, the first part concerns with the trajectory of a charged particle in twisted light and the generation of magnetic field with the LG beams using the concept of Liénard-Wiechert potential [100]. Further, in the second part, we demonstrate the optical trapping, guiding and acceleration of neutral *He* atom in the strong LG beam based on the recent studies by Eichmann et al. [10]. As discussed in Ref. [10], the key point is the stabilization of the atom against ionization in a strong laser field [106] with a strength that exceeds by orders of magnitude (10^8) that employed for atom manipulation based on the photon momentum transfer [107–109]. The physical picture behind the drift atomic motion is as follows [10]: While the active electron oscillates in large orbits in the presence of the laser and the ionic core and is recaptured into bound states, it experiences a net drift force, stemming from the ponderomotive potential. The motion of the electron is partially converted into a center of mass-motion of the neutral atom due to electron-ion binding. In Section 5.3, we adopt this picture and study the effects brought about by the structured light.

5.1 Trajectory, acceleration and generation of magnetic field with twisted light

Here, we have demonstrated the confinement of a charged particle at the high intensity LG beam which results in the transversal trapping and longitudinal acceleration of a charged particle at the same time. In this regard by solving Lagrangian equations of motion, at first we have calculated the trajectory of a charged particle i.e. an electron (for complete derivation, refer Appendix A) followed by showing the acceleration and then the generation of magnetic field with twisted light.

The Lagrangian of a particle with charge ‘q’ moving with the velocity ‘$\mathbf{v}$’ in an

electromagnetic field with the scalar and vector potentials φ and $\mathbf{A}$ respectively can be written as [100]:-

$$L = \frac{1}{2}mv^2 - q\varphi + \frac{q}{c}\mathbf{A}\cdot\mathbf{v} \tag{5.1}$$

For $\varphi = 0$, $z = 0$, Eq. 5.1 reduces to

$$L = \frac{1}{2}mv^2 + \frac{q}{c}\mathbf{A}\cdot\mathbf{v} \tag{5.2}$$

$$L = \frac{1}{2}m(\dot{r}^2 + r^2\dot{\phi}^2) + \frac{q}{c}\mathbf{A}\cdot\mathbf{v} \qquad (\because x = r\cos\phi) \tag{5.3}$$

$$\tag{5.4}$$

While the product term $\mathbf{A}\cdot\mathbf{v}$ can be written as

$$\mathbf{A}\cdot\mathbf{v} = -r(t)\sin\phi(t)\dot{\phi}(t)f_{\ell p} + \dot{r}(t)\cos\phi(t)f_{\ell p} \tag{5.5}$$

where the $f_{\ell p}$, the field amplitude of LG beam is ([97] or chapter2)

$$f^{LG}_{\ell p}(r,\phi,z=0,t) = \frac{C_p^{|\ell|}}{w_0}E_0\left(\frac{\sqrt{2}r(t)}{w_0}\right)^{|\ell|}\exp\left(\frac{-r(t)^2}{w_0^2}\right)L_p^{|\ell|}\left(\frac{2r(t)^2}{w_0^2}\right)\exp(i\ell\phi(t))\exp i(\phi_0+\omega t) \tag{5.6}$$

where r, ϕ and z are cylindrical coordinates, ℓ is the azimuthal index, p is the radial mode index, w_0 is the beam waist at $z = 0$, $L_p^{|\ell|}\left(\frac{2r^2}{w(z)^2}\right)$ is the associated Laguerre Polynomial, ϕ_0 is the initial phase of the field and C_p^{ℓ} is the normalization constant.

The Euler-Lagrange equations of motion in cylindrical coordinates are

$$\frac{d}{dt}\left(\frac{\partial L}{\partial \dot{r}}\right) = \frac{\partial L}{\partial r}, \tag{5.7}$$

$$\frac{d}{dt}\left(\frac{\partial L}{\partial \dot{\phi}}\right) = \frac{\partial L}{\partial \phi}, \tag{5.8}$$

$$\frac{d}{dt}\left(\frac{\partial L}{\partial \dot{z}}\right) = \frac{\partial L}{\partial z}. \tag{5.9}$$

On solving the Eqs. 5.7-5.9 for LG_0^1 mode with $z = 0$, we have the classical non-relativistic equations of motion for an electron in cylindrical coordinates as

$$\ddot{r}(t) = r(t)\dot{\phi}(t)^2 - \frac{q}{mc}E_0\left(\frac{\sqrt{2}}{w_0}\right)^{\lambda} exp\left(\frac{-r(t)^2}{w_0^2}\right)\Big(r(t)\dot{\phi}(t)\sin\phi(t)\Theta_1 A + [r(t)]^{\lambda}\cos\phi(t)B\Big), \tag{5.10}$$

and

$$\begin{aligned} r(t)^2\ddot{\phi}(t) = &-2mr(t)\dot{r}(t)\dot{\phi}(t) + \frac{q}{mc}E_0\left(\frac{\sqrt{2}r(t)}{w_0}\right)^{\lambda}\exp\left(\frac{-r(t)^2}{w_0^2}\right)\Theta_2 \\ &\times\Big(\lambda\dot{r}(t)\cos\phi(t) - \lambda r(t)\dot{\phi}(t)\sin\phi(t) + r(t)\sin\phi(t)(\omega + \lambda\phi'(t))\Big) \\ &+ \frac{q}{mc}E_0 r(t)\sin\phi(t)\left(\frac{\sqrt{2}}{w_0}\right)^{\lambda}\exp\left(\frac{-r(t)^2}{w_0^2}\right)r'(t)\Theta_1 A \end{aligned} \tag{5.11}$$

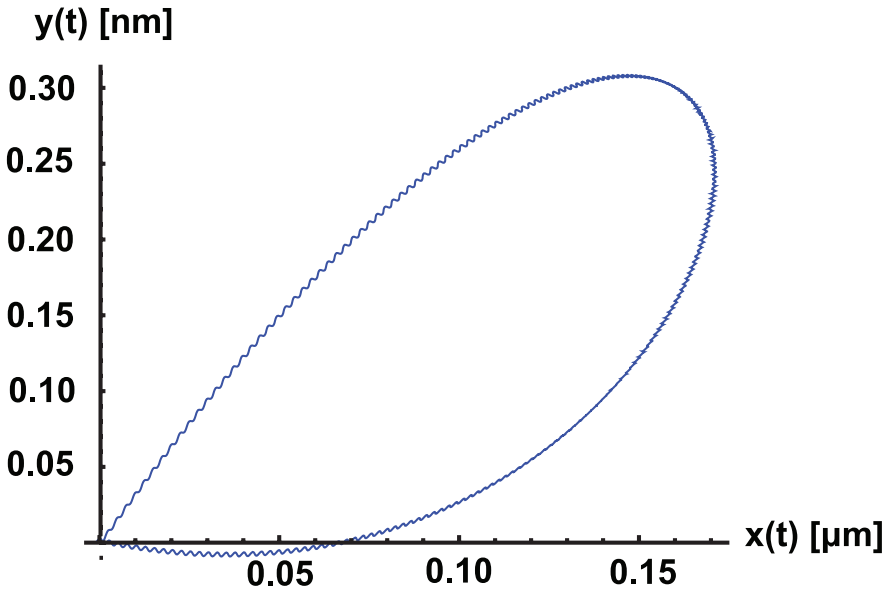

Figure 5.1: Trajectory of an electron in the LG beam with following parameters: $m_e = 9.1 \times 10^{-31}$kg, $w_0 = 1.05\,\mu$m, $\omega = 25.2 \times 10^{14}$ rad/s, $\phi_0 = 98.5°$, $E_0 = 0.6 \times 10^9$ V/m, $\ell = 1$, $p = 0$, $\mathbf{r}(t=0) = (0.5\text{ nm}, 0, 0)$, $\dot{\mathbf{r}}(t=0) = (10^6\text{ m/s}, 0, 0)$.

where $A = \left([r(t)]^{\lambda}\left(\frac{-2r(t)}{w_0^2}\right) + \lambda[r(t)]^{\lambda-1}\right)$, $B = \cos(\omega t + \phi_0 + \lambda\phi(t))(\omega + \lambda\phi'(t))$, $\Theta_1 = \sin(\omega t + \phi_0 + \lambda\phi(t))$ and $\Theta_2 = \cos(\omega t + \phi_0 + \lambda\phi(t))$.

The trajectory (Fig. 5.1) and the acceleration of the charged particle (Fig. 5.2) has been drawn on the basis of Eqs. 5.10 and 5.11.

By using the Liénard-Wiechert potential, the expressions for the electric and the magnetic field for the accelerated charged particle can be given with the help of Eq. 5.12 and 5.13 [100] respectively. Thus, the generated magnetic field with TL can be shown as in Fig. 5.3.

$$\mathbf{E} = \frac{q}{4\pi\varepsilon_0}\frac{1}{\kappa^3\mathbf{R}^2}(\mathbf{n}-\beta)(1-\beta^2) + \frac{1}{c\kappa^3\mathbf{R}}\mathbf{n}\times\left[(\mathbf{n}-\beta)\times\dot{\beta}\right], \tag{5.12}$$

$$\mathbf{B} = \nabla\times\mathbf{A} = \frac{1}{c}\mathbf{n}\times\mathbf{E} \tag{5.13}$$

where $\beta = \mathbf{v}/c$ & $\mathbf{n} = \frac{\mathbf{R}}{|R|}$.

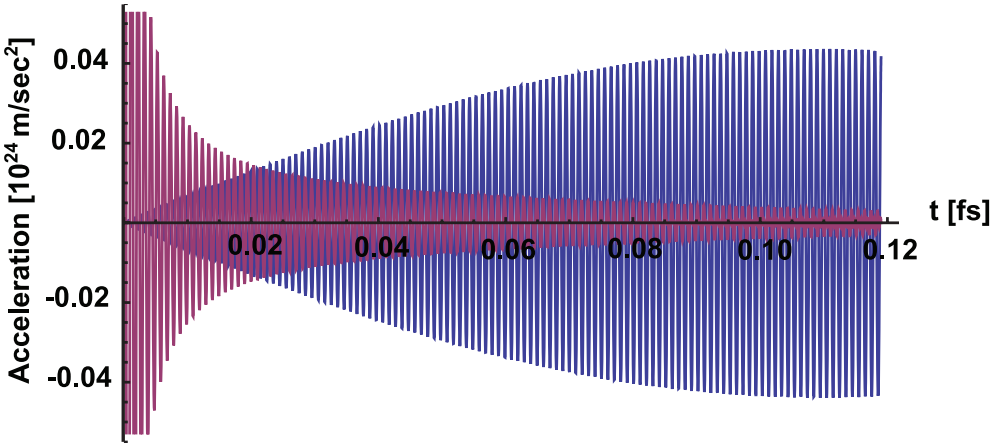

Figure 5.2: Acceleration of a charged particle in twisted light for the same parameters as in Fig. 5.1. The red and blue curve show the acceleration in ϕ and r direction respectively.

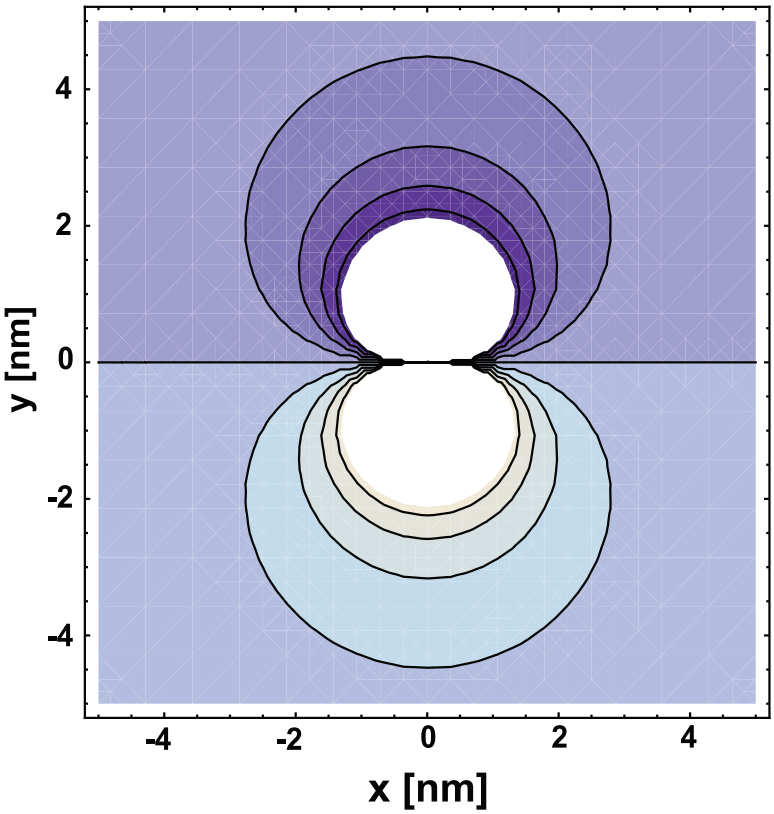

Figure 5.3: The magnetic field due to the LG beam for the same paramaters as in Fig. 5.1.

5.2 Dynamics of atoms and molecules in intense laser fields

It is a well known that a short laser light focused on a small region may have an electric field strength comparable to the Coulomb electric field acting upon the bound electrons in the atom. Thus, the relationship between the laser intensity 'I' and the generated electric field strength **E** can be given as:

$$I = \frac{1}{2}\varepsilon_0 c\mathbf{E}^2 \tag{5.14}$$

where ε_0 is the vacuum electrical permittivity and c is the speed of light in vacuum. For, e.g. hydrogen, the electric field acting on the electron in the ground state is $\mathbf{E} \simeq 5 \times 10^9$ V/cm which corresponds to an intensity $I \simeq 3.5 \times 10^{16}$ W/cm^2.

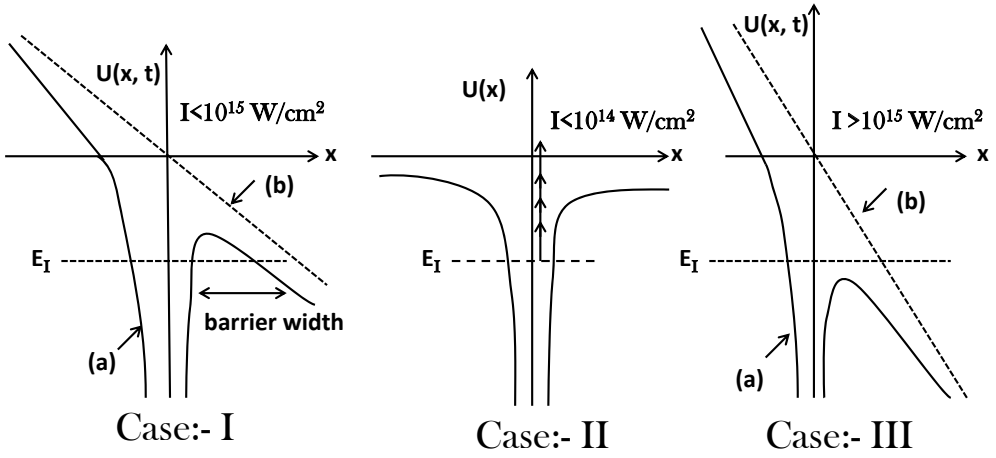

Figure 5.4: Case I: Tunneling ionization regime. Curve (a) shows the total potential energy U (x,t) of an atom in an intense laser field, the curve (b) represents the laser-electron interaction energy. Here, it shows that the laser field distorts the Coulomb potential. Case II: Multi-photon ionization regime. The figure shows the potential energy U (x) of an atom in presence of a weak external laser field. In this regime ($I < 10^{14}$ W/cm^2), the laser is not able to modify the Coulomb potential. Here, the arrows indicates that the ionization occurs through multi-photon absorption. Case III: OTBI regime. The curve (a) shows the potential energy U (x,t) of an atom in the presence of a strong external laser field, (b) represents the electron-laser interaction energy. In this regime ($I > 10^{15}$ W/cm^2), the ground state energy lies above the potential barrier. Here, in all the three cases, E_I and I are the ionization energy and the intensity of the field respectively.

Depending upon the laser intensity, the variety of new phenomena have been observed and among these the most important are :

- Multi-photon ionization (MPI)
- Above threshold ionization (ATI)

- High harmonic generation (HHG)

The above mentioned ionization regimes can be discriminated on the basis of Keldysh parameter (γ) which is defined by the ratio between the tunneling time (T_{tun}) i.e, the time required to cross the potential barrier, and the laser period (T_L) i.e.

$$\gamma = \frac{T_{tun}}{T_L} = \sqrt{\frac{E_I}{2U_p}} \tag{5.15}$$

where E_I is the ionization energy of the atom and U_p is the ponderomotive energy.

- If $\gamma < 1$, the intense laser field (10^{14}-10^{15} W/cm^2) make the width of potential barrier small, as a result, the tunneling time (T_{tun}) becomes short as compared to the laser period (T_L) (Fig. 5.4);
- If $\gamma > 1$, the intensity of the laser field is usually less than 10^{14} W/cm^2 and the tunneling time is too long compared to the laser period which makes the probability of the electron tunneling during a laser cycle very small which results in MPI (Fig. 5.4);
- If $\gamma \ll 1$, the laser field intensity is so strong ($> 10^{15}$ W/cm^2), it shifts the ground state energy of the atom above the distorted potential barrier created by the intense laser field. Consequently, the ionization takes place in a very short time compared to the laser period, so that the atom can be considered fully ionized at the beginning of the laser cycle only, thus it is called the over the barrier ionization (OTBI) (Fig. 5.4).

5.2.1 Multi-photon ionization (MPI)

Multi-photon ionization (MPI) is the process of ionization of an atom by means of absorption of the number of photons just necessary to overcome the ionization energy E_I (Fig. 5.5). The energy of the emitted electron E_e, is given by the relation:

$$E_e = N\hbar\omega - E_I < \hbar\omega \tag{5.16}$$

where N is the number of photons absorbed, ω is the photon frequency and the probability of ionization for N photons, P_N is given as [110, 111]

$$P_N \propto I^N \tag{5.17}$$

where I is the intensity of the driven laser field.

5.2.2 Above threshold ionization (ATI)

In 1980, Gontier and Trahin [112] observed the process of ionization which occurs through the absorption of the number of photons larger than the minimum necessary to overcome the ionization energy and this phenomenon was named as above threshold

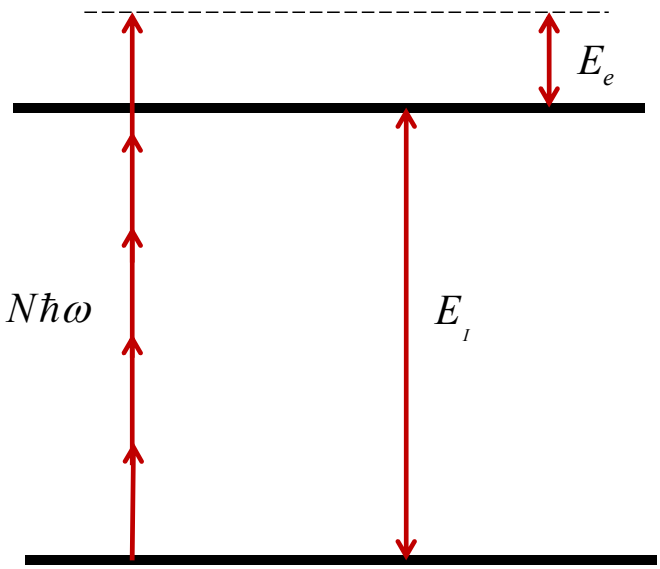

Figure 5.5: Process of Multi-photon ionization (MPI): E_I is the ionization energy of the atom, E_e is the kinetic energy of the emitted electron and N, the number of photons at frequency(ω) absorbed.

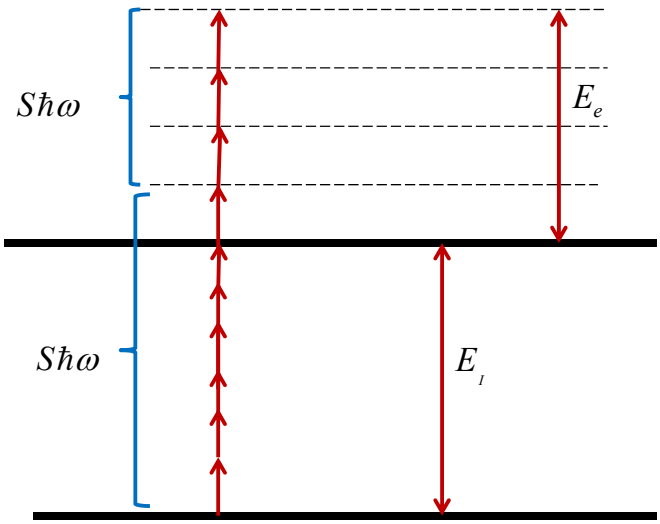

Figure 5.6: A typical ATI process with the absorption of $(N + S)$ photons. S, the number of photons absorbed above the minimum number needed to overcome the ionization barrier. E_e, E_I are the electron energy emitted and the ionization energy respectively.

ionization (ATI) (Fig. 5.6).
In ATI, the energy of the emitted electron and ionization probability are given by following relations respectively:-

$$E_e = (N + S)\hbar\omega - E_I \tag{5.18}$$

and

$$P_N \propto I^{N+S} \tag{5.19}$$

where I is the intensity of the laser field and S is the number of photons absorbed in excess.

5.2.3 High harmonic generation (HHG)

It is a nonlinear optical process in which the original laser light's frequency is converted into its integer multiples i.e. $N\hbar\omega$. The maximum photon energy (E_{max}) producible with the high harmonic generation is given by the cut-off law of harmonic plateau [113].

$$E_{max} = I_p + 3.17U_p, \tag{5.20}$$

where I_p is the ionization potential of the target atom and $U_p = \frac{E_0^2}{4\omega^2}$ is the ponderomotive energy with E_0 and ω being electric field strength and frequency respectively. Many features of the high harmonic generation (HHG) can be intuitively and qualitatively explained on the basis of the semiclassical **'three step model'** (Fig. 5.7), also referred as the semi-classical model of the high harmonic generation. HHG requires that the laser light needs to be linearly polarized. Otherwise the electron would not be accelerated back towards the atom with a significant probability. In this model, the atom is approximated to have only one electron. The motion of this electron in the laser field is treated classically while the active tunneling and recombination processes are treated quantum mechanically which are well explained in the following steps:-

Three step model [114]

- First Step:- Tunneling ionization.
  The presence of the intense laser field results in the distortion of the potential energy of the system and thus, the potential barrier gets lowered. Consequently, the electron tunnels in the continuum overcoming the potential barrier due to the Coulomb and the laser field.

- Second Step:- Propagation in the laser field.
  The electron is treated classically and consists of free oscillations driven by the laser field. During this propagation, the electron gains kinetic energy and accelerates away from the atom by electric field.

- Third Step:- Recombination.
  If the electron is near the nucleus, there is certain probability that it can recombine back to the atom emitting a photon with energy equal to the kinetic energy gained in the second step plus the ionization energy (Eq. 5.20).

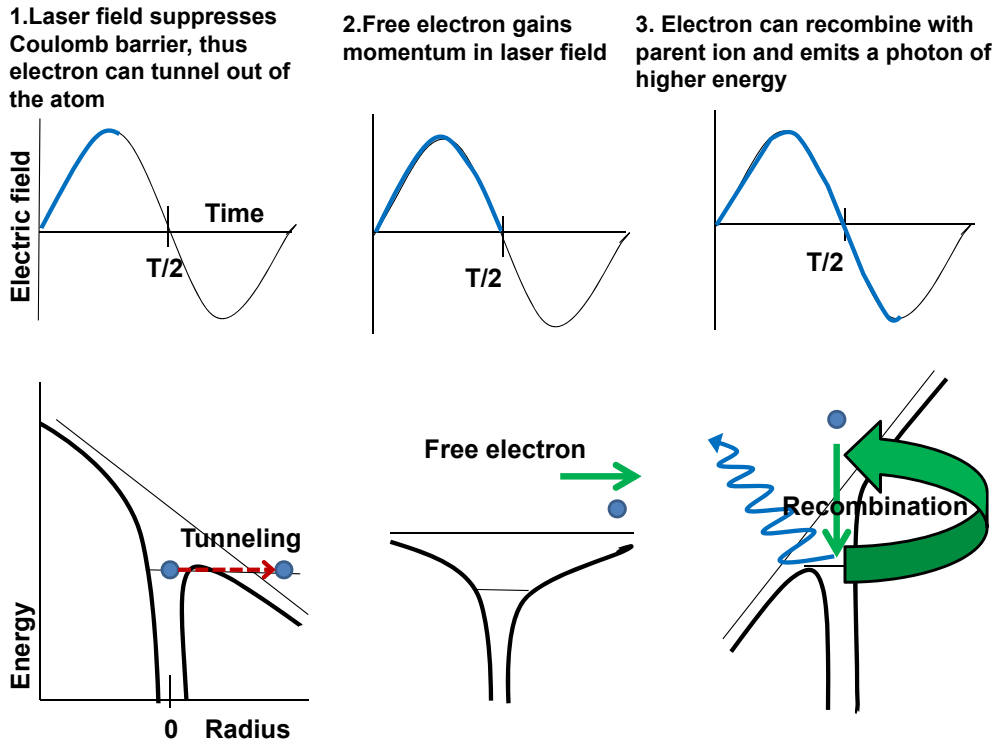

Figure 5.7: Process of three step model.

5.3 Introduction to Optical trapping (OT)

Trapping and controlling charged particles by a time-dependent, non-uniform electromagnetic field was triggered by the work of Boot et. al. [115] in 1957. The underlying mechanism can be understood classically as the second order effect that depends on the spatial gradient of the field intensity and tends to push the particles from regions of high to low intensities. This fact can be utilized for the confinement of charged particles [116] and plasmas [117]. In 1966, Phillips and Sanderson [118] proposed that the electrons could be trapped in a laser focus with a minimum intensity on axis. Since then a wealth of phenomena associated with the ponderomotive force and its corresponding potential named as ponderomotive potential have been revealed [6, 119–127] which found applications in diverse areas, ranging from accelerator physics and optical manipulation to plasma physics and biology. The ponderomotive potential is a result of the variation of a charged particle's average kinetic energy in a spatially varying electromagnetic field. The potential is highest in the regions of greatest intensity and lowest in the region of least intensity. This generates a force that will tend to push the particle away from the regions of high intensity. Its expression is given as [127] :-

$$\mathbf{F_p} = -\frac{e^2}{2m\omega^2}\nabla\langle E^2\rangle, \tag{5.21}$$

where e and m are the particle's charge and mass respectively, while w and E are the frequency and amplitude of the electric field.

For a focused laser pulse, due to the diffraction effect, F_p in acceleration stage can be larger than that in de-acceleration stage, therefore the electron may obtain a larger energy near the focus and lose the energy at the de-acceleration stage. This is the basic idea of the ponderomotive force electron acceleration using an intense focused pulse laser. In non-relativistic case, the ponderomotive potential is given as:

$$\Phi_p = \frac{e^2}{2m\omega^2}\langle E^2\rangle. \tag{5.22}$$

For the LG beam, the normalized time averaged intensity is given as:

$$\begin{aligned} E(r,\phi,z=0,t) &= E_0\frac{C_p^{|\ell|}}{w_0}\left(\frac{\sqrt{2}r}{w_0}\right)^{|\ell|}\exp\left(\frac{-r^2}{w_0^2}\right)L_p^{|\ell|}\left(\frac{2r^2}{w_0^2}\right)\cos(\ell\phi+\omega t)+c.c,\\ E(r,\phi,z=0,t) &= 2E_0\frac{C_p^{|\ell|}}{w_0}\left(\frac{\sqrt{2}r}{w_0}\right)^{|\ell|}\exp\left(\frac{-r^2}{w_0^2}\right)L_p^{|\ell|}\left(\frac{2r^2}{w_0^2}\right)\cos(\ell\phi+\omega t),\\ \langle E^2\rangle &= 4E_0^2\frac{C_p^{|\ell|}}{w_0}\left(\frac{\sqrt{2}r}{w_0}\right)^{2|\ell|}\exp\left(\frac{-2r^2}{w_0^2}\right)\left(L_p^{|\ell|}(\frac{2r^2}{w_0^2}\right)^2\langle\cos^2(\ell\phi+\omega t)\rangle. \end{aligned}$$

where the oscillation average of trigonometric function is equal to $\frac{1}{2}$

$$\langle E^2\rangle = 2E_0^2\frac{C_p^{|\ell|}}{w_0}\left(\frac{\sqrt{2}r}{w_0}\right)^{2|\ell|}\exp\left(\frac{-2r^2}{w_0^2}\right)\left(L_p^{|\ell|}\left(\frac{2r^2}{w_0^2}\right)\right)^2,$$

Therefore,

$$\Phi_p = \frac{e^2}{m\omega^2}E_0^2\frac{C_p^{|\ell|}}{w_0}\left(\frac{\sqrt{2}r}{w_0}\right)^{2|\ell|}\exp\left(\frac{-2r^2}{w_0^2}\right)\left(L_p^{|\ell|}\left(\frac{2r^2}{w_0^2}\right)\right)^2. \tag{5.23}$$

This intensity distribution has the added advantage that the ponderomotive potential will be approximately parabolic near the intensity minimum. Its parabolic shape results in the two-dimensional simple harmonic motion transverse to the beam direction.

For the LG_0^1 mode, the ponderomotive potential will reduce to

$$\Phi_p = \frac{e^2}{m\omega^2}E_0^2C_0^1\left(\frac{\sqrt{2}r}{w_0}\right)^2\exp\left(\frac{-2r^2}{w_0^2}\right). \tag{5.24}$$

Now, we will show the results on the trapping of a neutral He atom in the ponderomotive potential given by Eq. 5.24, but before that we will explain the principle of optical trapping and the role of twisted light in OT.

5.3.1 Principle of optical trapping (OT)

A light beam can exert a force on an object and this very small force of the order of piconewtons can be used to manipulate small objects such as micro-spheres. A very large scaled example of this phenomenon is that of a comet whose dust particles are

optically pushed by radiation pressure from the Sun's light. Similar idea shed the light to use the laser light to manipulate objects which was first realized by Arthur Ashkin also known as "Father of Optical Trapping" in 1970 at Bell Labs. It was Ashkin's idea which formed the basis for Steven Chu's work on cooling and trapping atom, which earned him the 1997 Noble prize in physics along with scientists Claude Cohen-Tannoudji and William Phillips. Since, then the field of optical trapping or optical tweezers (OT) has grown tremendously and has emerged as a powerful tool with the broad reaching applications within both biological and non-biological fields. Below, some of the milestones in the field of OT are reported:

- 1970: Arthur Ashkin (Bell Laboratories) demonstrates the effect of radiation pressure on latex spheres in water [32].
- 1978: Two opposing laser beams were used to trap and cool atoms [128].
- 1986: Development of a single beam gradient force optical trap [129].
- 1987: First application to biological samples [130, 131].

Soon, it was realized that the gradient force alone would be sufficient to trap small particles and the use of a single tightly focused laser beam with an objective lens of high numerical aperture (NA) can trap a transparent particle in three dimension and such an arrangement called as optical tweezers (OT) (Fig. 5.8). The Fig. 5.8 shows the single beam optical gradient force trap [132] which use a strongly focused beam of light to trap small objects like dielectric particles.

Photons can consider as particles in motion, which transfer part of their momentum to the particle when they are scattered and hence exerts force on the particle called as **radiation pressure**. He (Arthur Ashkin) investigated how the radiation pressure could be used to influence microscopic objects. The radiation pressure can be divided into two components: the scattering force (which points in the direction of the propagation of incident laser light) and the gradient force (which points in the direction of the intensity gradient of the light). On scattering, the photons transfer part of their momentum to the particle (for example a latex micro-sphere) (Fig. 5.9(1)). As a result of it, the scattering force pushes away the particle along the beam propagation direction. Some photons are not reflected and cross the interface. Their path is changed and some momentum is transferred to the particle as well, which is attracted toward the region of greater light intensity. This is the gradient force component of radiation pressure (Fig. 5.9(2)). A TEM_{00} focused laser beam has a Gaussian intensity profile, with the region of more intense light is toward the propagation axis. If the beam is strongly focused by a microscope objective, the brightest region is in the focal plane. Thus, the gradient force pulls the micro-sphere toward the laser focus (Fig. 5.9(3)). For micrometer sized dielectric particles, like latex or silica micro-spheres, the gradient force is always greater than the scattering force, so that they are trapped in the region near the focus. For small displacement from the laser focus, particles can be considered as trapped in a harmonic potential. The condition of stable three-dimensional optical trap is that the ratio of the gradient force to the scattering force must be greater than 1.

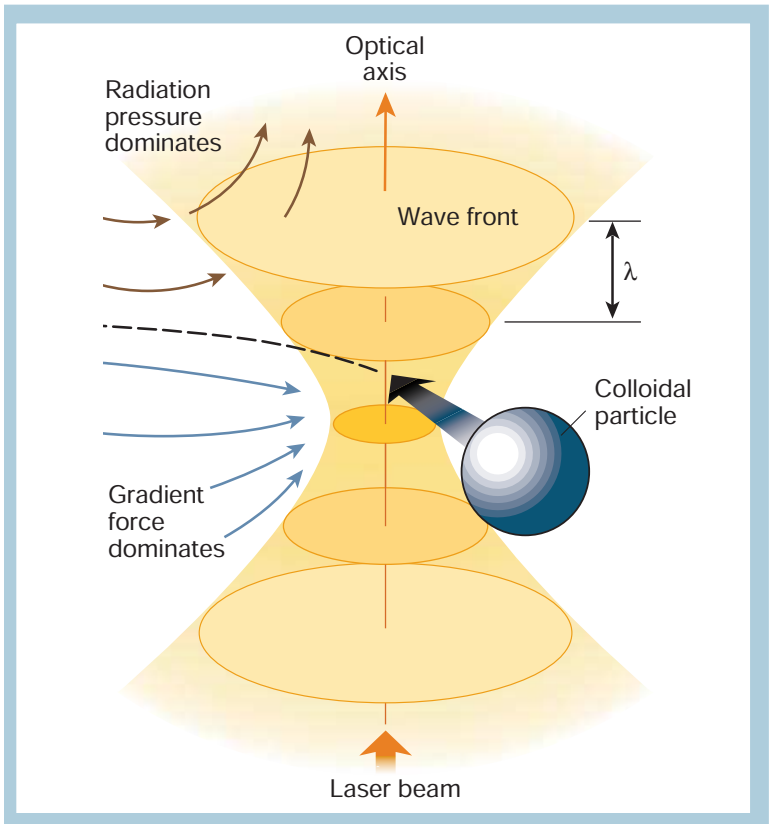

Figure 5.8: Single beam optical gradient force trap for a colloidal particle. Intensity gradients in the converging beam draw small objects, such as a colloidal particle, toward the focus, whereas the radiation pressure of the beam tends to blow them down the optical axis. Under conditions where the gradient force dominates, a particle can be trapped, in three dimensions, near the focal point [133].

Optical tweezers (OT) are able to trap particles like dielectric particles (polystyrene, silica), metallic (gold, silver,copper), biological (cells, macro-molecules, intracellular structures) within the size of 20 nm-20 μm which have provided us the access to physical, chemical and biological processes in the mesoscopic domain. The majority of OT make use of the conventional Gaussian beams. However a number of other beam types have been used to trap particles, including high order laser beams i.e. Hermite-Gaussian beam, Laguerre-Gaussian beams and Bessel beams. But, here in this chapter, we make use of the LG beams to trap particles (Section 5.4). Basically, the optical manipulation can be divided into three regimes as shown in Fig. 5.10:-

- Case (a) Mie regime where the radius of the trapped object or sphere is much larger than the wavelength of the laser light i.e. $a \gg \lambda$.
- Case (b) Lorentz-Mie regime where the radius of the trapped object is approximately the same as the wavelength of the laser light i.e. $a \sim \lambda$.
- Case (c) Rayleigh regime where the radius of the trapped object or sphere is much smaller than the wavelength of the laser light i.e. $a \ll \lambda$.

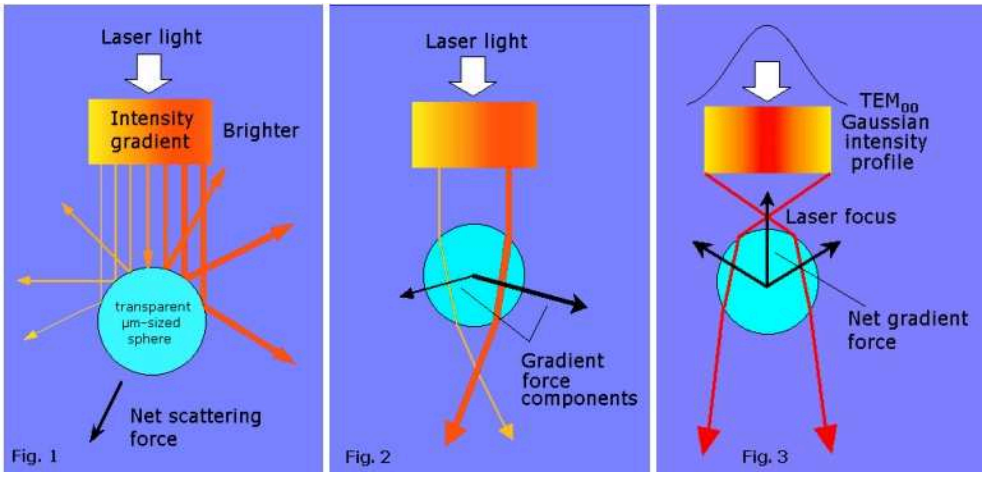

Figure 5.9: (1) Scattering force due to the radiation pressure, (2) Gradient force component of the radiation pressure, (3) Gradient force pulls the particle into the laser focus [Source: http://optical-tweezers.com/RadiationPressure.htm].

In Mie regime ($a \gg \lambda$) [134], the optical forces can be computed from simple ray optics approach (Fig. 5.11) which can be explained with the momentum transfer associated with the bending of light. It is known that light carries both the linear and the angular momentum and can thus exert forces and torque on matter. Optical tweezers exploit this fundamental property only to trap objects. The momentum carried by light is proportional to its energy and in the direction of propagation. Any change in the direction of light, by reflection or refraction, will result in a change of the momentum of the light. If an object bends the light, changing its momentum, conservation of momentum requires that the object must undergo an equal and opposite momentum change. This give rise to a force acting on the object which has been described in the Fig. 5.11 for (a) x and y direction as well as for (b) z direction. The light rays get refracted as soon as they travel through the particle which brings change in direction and leads to the change in momentum of light. According to Newton's third law, this has to be balanced by an equal and opposite change in momentum of the particle. Then the particle will move into the focal spot of the laser where the forces on the particle will be balanced and thus formed the stable 3d trap. Ray optics can be used to describe the effects of a strongly focused laser beam over a transparent dielectric particle, whose index of refraction is greater than the surrounding medium.

Whereas, in Rayleigh regime ($a \ll \lambda$), the particle or object is treated as electric dipole in an electric field. The expression for the gradient force (F_{grad}) and the scattering force (F_{scat}) for trapped objects in the Rayleigh regime are given as [132]:

$$\mathbf{F_{grad}} = \frac{-n_m}{2}\alpha_p \nabla \mathbf{E}^2 = \frac{-n_m^3 a^3}{2}\left(\frac{m^2-1}{m^2-2}\right)\nabla \mathbf{E}^2, \tag{5.25}$$

$$\mathbf{F_{scat}} = \frac{n_m P_{scat}}{c} = \frac{n_m I}{c}\frac{128 a^6 \pi^5}{3\lambda^4}\left(\frac{m^2-1}{m^2+2}\right)^2. \tag{5.26}$$

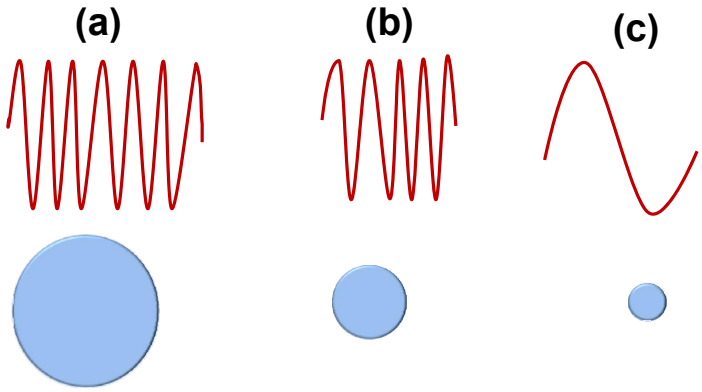

Figure 5.10: Image (a) represents the Mie regime where the object is much larger than the laser wavelength (object size $> 10\lambda$). Image (b) represents the Lorentz-Mie regime where the object is approximately the same dimensions as the laser wavelength. Image (c) represents the Rayleigh regime where the object is much smaller than the laser wavelength (object size $< \lambda/20$).

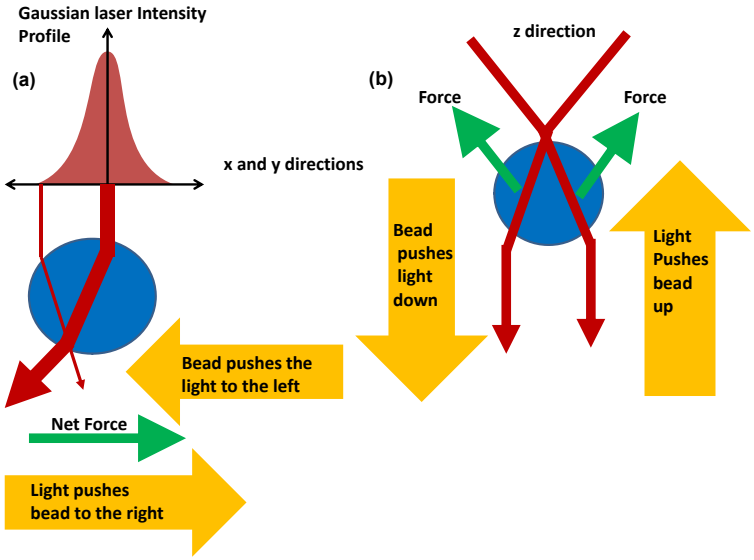

Figure 5.11: Ray optics description of the gradient force (a) A transparent bead is illuminated by a parallel beam of light with an intensity gradient increasing from left to right, (b) The bead is illuminated by a focused beam of light with a radial intensity gradient to form a stable trap in three dimension.

and the scattering cross-section of the sphere, σ_{sc}, is [135]

$$\sigma_{sc} = \frac{128a^6\pi^5}{3\lambda^4}\left(\frac{m^2-1}{m^2+2}\right)^2, \tag{5.27}$$

where ∇ is the gradient operator, $\mathbf{E}$ is the electric field vector, $m = n_s/n_m$ is the ratio between the refractive index of the sphere (n_s), and that of the surrounding medium (n_m), λ is the wavelength, c is the speed of light, a is the radius of the sphere, I is the intensity, P_{scat} is the scattered power and α_p is the polarizability of the sphere. As the gradient force is proportional to polarizability, so a sphere with a high polarizability will be trapped more strongly than a less polarizable sphere.

The regime between Mie and Rayleigh is called Lorentz-Mie regime where neither the ray optics nor the point dipole approach is valid and can be explained only by the electromagnetic theories [136–140] which involve the treatment of either time dependent or time harmonic Maxwell equations using appropriate boundary conditions.

5.3.2 Role of twisted light over Gaussian beams in optical tweezers (OT)

In most of the applications of OT, it is the linear momentum of light that is transferred to the trap objects but as we know that light can carry angular momentum too which can be further divided into the spin angular momentum associated with circular polarization and the orbital angular momentum related with twisted phase-fronts. It means that the light beams carrying orbital angular momentum (OAM) such as Laguerre-Gaussian beams (LG) (explained in chapter 2) can be used in the trapping of microscopic objects. These beams exert torques to twist or rotate microscopic objects. Now, when the trapping beam is scattered by the object in the trap altering either spin or orbital angular momentum results in the optical torque which can be measured optically without any calibration procedure as shown in Fig. 5.12 [141].

In 1986, Ashkin et al. [132] explained that when a focused laser beam interacts with a small particle, two forces named the scattering force along the direction of light propagation and the gradient force in the direction of the spatial light gradient (explained in above Section 5.3.1) have a key importance. They showed that the low absorbing dielectric spherical particles with a refractive index (n_p) higher than the surrounding medium or liquid (n_0) can also be trapped in three dimension by using a strongly focused Gaussian beam. Whereas, in the trapping of spherical low index particles such as bubbles and droplets, the direction of the gradient force gets reversed and the particle experiences a force away from the maximum intensity region which results in the repulsion of low index particles from the beam axis. Optical tweezers (OT) based on the Laguerre-Gaussian (LG) beams popularly known as twisted light can overcome this problem, as the LG beams is associated with helical wavefronts which is an annular intensity distribution with a zero on-axis intensity also referred as optical vortex. In optical vortex, the low index particles again experiences the gradient force directed to the beam axis and thus enable three dimensional stable trapping of the hollow glass spheres within the range of 2 to 50 μm in diameter [143]. It has been explained that

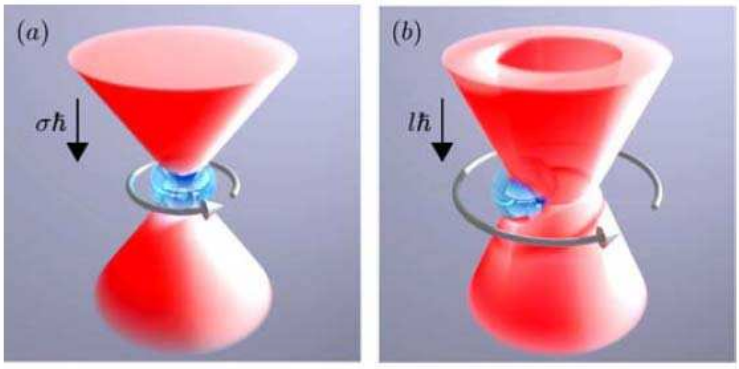

Figure 5.12: Angular momentum transfer in optical tweezers. Rotation of a trapped object can be induced by (a), the transfer of spin angular momentum using a circular polarized beam or (b), the transfer of orbital angular momentum using a beam such as high order Laguerre-Gaussian or Bessel beam [141].

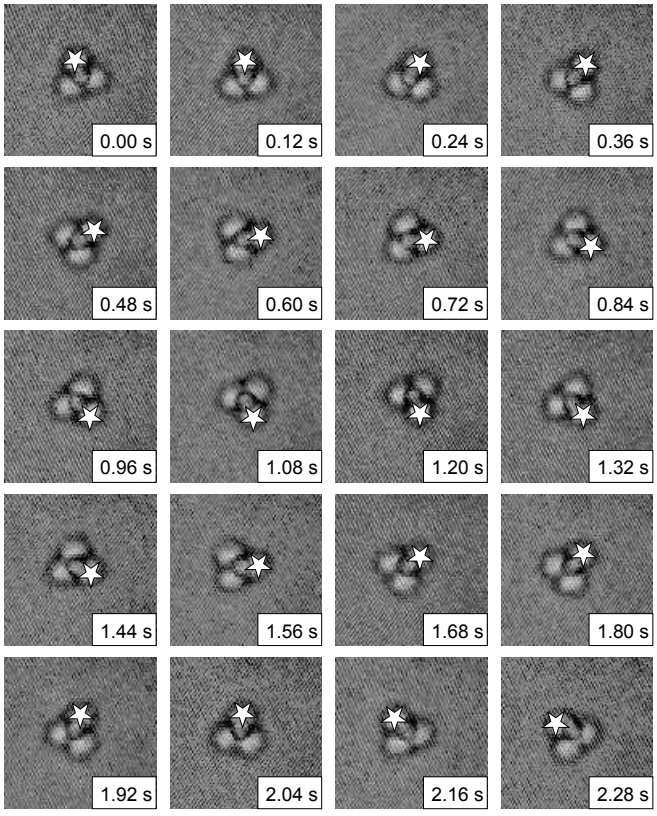

Figure 5.13: Reversal of rotation of absorbing polystyrene spheres trapped in a helical beam [142].

the successful trapping requires a position of stable equilibrium where the net gradient and the scattering forces are balanced. For a low index particle ($n_p < n_0$) such as water droplets in acetophenone (4 – 20 μm in diameter) and hollow glass sphere in water (12 – 30 μm diameter) in a strongly focused vortex beam, the equilibrium position occurs on the optical axis just above the focal plane [33, 144] and for the high index particles which can also simultaneously trapped by vortex beams to the normal position just below the beam focus. The transverse trapping attributes to the gradient and the scattering forces directed to vortex core whereas the longitudinal trapping results from the balanced scattering and gradient forces. The other major advantage of the LG beam over the conventional Gaussian beam in OT is related to the optical trapping of absorbing particles [142]. Although, optical tweezers using conventional Gaussian beam works well for most dielectric particles but the absorbing particles experience a much higher scattering force that often destructs a stable trap. Therefore, the optical vortex based tweezers are more efficient than the conventional Gaussian beam based one. Fig. 5.13 shows the trapping of the absorbing particles (polystyrene spheres) in the LG modes. These modes makes the particles trapped and rotated. Although, the particles normally trapped with optical tweezers are highly transparent, usually some absorption occurs. However, when the absorbability of micron sized particles becomes high enough, the radiation pressure becomes much greater than the gradient force, and they can no longer be trapped using the dipole forces. These absorbing particles are then affected primarily by the radiation pressure, whereby the momentum of absorbed light is transferred to the particle. In the LG beam modes, the laser intensity is concentrated in a ring of light: which means that the radiation force along the beam axis is less than for the Gaussian mode and hence, the radiation trapping becomes comparatively more strong which makes the LG modes more advantageous over Gaussian modes.

An additional advantage of the vortex beams based optical tweezers (OVT) over Gaussian beams is that the particle is exposed to lower intensities and thus is less likely to exhibit optically induced damage. On the contrary, in the conventional OT, the formation of stable traps requires high optical intensities($> 10^5$ W/cm^2) which can damage fragile objects such as biological cells or nano-particles. Optical vortex tweezers (OVT) are also proved to be more reliable in increasing the axial trapping efficiencies over the optical tweezers using the Gaussian beam. Simpson et al. [27] have made a comparison between the axial trapping efficiencies produced by OT using the Gaussian beam and the LG mode with an index value $\ell = 3$ by measuring the threshold laser power required to achieve the axial trapping of silica spheres within the range of 1-5 μm in diameter, suspended in water. It has been observed that for the spheres of 5 μm diameter, which are significantly larger than the diameter of the focused laser mode, the use of the LG mode with $\ell = 3$ as the trapping beam improves the axial efficiency of the OT by a factor of approximately 2. Even, it has also been seen that both the axial and the lateral trapping efficiencies can be improved with the LG modes in 'inverted' optical tweezers [145]. In the inverted geometry based optical tweezers, the trapping beam is directed upwards allowing easy and unrestricted access to the sample which has more applications in biomedical field whereas in the case of conventional optical tweezers, the trapping beam is directed downwards to the sample. It has been

concluded out that for spheres with size larger than the diameter of the focused beam, the use of high mode LG modes is highly improves the axial trapping efficiency of optical tweezers while the lateral trapping remains unaltered and for small-size spheres the TEM_{00} Gaussian beam is more recommendable.

On the contrary, recently in 2012 [146], it has been demonstrated that the transverse or lateral trapping efficiency can also be enhanced on dielectric sphere by the high order LG beams in Rayleigh regime i.e where radius of trapped sphere is less than the wavelength of the beam. It was investigated that for Rayleigh particles, the LG beams with $\ell = 0$ improves the transverse trapping effect with increasing value of p compared to Gaussian beam; while the axial trapping remains the same, although the central trapping region reduces as p increases. However, for the high order LG modes (i.e. $\ell \geq 1$), it has been found that the maximal transverse gradient forces increase with the increasing of p values and the axial radiation forces reduce slightly, therefore an optimal selection on the value of p and ℓ is necessary for obtaining an optimal optical guiding effect. Thus, the above mentioned facts are really helpful to draw the conclusion on the efficiency of the LG beams over the Gaussian beams in optical trapping process.

5.4 Optical trapping, guiding and acceleration of neutral atoms with twisted light

It is a well known fact that the classical interaction of a free electron with a rapidly oscillating, spatially inhomogeneous electromagnetic fields results in the so called ponderomotive force on the electron directed towards the regions of low intensity. The same fact can be used in the case of ponderomotive interaction of an optical field with Rydberg atom as it is comprised of an electron that is weakly bound to an ionic core through Coulomb interaction, thus considered as a free electron. Hence, a Rydberg atom immersed in an optical field can be described by the three coordinates system i.e. R (position of the Rydberg atom center of mass), r (relative coordinate between the Rydberg electron and the ionic core) and ρ (describes the quiver motion of the driven oscillation of the electron in the applied field) as shown in Fig. 5.14.

Our present work is motivated by a recent experimental study on the acceleration of neutral atoms in a strong Gaussian laser beam [10] where the captivity of Rydberg electron in the ponderomotive potential of a strongly focused Gaussian beam is observed. Hence, the captivity of Rydberg electron can be explained on the basis of the three step model (details are given in section 5.2). Eichmann and his coworkers [10] explained that the helium's electron, which oscillates vigorously near its ionic core in response to the laser field, still lacks enough energy after the pulse to escape the core of the atom. As a result, the electron is recaptured by the core in a bound excited state. However, during the oscillation, the strongly focused laser beam induces a ponderomotive force which leads to the ultra-strong acceleration of neutral atoms. We adopt a similar physical picture as in [10], namely the three-step model for strong field ionization [114], according to which the valence electron tunnels out of the atom near the

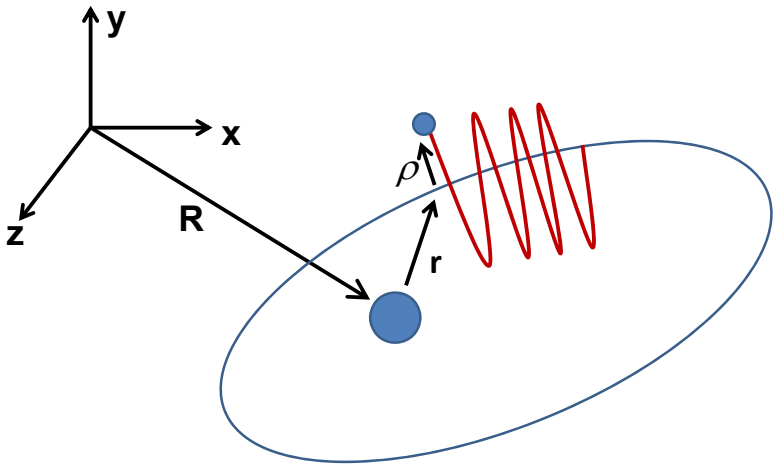

Figure 5.14: Relevant coordinates for a Rydberg atom immersed in an applied optical field.

laser peak field. The escaping electron propagates in the laser field and may eventually be recaptured into the atom.

Our findings based on the analysis of the classical trajectories are summarized as follows: The atom as a whole attains a net internal twist due to the transfer of a net angular momentum ℓ to the electron as it traverses the region of high intensity. Since the increase of ℓ enhances the centrifugal barrier, the electron is recaptured into outer orbits. Thus, this procedure might be useful for the generation of Rydberg atoms with internal orbital currents and for spin manipulation in spin-orbit coupled systems, e.g. as discussed in Refs. [67, 69]. Furthermore, depending on the initial velocity and the position of the atom with respect to the optical axis, due to the ponderomotive potential the atom is trapped within the beam or accelerated away from it. This effect can be used for laser guiding and structuring of a distribution of neutral atoms and might be useful for lithographic applications. Here, we will present numerical calculations for the parameters given in the experiment with He atoms [10] and contrast with the results for the Gaussian beam.

5.4.1 Results and discussion

The electric field **E** of the LG beam in cylindrical coordinates (with the z axis chosen to be along the incident beam propagation direction) is [24, 97](for more details, see chapter2):-

$$\mathbf{E}(r,\phi,z,t) = \mathbf{e}\frac{C_p^{|\ell|}}{w(z)}\left(\frac{\sqrt{2}r}{w(z)}\right)^{|\ell|}\exp\left(\frac{-r^2}{w^2(z)}\right) \times L_p^{|\ell|}\left(\frac{2r^2}{w^2(z)}\right)\exp\left[i(kz+\omega t+\phi_0)\right]\exp(i\ell\phi)+\text{c.c.}, \quad (5.28)$$

where r and ϕ are the radial and azimuthal coordinates, respectively, ℓ is the topological charge of the optical vortex, and **e** is the polarization vector. $L_p^{|\ell|}(x)$ is the associated

Laguerre polynomial, $C_p^{|\ell|}$ is a normalization constant, $w(z) = w_0\sqrt{1+\left(\frac{z}{z_0}\right)^2}$ is the radius of the beam at z, w_0 is the half beam width, k is the wave number in vacuum and ϕ_0 is a constant phase of the field.

In the present work, for an atom in the presence of the light beam with OAM, we have considered the classical equations of motions for the structureless ionic core and one active electron including the electrostatic forces $\mathbf{F}_c$. The calculations are performed for He atoms [10]. As outlined below for a sizable effect the spatial intensity gradient is essential. Hence, the atoms of interest here are those initially residing around $r \approx w_0/4$. Adopting the three-step model [114], we consider the second step where the liberated electron traverses the high-intensity region of the field (Eq. 5.28). The electron moving in the plane perpendicular to the light propagation direction attains an angular twist, i.e. a velocity component ($\dot{r}_\perp(t) = r\dot{\phi}(t)$) perpendicular to the radial direction to the ion. This is important insofar, as the electron re-entering the ionic fields has then the classical angular momentum $L = mr\dot{r}_\perp(t) = mr^2\dot{\phi}(t)$ and therefore, it experiences a centrifugal barrier pushing it to outer orbits. Note, that this barrier can be enhanced by increasing ℓ. The sign of ℓ sets the sign of the orbital current. This procedure can thus be used to "pump" the atom to an oriented high Rydberg state.
However, the above description contrasts the previous study by Babiker et al. [147] on the OAM exchange between the light carrying OAM and molecules. In their work, they stated on the basis of explicit analysis that during the interaction of the light beams containing OAM with molecules, the exchange of the OAM occurs only between the light beams and center of mass motion i.e. no internal electron state of an atom would participate in any OAM exchange in the electric dipole interactions. And only in the case of weaker electric quadruple interaction, the exchange of the OAM can take place involving all the three subsystems, i.e. the light, the internal motion and the center of mass motion. Recently, an another interesting study by Lloyd et al. [148] came into picture in favor of our predicted result that OAM exchange indeed can occur even in the case of electric dipole transition. It has been argued theoretically that the electric dipole transition involves the transfer of a single unit of OAM between the light beam and the internal motion of the atomic electron whereas the higher multi-pole transitions leads to the exchange of two or more units of OAM between the vortex beam and the atomic system. For illustrations, we have solved numerically the Lagrangian equations of motion and Fig. 5.15 shows the trajectory of an electron in the $x-y$ plane endorsing the above statements (for detailed calculations, refer to Appendix C).

The radial drift motion of an atom on the other hand is determined by the ponderomotive forces $\mathbf{F}_{pe}$ and $\mathbf{F}_{pi}$ on the electron and the ion, respectively, i.e.

$$m_e\ddot{\mathbf{r}}_1 = \mathbf{F}_{pe} + \mathbf{F}_c \tag{5.29}$$

$$m_i\ddot{\mathbf{r}}_2 = \mathbf{F}_{pi} - \mathbf{F}_c. \tag{5.30}$$

Here m_e (m_i) is the mass of the electron (ion) and $\mathbf{r}_e$ ($\mathbf{r}_i$) is the radial coordinate of the electron (ion). Switching over to a relative and a center of mass $\mathbf{R}$ coordinate and neglecting terms of the order $1/m_i^2$ we find for the drift motion of the atom as a whole the following equation of motion (for detailed calculations, refer to Appendix B);

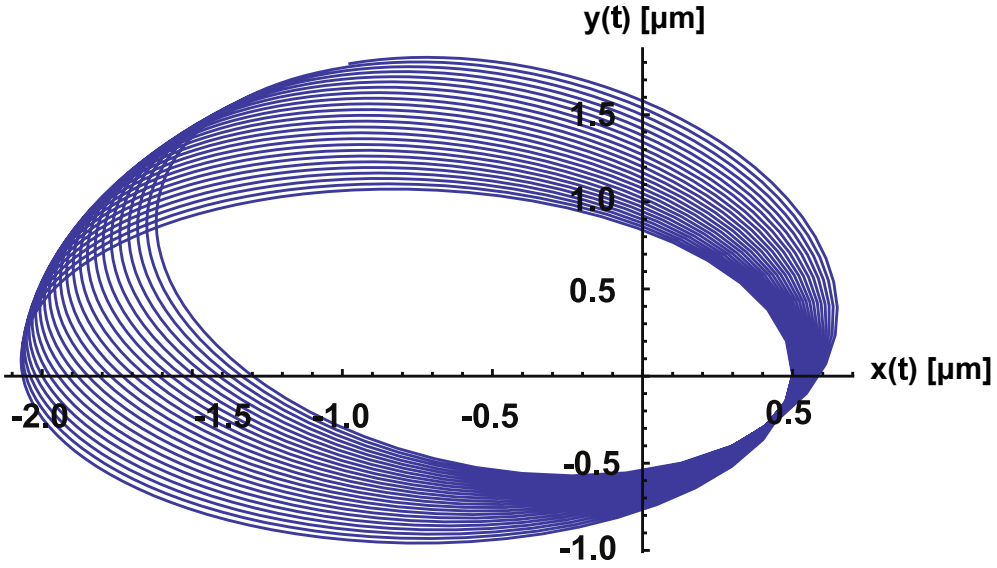

Figure 5.15: Trajectory of an electron in the LG beam with Coulomb potential for following parameters: $m_e = 9.1 \times 10^{-31}$kg, $w_0 = 1.05\ \mu$m, $\omega = 25.2 \times 10^{14}$ rad/s, $\phi_0 = 98.5°$, $E_0 = 0.7 \times 10^8$ V/m, $\ell = 1$, $p = 0$, $\mathbf{r}(t=0) = (0.5\text{ nm}, 0, 0)$, $\dot{\mathbf{r}}(t=0) = (10^6\text{ m/s}, 0, 0)$.

$$M\ddot{\mathbf{R}}(t) = -\frac{e^2}{4m_e\omega^2}\nabla|\mathbf{E}|^2, \tag{5.31}$$

where M is the atom mass and e is the electron charge.

The ponderomotive force depends on the gradient of the spatial distribution of the intensity I. For LG_0^1 mode, we have

$$I \propto |E|^2 = 4E_0^2\frac{2r^2}{w^2(z)}\exp\left(\frac{-2r^2}{w^2(z)}\right). \tag{5.32}$$

The ponderomotive potential is thus approximately parabolic near the intensity minima. The number of minima is determined by p. We note that ℓ does not appear explicitly in I, similar to the case of $\ell = 0$ corresponding to the Gaussian beam. Hence, sufficiently cold atoms starting near the radial minima of the beam perform harmonic motion with a frequency determined by the radial shape of the beam. For a fixed waist and overall shape of the beam the frequencies can be increased by increasing p. Along the beam the atoms drift almost freely with their initial velocities. In general the atom center of mass $\mathbf{R}$ evolves according to

$$\ddot{\mathbf{R}}(t) = \frac{-e^2E_0^2}{M\omega^2}\left(\frac{4R}{w^2(z)}\right)\exp\left(\frac{-2R^2}{w^2(z)}\right)\left(1 - \frac{2R^2}{w^2(z)}\right). \tag{5.33}$$

To obtain analytical results we argue as follows: atoms initially located around the optical axis or at distances larger than the beam waist w_0 hardly experience any laser-induced drift. The maximum laser influence is exerted on atoms residing initially at $R = w_0/2$ (with $\dot{\mathbf{R}}(t = 0) = 0$). For these atoms, integrating over the full pulse laser

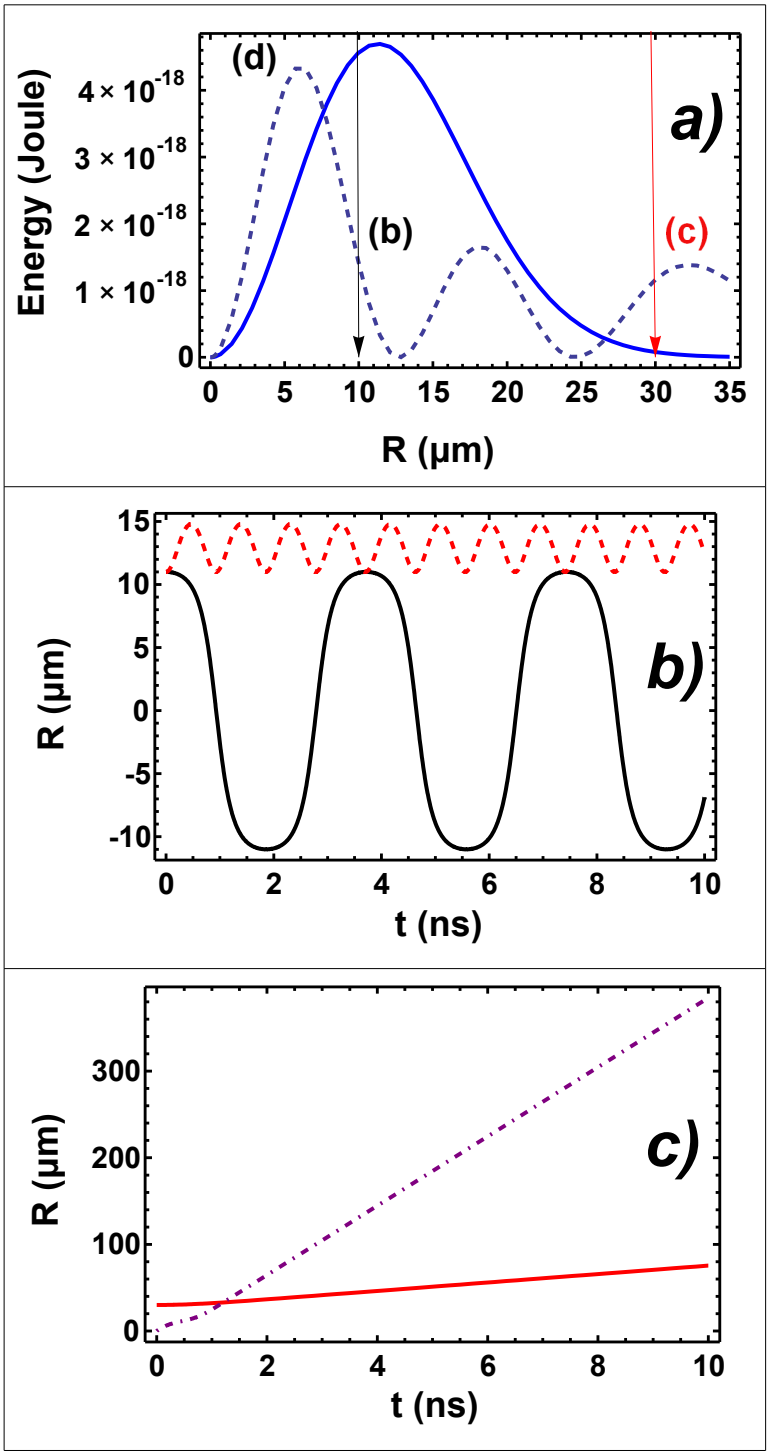

Figure 5.16: Dynamics of a neutral He atom in the LG beam for different initial conditions. (a) Ponderomotive potential of LG_0^1 mode (blue curve) and LG_2^1 mode (dashed curve) with the following parameters: $M(\text{He atom}) = 6.68 \times 10^{-27}$kg, $w_0 = 16\,\mu$m, $\omega = 28.96 \times 10^{14}$ rad/s ($\lambda = 650$ nm), $E_0 = 5.3 \times 10^7$ V/m; (b) The neutral atom resides initially at $\mathbf{R}(t = 0) = 10\,\mu$m, $\dot{\mathbf{R}}(t = 0) = 0$ m/s for $\ell = 1$, $p = 0$ (black curve), $\ell = 1$, $p = 2$ (dashed red curve); (c) Scattering of atom at $\mathbf{R}(t = 0) = 30\,\mu$m, $\dot{\mathbf{R}}(t = 0) = 0$ m/s (indicated with the red curve) and with $\dot{\mathbf{R}}(t = 0) = 40 \times 10^3$ m/s (indicated with the dot-dashed curve).

duration, we find the maximum velocity $v_{\max}(z)$ (For full derivations, refer Appendix B) to be given by

$$\mathbf{v}_{\max}(z) = \frac{-I_0 \exp(-0.5)\sqrt{\pi}\tau}{2M\omega^2 w_0 \left(1 + \left(\frac{z}{z_0}\right)^2\right)^{\frac{3}{2}}}, \tag{5.34}$$

where τ is the pulse width, I_0 is the field intensity and ω is the laser frequency. This relation we confirmed by solving fully numerically for Eq. 5.33. For numerical illustration we employ similar laser and atom parameters as in the experiment ([10]). Fig. 5.16 shows the dynamics of the neutral He atoms initially residing at different radial positions with respect to the optical axis. The ponderomotive potential for LG_0^1 mode (blue curve) and LG_2^1 (dashed curve) are shown in Fig. 5.16(a) that evidences the trapping of a neutral He atom initially located at $R = 10\ \mu$m (Fig. 5.16(b)) for $\ell = 1$, $p = 0$ with the black curve and for $\ell = 1$, $p = 2$ with the red dashed curve (while repeating the same calculations) where it exhibits the rapid oscillations through the focus of the LG beam. For the initial value of the radial coordinate $R = 30\ \mu$m, the atom is scattered as indicated by the red curve in Fig. 5.16(c). For a high initial velocity, i.e. 40×10^3 m/s, the atom remains initially bound to the potential well but at a later time it escapes (dot-dashed curve). In this case the situation resembles the one for the Gaussian beam and indeed the velocities are similar to those reported in [10]. In summary, a neutral atom attains an internal twist and can be trapped in the radial minima of an LG beam where it oscillates with a frequency determined by the spatial distribution of the beam.

5.4.2 Conclusions

We studied the dynamics of neutral atoms in the focused, high-intensity laser beam carrying an orbital angular momentum. The dynamics of the active electron in the high intensity region of the laser field results in a transfer of a net angular momentum to the atom. The ponderomotive force on the electrons translates into an unbounded or a bounded drift radial motion of the whole atom, depending on its initial velocity and position in the beam. In particular, the radial minima of the beam may trap the neutral atoms, an effect which may be exploited for an atom guiding, structuring and for lithographic applications.

Chapter 6

Summary

In the recent years, the light beams carrying orbital angular momentum have received an increased attention by Optics fraternity. Here, in the present work we focused on the study of optical nonlinear phenomena such as self-focusing and de-focusing, optical phase conjugation and particle dynamics with twisted light. For these helical wavefront beams, the Poynting vector unlike spin angular momentum is not parallel to the beam axis, thus results into many interesting nonlinear effects by varying beam parameters like beam waist, frequency and intensity. The studies on self-focusing of light beams have been carried out for many years but here for the first time to the best of our knowledge, the self-focusing and de-focusing of twisted light in nonlinear media has been pointed out by solving the differential wave equation for the beam width parameter analytically using the WKB and paraxial approximations. The results thus obtained are analyzed and illustrated for typical experimental situations with the help of numerical calculations. The predicted focusing effect can be used for the realization of more versatile optical tweezers, e.g. for creating tighter and stronger three-dimensional optical traps for both high and low refractive index particles in comparison to their surrounding media by crossing two LG beams at the focused distance. Next, a study on the reflection and the transmission of twisted light through multilayered structure containing phase conjugating interfaces has been conducted and the obtained results are found in good agreement with the previous experimental studies containing single PCM layer structure. The key idea behind this work is to calculate the interference pattern for reflected beams resulting from the multilayered structure with phase conjugating interfaces. It has been observed that the interference pattern for reflected beams has dependence on the thickness of the medium and thus prove helpful to obtain information on the depth profile of refractive in-homogeneities of composite optical materials. The obtained results can also be useful to simulate a certain experimental situation to study the phase conjugation in composite optical materials.

Since the last few decades, the field of optical micromanipulation using twisted light has emerged as one of the key advances seen in the modern photonics. The major point of implementing the twisted light in trapping is that angular as well as linear momentum can be transferred to trapped objects. In such light beams, the OAM offers itself as a useful tool in the exertion of torques on particles by simply increasing the

azimuthal index in contrast to the optical torque arising from spin angular momentum which varies with optical power and is limited to $\hbar$ per photon. Here, we used the same principle of optical trapping to study the dynamics of charged particles and neutral atoms by calculating their classical trajectories using the focused, high-intensity laser beam carrying an orbital angular momentum. Our present work is motivated by a recent experimental study on the acceleration of neutral atoms in a strong Gaussian laser beam carried out by Eichmann et al. [10]. Considering the same fact, we studied the dynamics of the active electron of the neutral He atom in the high intensity region of the laser field carrying OAM which results into a transfer of a net angular momentum to the atom. The ponderomotive force on the electrons translates into an unbounded or a bounded drift radial motion of the whole atom, depending on its initial velocity and position in the beam. In particular, the radial minima of the beam may trap the neutral atoms and this effect can be used for an atom guiding, structuring and in lithographic applications.

Appendix A: Calculation on reflection and transmission coefficients of twisted light for quadra-layered structure

Here, we have considered a quadra-layered dielectric structure (the layers and related quantities are indexed by 0, 1, 2, 3) as sketched in Fig. A.1, similar as described in chapter 4. The only difference is that here, we will present calculations for structure containing three layers of PCM. All the layers are parallel and infinitely extended. The monochromatic LG beam with the frequency ω propagates in the medium 0 and impinges onto the medium 1. The interface between medium 0 and medium 1, the interface between medium 1 and 2 as well as the interface between medium 2 and medium 3 are phase conjugating, d_1 is the thickness of the layer 1 and d_2 is the thickness of the layer 2 (our treatment is also valid when the whole medium 1 is phase conjugating). We denote the incident, the reflected and the transmitted fields by i, r and t respectively and n_0, n_1, n_2 and n_3 are the refractive indices of the media 0, 1, 2 and 3 respectively.

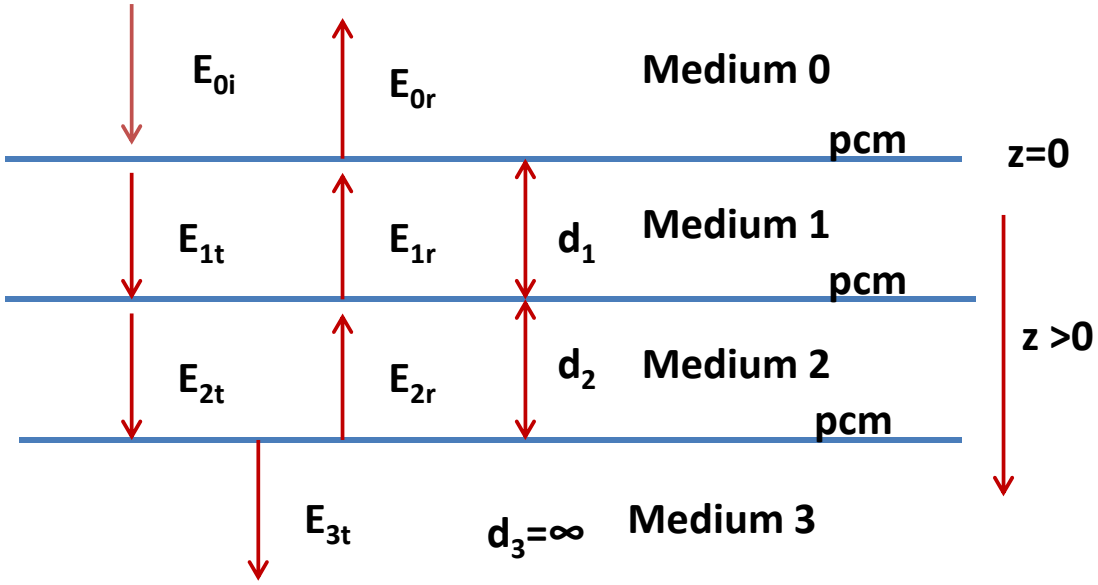

Figure A.1: Schematic representation of the propagation of LG beam in a multi layer dielectric structure. The interfaces with PCM are indicated.

The electric field E (at the beam waist, $z=0$) of the LG beam in cylindrical coordinates (with the z axis chosen to be along the incident beam propagation direction) is given by [24, 97].

$$E = \frac{C_p^{|\ell|}}{w_0}\left(\frac{\sqrt{2}r}{w_0}\right)^{|\ell|}\exp\left(\frac{-r^2}{w_0^2}\right)L_p^{|\ell|}\left(\frac{2r^2}{w_0^2}\right)\exp i(k_0 nz-\omega t)\exp(i\ell\phi), \tag{A.1}$$

where r and ϕ are the radial and azimuthal coordinates, ℓ can take any integer value either positive or negative and means physically the topological charge of the optical vortex. $L_p^{|\ell|}$ is the associated Laguerre polynomial, $C_p^{|\ell|}$ is a normalization constant, w_0 is the half beam width, and $k_0=\omega/c$ is the wave number in vacuum.

To keep the notation simple we can incorporate the condition on ℓ due to time reversal property of phase conjugating mirror by the ansatz

$$E_{0i} = \bar{E}_{0i}e^{i\ell\phi} = \frac{C_p^{|\ell|}}{w_0}\left(\frac{\sqrt{2}r}{w_0}\right)^{|\ell|}\exp\left(\frac{-r^2}{w_0^2}\right)L_p^{|\ell|}\left(\frac{2r^2}{w_0^2}\right)e^{i(k_0 n_0 z+\ell\phi)},(z\le 0) \tag{A.2}$$

$$E_{0r} = \bar{E}_{0r}e^{-i\ell\phi} = r_0\frac{C_p^{|\ell|}}{w_0}\left(\frac{\sqrt{2}r}{w_0}\right)^{|\ell|}\exp\left(\frac{-r^2}{w_0^2}\right)L_p^{|\ell|}\left(\frac{2r^2}{w_0^2}\right)e^{-i(k_0 n_0 z+\ell\phi)},(z\le 0) \tag{A.3}$$

$$E_{1t} = \bar{E}_{1t}e^{i\ell\phi} = t_1\frac{C_p^{|\ell|}}{w_0}\left(\frac{\sqrt{2}r}{w_0}\right)^{|\ell|}\exp\left(\frac{-r^2}{w_0^2}\right)L_p^{|\ell|}\left(\frac{2r^2}{w_0^2}\right)e^{i(k_0 n_1 z+\ell\phi)},(0\le z\le d_1) \tag{A.4}$$

$$E_{1r} = \bar{E}_{1r}e^{-i\ell\phi} = r_1\frac{C_p^{|\ell|}}{w_0}\left(\frac{\sqrt{2}r}{w_0}\right)^{|\ell|}\exp\left(\frac{-r^2}{w_0^2}\right)L_p^{|\ell|}\left(\frac{2r^2}{w_0^2}\right)e^{-i(k_0 n_1 z+\ell\phi)},(0\le z\le d_1) \tag{A.5}$$

$$E_{2t} = \bar{E}_{2t}e^{i\ell\phi} = t_2\frac{C_p^{|\ell|}}{w_0}\left(\frac{\sqrt{2}r}{w_0}\right)^{|\ell|}\exp\left(\frac{-r^2}{w_0^2}\right)L_p^{|\ell|}\left(\frac{2r^2}{w_0^2}\right)e^{-i(k_0 n_1 z+\ell\phi)},(d_1\le z\le (d_1+d_2)) \tag{A.6}$$

$$E_{2r} = \bar{E}_{2r}e^{-i\ell\phi} = r_2\frac{C_p^{|\ell|}}{w_0}\left(\frac{\sqrt{2}r}{w_0}\right)^{|\ell|}\exp\left(\frac{-r^2}{w_0^2}\right)L_p^{|\ell|}\left(\frac{2r^2}{w_0^2}\right)e^{-i(k_0 n_1 z+\ell\phi)},(d_1\le z\le (d_1+d_2)) \tag{A.7}$$

$$E_{3t} = \bar{E}_{3t}e^{i\ell\phi} = t_3\frac{C_p^{|\ell|}}{w_0}\left(\frac{\sqrt{2}r}{w_0}\right)^{|\ell|}\exp\left(\frac{-r^2}{w_0^2}\right)L_p^{|\ell|}\left(\frac{2r^2}{w_0^2}\right)e^{i[k_0 n_2(z-d_1)+\ell\phi]},(z\ge (d_1+d_2)). \tag{A.8}$$

Here, the temporal factor $\exp(-i\omega t)$ is omitted for the sake of simplicity. To evaluate the reflection and the transmission coefficients, we shall apply the condition of the continuity and smoothness of the field at the boundaries within the structure [100, 101] (note the behavior of ℓ upon scattering is already accounted for by the ansatz (Eq. A.2-Eq. A.8))

$$\left[\bar{E}_{0i}+\bar{E}_{0r}\right]_{z=0} = \left[\bar{E}_{1t}+\bar{E}_{1r}\right]_{z=0}, \tag{A.9a}$$

$$\left[\bar{E}_{1t}+\bar{E}_{1r}\right]_{z=d_1} = \left[\bar{E}_{2t}+\bar{E}_{2r}\right]_{z=d_1}, \tag{A.9b}$$

$$\left[\bar{E}_{2t}+\bar{E}_{2r}\right]_{z=(d_1+d_2)} = \left[\bar{E}_{3t}\right]_{z=(d_1+d_2)}. \tag{A.9c}$$

and

$$\left[\frac{\partial \bar{E}_{0i}}{\partial z}+\frac{\partial \bar{E}_{0r}}{\partial z}\right]_{z=0} = \left[\frac{\partial \bar{E}_{1t}}{\partial z}+\frac{\partial \bar{E}_{1r}}{\partial z}\right]_{z=0}, \tag{A.10a}$$

$$\left[\frac{\partial \bar{E}_{1t}}{\partial z}+\frac{\partial \bar{E}_{1r}}{\partial z}\right]_{z=d_1} = \left[\frac{\partial \bar{E}_{2t}}{\partial z}+\frac{\partial \bar{E}_{2r}}{\partial z}\right]_{z=d_1}, \tag{A.10b}$$

$$\left[\frac{\partial \bar{E}_{2t}}{\partial z}+\frac{\partial \bar{E}_{2r}}{\partial z}\right]_{z=(d_1+d_2)} = \left[\frac{\partial \bar{E}_{3t}}{\partial z}\right]_{z=(d_1+d_2)}. \tag{A.10c}$$

Eqs.(A.9) and (A.10) lead to

$$1+r_0 = t_1+r_1, \tag{A.11a}$$

$$t_1e^{i\alpha_1}+r_1e^{-i\alpha_1} = t_2+r_2, \tag{A.11b}$$

$$t_2e^{i\alpha_2}+r_2e^{-i\alpha_2} = t_3, \tag{A.11c}$$

and

$$n_0[1-r_0] = n_1[t_1-r_1], \tag{A.12a}$$

$$n_1[t_1e^{i\alpha_1}-r_1e^{-i\alpha_1}] = n_2(t_2-r_2), \tag{A.12b}$$

$$n_2[t_2e^{i\alpha_2}-r_2e^{-i\alpha_2}] = n_3t_3. \tag{A.12c}$$

With the notation $\alpha_1 = k_0n_1d_1$, $\alpha_2 = k_0n_2d_2$.

On solving Eq. A.11 and Eq. A.12, we obtain the reflection coefficient r_0 related to the propagation in the medium 0, and the reflection and the transmission coefficients related to the propagation in the medium 1, 2 and 3 denoted by r_1, t_1, r_2, t_2 and t_3, respectively. Explicitly, the reflection and the transmission coefficients are

$$r_0 = \left(\frac{an_0-a_1n_1}{an_0+a_1n_1}\right), \tag{A.13}$$

$$r_1 = \frac{1+r_0-r_2A^-e^{-i\alpha_1}}{1-e^{-2i\alpha_1}}, \tag{A.14}$$

$$t_1 = e^{-i\alpha_1}(r_2A^- - r_1e^{-i\alpha_1}), \tag{A.15}$$

$$r_2 = -\frac{2n_1e^{-i\alpha_1}(1+r_0)}{n_2A^+(e^{-2i\alpha_1}-1)-n_1A^-(e^{-2i\alpha_1}+1)}, \tag{A.16}$$

$$t_2 = -r_2e^{-2i\alpha_2}N, \tag{A.17}$$

$$t_3 = \frac{n_2}{n_3}(t_2e^{i\alpha_2}-r_2e^{-i\alpha_2}). \tag{A.18}$$

where

$$a = (e^{-2i\alpha_1}-1)^2(n_1A^-+n_2A^+)-2n_1A^-e^{-2i\alpha_1}(e^{-2i\alpha_1}-1),$$

$$a_1 = [(e^{-2i\alpha_1}-1)(n_1A^-+n_2A^+)-2n_1A^-e^{-2i\alpha_1}](e^{-2i\alpha_1}-1)+4n_1A^-e^{-2i\alpha_1},$$

$$A^+ = 1+e^{-2i\alpha_2}N,$$

$$A^- = 1-e^{-2i\alpha_2}N,$$

$$N = \left(\frac{n_3+n_2}{n_3-n_2}\right).$$

After substituting for the reflection and the transmission coefficients in the Eqs. (A.2-A.8), we can obtain the electromagnetic fields that describe the propagation of the LG beam through the system depicted in Fig. A.1.

Appendix B: Calculation on Lagrangian equations of motion of the LG beam in the absence of Coulomb potential

The lagrangian of a particle with charge 'q' moving with the velocity '**v**' in an electromagnetic field with the scalar and vector potentials φ and **A** respectively can be written as [100]:

$$L = \frac{1}{2}mv^2 - q\varphi + \frac{q}{c}\mathbf{A}\cdot\mathbf{v} \tag{B.1}$$

For $\varphi = 0$, $z = 0$, the Eq. B.1 reduces to

$$L = \frac{1}{2}mv^2 + \frac{q}{c}\mathbf{A}\cdot\mathbf{v} \tag{B.2}$$

$$L = \frac{1}{2}m(\dot{r}^2 + r^2\dot{\phi}^2) + \frac{q}{c}\mathbf{A}\cdot\mathbf{v} \quad (\because x = r\cos\phi) \tag{B.3}$$

$$\tag{B.4}$$

While the term $\mathbf{A}\cdot\mathbf{v}$ can be written as

$$\mathbf{A}\cdot\mathbf{v} = -r(t)\sin\phi(t)\dot{\phi}(t)f_{\ell p} + \dot{r}(t)\cos\phi(t)f_{\ell p}, \tag{B.5}$$

where the $f_{\ell p}$, the field amplitude of the LG beam is [97]

$$f_{\ell p}^{LG}(r,\phi,z=0,t) = \frac{C_p^{|\ell|}}{w_0}E_0\left(\frac{\sqrt{2}r(t)}{w_0}\right)^{|\ell|}\exp\left(\frac{-r(t)^2}{w_0^2}\right)L_p^{|\ell|}\left(\frac{2r(t)^2}{w_0^2}\right)\exp i(\phi_0 + \omega t + \ell\phi(t)), \tag{B.6}$$

where r, ϕ and z are cylindrical coordinates, ℓ is the azimuthal index, p is the radial mode index, w_0 is the beam waist at $z = 0$, $L_p^{|\ell|}\left(\frac{2r^2}{w(z)^2}\right)$ is the associated Laguerre Polynomial and $C_p^{|\ell|}$ is the normalization constant.

For $\ell > 1$, $p = 0$, the value of Laguerre polynomial i.e. $L_p^{|\ell|}\left(\frac{2r(t)^2}{w_0^2}\right) = 1$ [149], then the Eq. B.6 reduces to (in more generalized form as):

$$f_{\ell p}(r,\phi,t) = E_0\left(\frac{\sqrt{2}r(t)}{w_0}\right)^{\lambda}\exp\left(\frac{-r(t)^2}{w_0^2}\right)\sin(\omega t + \phi_0 + \lambda\phi(t)) \tag{B.7}$$

where λ represents the azimuthal index ℓ and the term $\frac{C_p^{|\ell|}}{w_0}$ has been omitted in the further steps for simplicity.

The Euler-Lagrangian equations of motion in cylindrical coordinates are [100]:

$$\frac{d}{dt}\left(\frac{\partial L}{\partial \dot{r}}\right) = \frac{\partial L}{\partial r}, \tag{B.8}$$

$$\frac{d}{dt}\left(\frac{\partial L}{\partial \dot{\phi}}\right) = \frac{\partial L}{\partial \phi}, \tag{B.9}$$

$$\frac{d}{dt}\left(\frac{\partial L}{\partial \dot{z}}\right) = \frac{\partial L}{\partial z}. \tag{B.10}$$

Now Eq. B.8 implies

$$\frac{d}{dt}\left(\frac{\partial L}{\partial \dot{r}}\right) = \frac{\partial L}{\partial r}, \tag{B.11}$$

The L.H.S. of Eq. B.11 equals to

$$\begin{aligned}
\frac{d}{dt}\left(\frac{\partial L}{\partial \dot{r}}\right) &= \frac{d}{dt}\frac{\partial}{\partial \dot{r}(t)}\left[\frac{m}{2}\left(\dot{r}(t)^2 + r(t)^2\dot{\phi}(t)^2\right) + \frac{q}{c}\left(\dot{r}(t)\cos\phi(t) f_{\ell p} - r(t)\sin\phi(t)\dot{\phi}(t) f_{\ell p}\right)\right] \\
&= \frac{d}{dt}\left(m\dot{r}(t) + \frac{q}{c}\left(f_{\ell p}\cos\phi(t)\right)\right) \\
&= m\ddot{r}(t) + \frac{q}{c}\frac{d}{dt}\left(f_{\ell p}\cos\phi(t)\right) \\
&= m\ddot{r}(t) - \frac{q}{c} f_{\ell p}\sin\phi(t)\dot{\phi}(t) + \frac{q}{c}\cos\phi(t)\frac{d}{dt}\left(f_{\ell p}\right) \\
&= m\ddot{r}(t) - \frac{q}{c} f_{\ell p}\sin\phi(t)\dot{\phi}(t) + \frac{q}{c}E_0\cos\phi(t)\left(\frac{\sqrt{2}r(t)}{w_0}\right)^{\lambda}\exp\left(\frac{-r(t)^2}{w_0^2}\right)B \\
&+ \frac{q}{c}E_0\cos\phi(t)\left(\frac{\sqrt{2}r(t)}{w_0}\right)^{\lambda}\exp\left(\frac{-r(t)^2}{w_0^2}\right)\left(\frac{-2r(t)}{w_0^2}\right)r'(t)\Theta_1 \\
&+ \frac{q}{c}E_0\cos\phi(t)\left(\frac{\sqrt{2}}{w_0}\right)^{\lambda}\lambda[r(t)]^{\lambda-1}r'(t)\exp\left(\frac{-r(t)^2}{w_0^2}\right)\Theta_1 \\
&= m\ddot{r}(t) - \frac{q}{c} f_{\ell p}\sin\phi(t)\dot{\phi}(t) + \frac{q}{c}E_0\cos\phi(t)\left(\frac{\sqrt{2}r(t)}{w_0}\right)^{\lambda}\exp\left(\frac{-r(t)^2}{w_0^2}\right)B \\
&+ \frac{q}{c}E_0\cos\phi(t)\left(\frac{\sqrt{2}r(t)}{w_0}\right)^{\lambda}\exp\left(\frac{-r(t)^2}{w_0^2}\right)\left(\frac{-2r(t)}{w_0^2}\right)r'(t)\Theta_1 A\,,
\end{aligned} \tag{B.12}$$

The R.H.S. of Eq. B.11 equals to

$$\begin{aligned}
\frac{\partial L}{\partial r} &= \frac{\partial}{\partial r}\left[\frac{m}{2}\left(\dot{r}(t)^2 + r(t)^2\dot{\phi}(t)^2\right) + \frac{q}{c}\left(\dot{r}(t)\cos\phi(t) f_{\ell p} - r(t)\sin\phi(t)\dot{\phi}(t) f_{\ell p}\right)\right] \\
&= mr(t)\dot{\phi}(t)^2 + \frac{q}{c}\frac{\partial}{\partial r}\left(\dot{r}(t)\cos\phi(t) f_{\ell p} - r(t)\sin\phi(t)\dot{\phi}(t) f_{\ell p}\right) \\
&= mr(t)\dot{\phi}(t)^2 + \frac{q}{c}\dot{r}(t)\cos\phi(t)\frac{\partial}{\partial r}(f_{\ell p}) - \frac{q}{c}\sin\phi(t)\dot{\phi}(t)\frac{\partial}{\partial r}\left(r(t) f_{\ell p}\right) \\
&= mr(t)\dot{\phi}(t)^2 + \frac{q}{c}\dot{r}(t)\cos\phi(t)E_0\left(\frac{\sqrt{2}}{w_0}\right)^{\lambda}\exp\left(\frac{-r(t)^2}{w_0^2}\right)\Theta_1 A \\
&- \frac{q}{c}\dot{\phi}(t)\sin\phi(t) f_{\ell p} - \frac{q}{c}r(t)\dot{\phi}(t)\sin\phi(t)E_0\left(\frac{\sqrt{2}}{w_0}\right)^{\lambda}\exp\left(\frac{-r(t)^2}{w_0^2}\right)\Theta_1 A \\
&= mr(t)\dot{\phi}(t)^2 - \frac{q}{c}\dot{\phi}(t)\sin\phi(t) f_{\ell p} + \frac{q}{c}E_0\left(\frac{\sqrt{2}}{w_0}\right)^{\lambda}\exp\left(\frac{-r(t)^2}{w_0^2}\right)\Theta_1 A \\
&\quad \times\dot{r}(t)\cos\phi(t) - r(t)\dot{\phi}(t)\sin\phi(t). \qquad \text{(B.13)}
\end{aligned}$$

After substituting Eq. B.12 and Eq. B.13 in Eq. B.11, we get

$$\ddot{r}(t) = r(t)\dot{\phi}(t)^2 - \frac{q}{mc}E_0\left(\frac{\sqrt{2}}{w_0}\right)^{\lambda} exp\left(\frac{-r(t)^2}{w_0^2}\right)\left(r(t)\dot{\phi}(t)\sin\phi(t)\Theta_1 A + [r(t)]^{\lambda}\cos\phi(t)B\right), \qquad \text{(B.14)}$$

where $A = \left([r(t)]^{\lambda}\left(\frac{-2r(t)}{w_0^2}\right) + \lambda[r(t)]^{\lambda-1}\right)$, $B = \cos(\omega t + \phi_0 + \lambda\phi(t))(\omega + \lambda\phi'(t))$ and $\Theta_1 = \sin(\omega t + \phi_0 + \lambda\phi(t))$.

Now Eq. B.9 implies

$$\frac{d}{dt}\left(\frac{\partial L}{\partial\dot{\phi}}\right) = \frac{\partial L}{\partial\phi} \qquad \text{(B.15)}$$

The L.H.S. of Eq. B.15 equals to

$$\begin{aligned}
\frac{d}{dt}\left(\frac{\partial L}{\partial \dot{\phi}}\right) &= \frac{d}{dt}\frac{\partial}{\partial \dot{\phi}}\left[\frac{m}{2}\left(\dot{r}(t)^2 + r(t)^2\dot{\phi}(t)^2\right) + \frac{q}{c}\left(\dot{r}(t)\cos\phi(t) f_{\ell p} - r(t)\sin\phi(t)\dot{\phi}(t) f_{\ell p}\right)\right] \\
&= \frac{d}{dt}\left(mr(t)^2\dot{\phi}(t) - \frac{q}{c} f_{\ell p} r(t)\sin\phi(t)\right) \\
&= mr(t)^2\ddot{\phi}(t) + 2mr(t)\dot{r}(t)\dot{\phi}(t) - \frac{q}{c}\frac{d}{dt}\left(f_{\ell p} r(t)\sin\phi(t)\right) \\
&= mr(t)^2\ddot{\phi}(t) + 2mr(t)\dot{r}(t)\dot{\phi}(t) \\
&- \frac{q}{c}E_0 r(t)\sin\phi(t)\left(\frac{\sqrt{2}r(t)}{w_0}\right)^{\lambda}\exp\left(\frac{-r(t)^2}{w_0^2}\right)B \\
&- \frac{q}{c}E_0 r(t)\sin\phi(t)\left(\frac{\sqrt{2}r(t)}{w_0}\right)^{\lambda}\exp\left(\frac{-r(t)^2}{w_0^2}\right)\left(-\frac{2r(t)}{w_0^2}\right)r'(t)\Theta_1 \\
&- \frac{q}{c}E_0 r(t)\sin(t)\left(\frac{\sqrt{2}}{w_0}\right)^{\lambda}\lambda[r(t)]^{\lambda-1}r'(t)\exp\left(\frac{-r(t)^2}{w_0^2}\right)\Theta_1 \\
&- \frac{q}{c} f_{\ell p}\left(r(t)\dot{\phi}(t)\cos\phi(t) + \dot{r}(t)\sin(t)\right) \qquad \text{(B.16)}
\end{aligned}$$

The R.H.S. of Eq. B.15 equals to

$$\begin{aligned}
\frac{\partial L}{\partial \phi} &= \frac{\partial}{\partial \phi}\left[\frac{m}{2}\left(\dot{r}(t)^2 + r(t)^2\dot{\phi}(t)^2\right) + \frac{q}{c}\left(\dot{r}(t)\cos\phi(t) f_{\ell p} - r(t)\sin\phi(t)\dot{\phi}(t) f_{\ell p}\right)\right] \\
&= \frac{q}{c}\frac{\partial}{\partial \phi}\left(\dot{r}(t)\cos\phi(t) f_{\ell p} - r(t)\dot{\phi}(t)\sin\phi(t) f_{\ell p}\right) \\
&= \frac{q}{c}\dot{r}(t)\frac{\partial}{\partial \phi}\left(f_{\ell p}\cos\phi(t)\right) - \frac{q}{c}r(t)\dot{\phi}(t)\frac{\partial}{\partial \phi}\left(\sin\phi(t) f_{\ell p}\right) \\
&= -\frac{q}{c}\dot{r}(t)\sin\phi(t) f_{\ell p} + \frac{q}{c}\dot{r}(t)\cos\phi(t)\frac{\partial}{\partial \phi}(f_{\ell p}) \\
&- \frac{q}{c}r(t)\dot{\phi}(t)\cos\phi(t) f_{\ell p} - \frac{q}{c}r(t)\dot{\phi}(t)\sin\phi(t)\frac{\partial}{\partial \phi}(f_{\ell p}) \\
&= -\frac{q}{c}\dot{r}(t)\sin\phi(t) f_{\ell p} + \frac{\lambda q}{c}\dot{r}(t)\cos\phi(t)E_0\left(\frac{\sqrt{2}r(t)}{w_0}\right)^{\lambda}\exp\left(\frac{-r(t)^2}{w_0^2}\right)\Theta_2 \\
&- \frac{q}{c}r(t)\dot{\phi}(t)\cos\phi(t) f_{\ell p} - \frac{\lambda q}{c}r(t)\dot{\phi}(t)\sin\phi(t)E_0\left(\frac{\sqrt{2}r(t)}{w_0}\right)^{\lambda}\exp\left(\frac{-r(t)^2}{w_0^2}\right)\Theta_2 \\
&= -\frac{q}{c} f_{\ell p}\left(r(t)\dot{\phi}(t)\cos\phi(t) + \dot{r}(t)\sin\phi(t)\right) + \frac{\lambda q}{c}E_0\left(\frac{\sqrt{2}r(t)}{w_0}\right)^{\lambda}\exp\left(\frac{-r(t)^2}{w_0^2}\right)\Theta_2 \\
&\times\left(\dot{r}(t)\cos\phi(t) - r(t)\dot{\phi}(t)\sin\phi(t)\right) \qquad \text{(B.17)}
\end{aligned}$$

After substituting Eq. B.16 and Eq. B.17 in Eq. B.15, we get

$$
\begin{aligned}
r(t)^2\ddot{\phi}(t) = &-2mr(t)\dot{r}(t)\dot{\phi}(t) + \frac{q}{mc}E_0\left(\frac{\sqrt{2}r(t)}{w_0}\right)^{\lambda}\exp\left(\frac{-r(t)^2}{w_0^2}\right)\Theta_2 \\
&\times\left(\lambda\dot{r}(t)\cos\phi(t) - \lambda r(t)\dot{\phi}(t)\sin\phi(t) + r(t)\sin\phi(t)(\omega + \lambda\phi'(t))\right) \qquad \text{(B.18)} \\
&+ \frac{q}{mc}E_0 r(t)\sin\phi(t)\left(\frac{\sqrt{2}}{w_0}\right)^{\lambda}\exp\left(\frac{-r(t)^2}{w_0^2}\right)r'(t)\Theta_1 A
\end{aligned}
$$

where $\Theta_2 = \cos(\omega t + \phi_0 + \lambda\phi(t))$.

Appendix C: Calculation on Lagrangian equations of motion of the LG beam in the presence of Coulomb potential

The Lagrangian of a particle with charge 'q' moving with the velocity '**v**' in an electromagnetic field with the scalar and vector potentials φ and **A** respectively and in the soft Coulomb potential V_c can be written as [100]:

$$L = \frac{1}{2}mv^2 - q\varphi + \frac{q}{c}\mathbf{A}\cdot\mathbf{v} - V_c \tag{C.1}$$

where $V_c = -\frac{1}{\sqrt{1+r(t)^2}}$ is called Coulomb potential. For $\varphi = 0$, $z = 0$, the Eq. C.1 reduces to

$$L = \frac{1}{2}mv^2 + \frac{q}{c}\mathbf{A}\cdot\mathbf{v} - V_c \tag{C.2}$$

$$L = \frac{1}{2}m(\dot{r}^2 + r^2\dot{\phi}^2) + \frac{q}{c}\mathbf{A}\cdot\mathbf{v} - V_c \quad (\because x = r\cos\phi) \tag{C.3}$$

While the term $\mathbf{A}\cdot\mathbf{v}$ can be written as

$$\mathbf{A}\cdot\mathbf{v} = -r(t)\sin\phi(t)\dot{\phi}(t)f_{\ell p} + \dot{r}(t)\cos\phi(t)f_{\ell p}\ , \tag{C.4}$$

where the $f_{\ell p}$, the field amplitude of the LG beam is [97]

$$f_{\ell p}^{LG}(r,\phi,z=0,t) = \frac{C_p^{|\ell|}}{w_0}E_0\left(\frac{\sqrt{2}r(t)}{w_0}\right)^{|\ell|}\exp\left(\frac{-r(t)^2}{w_0^2}\right)L_p^{|\ell|}\left(\frac{2r(t)^2}{w_0^2}\right)\exp i(\phi_0+\omega t+\ell\phi(t))f(t) \tag{C.5}$$

where r, ϕ and z are cylindrical coordinates, ℓ is the azimuthal index, p is the radial mode index, w_0 is the beam waist at $z = 0$, $L_p^{|\ell|}\left(\frac{2r^2}{w(z)^2}\right)$ is the associated Laguerre Polynomial, $C_p^{|\ell|}$ is the normalization constant and $f(t) = \exp\left(-\frac{(t-t_0)^2}{\tau^2}\right)$ is the pulse envelope with τ is the pulse width.

For $\ell > 1$, $p = 0$, the value of Laguerre polynomial i.e. $L_p^{|\ell|}\left(\frac{2r(t)^2}{w_0^2}\right) = 1$ [149], then the Eq. C.5 reduces to (in more generalized form as):

$$f_{\ell p}(r,\phi,t) = E_0\left(\frac{\sqrt{2}r(t)}{w_0}\right)^{\lambda}\exp\left(\frac{-r(t)^2}{w_0^2}\right)\sin(\omega t + \phi_0 + \lambda\phi(t))f(t) \tag{C.6}$$

where λ represents the azimuthal index ℓ and the term $\frac{C_p^{|\ell|}}{w_0}$ has been omitted in the further steps for simplicity.

The Euler-Lagrangian equations of motion in cylindrical coordinates can be given as [100]:

$$\frac{d}{dt}\left(\frac{\partial L}{\partial \dot{r}}\right) = \frac{\partial L}{\partial r}, \tag{C.7}$$

$$\frac{d}{dt}\left(\frac{\partial L}{\partial \dot{\phi}}\right) = \frac{\partial L}{\partial \phi}, \tag{C.8}$$

$$\frac{d}{dt}\left(\frac{\partial L}{\partial \dot{z}}\right) = \frac{\partial L}{\partial z}. \tag{C.9}$$

Now Eq. C.7 implies

$$\frac{d}{dt}\left(\frac{\partial L}{\partial \dot{r}}\right) = \frac{\partial L}{\partial r}\,, \tag{C.10}$$

The L.H.S. of Eq. C.10 equals to

$$\begin{aligned}
\frac{d}{dt}\left(\frac{\partial L}{\partial \dot{r}}\right) &= \frac{d}{dt}\frac{\partial}{\partial \dot{r}(t)}\left[\frac{m}{2}\left(\dot{r}(t)^2 + r(t)^2\dot{\phi}(t)^2\right) + \frac{q}{c}\left(\dot{r}(t)\cos\phi(t) f_{\ell p} - r(t)\sin\phi(t)\dot{\phi}(t) f_{\ell p}\right) - V_c\right] \\
&= \frac{d}{dt}\left(m\dot{r}(t) + \frac{q}{c}\left(f_{\ell p}\cos\phi(t)\right)\right) \\
&= m\ddot{r}(t) + \frac{q}{c}\frac{d}{dt}\left(f_{\ell p}\cos\phi(t)\right) \\
&= m\ddot{r}(t) - \frac{q}{c} f_{\ell p}\sin\phi(t)\dot{\phi}(t) + \frac{q}{c}\cos\phi(t)\frac{d}{dt}\left(f_{\ell p}\right) \\
&= m\ddot{r}(t) - \frac{q}{c} f_{\ell p}\sin\phi(t)\dot{\phi}(t) + \frac{q}{c}E_0\cos\phi(t)\left(\frac{\sqrt{2}r(t)}{w_0}\right)^{\lambda}\exp\left(\frac{-r(t)^2}{w_0^2}\right) B f(t) \\
&+ \frac{q}{c}E_0\cos\phi(t)\left(\frac{\sqrt{2}r(t)}{w_0}\right)^{\lambda}\exp\left(\frac{-r(t)^2}{w_0^2}\right)\left(\frac{-2r(t)}{w_0^2}\right) r'(t)\Theta_1 f(t) \\
&+ \frac{q}{c}E_0\cos\phi(t)\left(\frac{\sqrt{2}}{w_0}\right)^{\lambda}\lambda[r(t)]^{\lambda-1} r'(t)\exp\left(\frac{-r(t)^2}{w_0^2}\right)\Theta_1 f(t) \\
&+ \frac{q}{c}E_0\cos\phi(t)\left(\frac{\sqrt{2}r(t)}{w_0}\right)^{\lambda}\exp\left(\frac{-r(t)^2}{w_0^2}\right)\Theta_1 f(t)\left(-\frac{2(t-t_0)}{\tau^2}\right) \\
&= m\ddot{r}(t) - \frac{q}{c} f_{\ell p}\sin\phi(t)\dot{\phi}(t) + \frac{q}{c}E_0\cos\phi(t)\left(\frac{\sqrt{2}r(t)}{w_0}\right)^{\lambda}\exp\left(\frac{-r(t)^2}{w_0^2}\right) B \\
&+ \frac{q}{c}E_0\cos\phi(t)\left(\frac{\sqrt{2}r(t)}{w_0}\right)^{\lambda}\exp\left(\frac{-r(t)^2}{w_0^2}\right)\left(\frac{-2r(t)}{w_0^2}\right) r'(t)\Theta_1 A \\
&+ \frac{q}{c}E_0\cos\phi(t)\left(\frac{\sqrt{2}r(t)}{w_0}\right)^{\lambda}\exp\left(\frac{-r(t)^2}{w_0^2}\right)\Theta_1 f(t)\left(-\frac{2(t-t_0)}{\tau^2}\right),
\end{aligned} \tag{C.11}$$

The R.H.S. of Eq. C.10 equals to

$$\begin{aligned}
\frac{\partial L}{\partial r} &= \frac{\partial}{\partial r}\left[\frac{m}{2}\left(\dot{r}(t)^2 + r(t)^2\dot{\phi}(t)^2\right) + \frac{q}{c}\left(\dot{r}(t)\cos\phi(t) f_{\ell p} - r(t)\sin\phi(t)\dot{\phi}(t) f_{\ell p} - V_c\right)\right] \\
&= mr(t)\dot{\phi}(t)^2 + \frac{q}{c}\frac{\partial}{\partial r}\left(\dot{r}(t)\cos\phi(t) f_{\ell p} - r(t)\sin\phi(t)\dot{\phi}(t) f_{\ell p} - V_c\right) \\
&= mr(t)\dot{\phi}(t)^2 + \frac{q}{c}\dot{r}(t)\cos\phi(t)\frac{\partial}{\partial r}(f_{\ell p}) - \frac{q}{c}\sin\phi(t)\dot{\phi}(t)\frac{\partial}{\partial r}[r(t) f_{\ell p} - \frac{\partial}{\partial r}(V_c)] \\
&= mr(t)\dot{\phi}(t)^2 + \frac{q}{c}\dot{r}(t)\cos\phi(t) E_0\left(\frac{\sqrt{2}}{w_0}\right)^{\lambda}\exp\left(\frac{-r(t)^2}{w_0^2}\right)\Theta_1 A \\
&- \frac{q}{c}\dot{\phi}(t)\sin\phi(t) f_{\ell p} - \frac{q}{c}r(t)\dot{\phi}(t)\sin\phi(t) E_0\left(\frac{\sqrt{2}}{w_0}\right)^{\lambda}\exp\left(\frac{-r(t)^2}{w_0^2}\right)\Theta_1 A \\
&- \left(\frac{r(t)}{(1+r(t)^2)^{\frac{3}{2}}}\right). \qquad \text{(C.12)}
\end{aligned}$$

After substituting Eq. C.11 and Eq. C.12 in Eq. C.10, we get

$$\begin{aligned}
\ddot{r}(t) =& r(t)\dot{\phi}(t)^2 - \frac{q}{mc}E_0\left(\frac{\sqrt{2}}{w_0}\right)^{\lambda}\exp\left(\frac{-r(t)^2}{w_0^2}\right) f(t)\Bigg(r(t)\dot{\phi}(t)\sin\phi(t)\Theta_1 A \\
&+ [r(t)]^{\lambda}\cos\phi(t) B + [r(t)]^{\lambda}\cos\phi(t)\Theta_1\left(-\frac{2(t-t_0)}{\tau^2}\right)\Bigg) - \frac{1}{m}\left(\frac{r(t)}{(1+r(t)^2)^{\frac{3}{2}}}\right) \qquad \text{(C.13)}
\end{aligned}$$

where $A = \left([r(t)]^{\lambda}\left(\frac{-2r(t)}{w_0^2}\right) + \lambda[r(t)]^{\lambda-1}\right)$, $B = \cos(\omega t + \phi_0 + \lambda\phi(t))(\omega + \lambda\phi'(t))$ & $\Theta_1 = \sin(\omega t + \phi_0 + \lambda\phi(t))$.

Eq. C.8 implies

$$\frac{d}{dt}\left(\frac{\partial L}{\partial \dot{\phi}}\right) = \frac{\partial L}{\partial \phi}\,, \qquad \text{(C.14)}$$

The L.H.S. of Eq. C.14 equals to

$$\begin{aligned}
\frac{d}{dt}\left(\frac{\partial L}{\partial \dot{\phi}}\right) &= \frac{d}{dt}\frac{\partial}{\partial \dot{\phi}}\left[\frac{m}{2}\left(\dot{r}(t)^2 + r(t)^2\dot{\phi}(t)^2\right) + \frac{q}{c}\left(\dot{r}(t)\cos\phi(t) f_{\ell p} - r(t)\sin\phi(t)\dot{\phi}(t) f_{\ell p} - V_c\right)\right] \\
&= \frac{d}{dt}\left(mr(t)^2\dot{\phi}(t) - \frac{q}{c} f_{\ell p} r(t)\sin\phi(t)\right) \\
&= mr(t)^2\ddot{\phi}(t) + 2mr(t)\dot{r}(t)\dot{\phi}(t) - \frac{q}{c}\frac{d}{dt}\left(f_{\ell p} r(t)\sin\phi(t)\right) \\
&= mr(t)^2\ddot{\phi}(t) + 2mr(t)\dot{r}(t)\dot{\phi}(t) \\
&- \frac{q}{c}E_0 r(t)\sin\phi(t)\left(\frac{\sqrt{2}r(t)}{w_0}\right)^{\lambda}\exp\left(\frac{-r(t)^2}{w_0^2}\right)\Theta_1\exp\left(\frac{-(t-t_0)^2}{\tau^2}\right)\left(\frac{-2(t-t_0)}{\tau^2}\right) \\
&- \frac{q}{c}E_0 r(t)\sin\phi(t)\left(\frac{\sqrt{2}r(t)}{w_0}\right)^{\lambda}\exp\left(\frac{-r(t)^2}{w_0^2}\right) B f(t) \\
&- \frac{q}{c}E_0 r(t)\sin\phi(t)\left(\frac{\sqrt{2}r(t)}{w_0}\right)^{\lambda}\exp\left(\frac{-r(t)^2}{w_0^2}\right)\left(\frac{-2r(t)}{w_0^2}\right) r'(t)\Theta_1 f(t) \\
&- \frac{q}{c}E_0 r(t)\sin(t)\left(\frac{\sqrt{2}}{w_0}\right)^{\lambda}\lambda[r(t)]^{\lambda-1} r'(t)\exp\left(\frac{-r(t)^2}{w_0^2}\right)\Theta_1 f(t) \\
&- \frac{q}{c} f_{\ell p}\left(r(t)\dot{\phi}(t)\cos\phi(t) + \dot{r}(t)\sin(t)\right), \qquad \text{(C.15)}
\end{aligned}$$

The R.H.S. of Eq. C.14 equals to

$$\begin{aligned}
\frac{\partial L}{\partial \phi} &= \frac{\partial}{\partial \phi}\left[\frac{m}{2}\left(\dot{r}(t)^2 + r(t)^2\dot{\phi}(t)^2\right) + \frac{q}{c}\left(\dot{r}(t)\cos\phi(t) f_{\ell p} - r(t)\sin\phi(t)\dot{\phi}(t) f_{\ell p} - V_c\right)\right] \\
&= \frac{q}{c}\frac{\partial}{\partial \phi}\left(\dot{r}(t)\cos\phi(t) f_{\ell p} - r(t)\dot{\phi}(t)\sin\phi(t) f_{\ell p}\right) \\
&= \frac{q}{c}\dot{r}(t)\frac{\partial}{\partial \phi}\left(f_{\ell p}\cos\phi(t)\right) - \frac{q}{c} r(t)\dot{\phi}(t)\frac{\partial}{\partial \phi}\left(\sin\phi(t) f_{\ell p}\right) \\
&= -\frac{q}{c}\dot{r}(t)\sin\phi(t) f_{\ell p} + \frac{q}{c}\dot{r}(t)\cos\phi(t)\frac{\partial}{\partial \phi}(f_{\ell p}) \\
&- \frac{q}{c} r(t)\dot{\phi}(t)\cos\phi(t) f_{\ell p} - \frac{q}{c} r(t)\dot{\phi}(t)\sin\phi(t)\frac{\partial}{\partial \phi}(f_{\ell p}) \\
&= -\frac{q}{c}\dot{r}(t)\sin\phi(t) f_{\ell p} + \frac{\lambda q}{c}\dot{r}(t)\cos\phi(t) E_0\left(\frac{\sqrt{2}r(t)}{w_0}\right)^{\lambda}\exp\left(\frac{-r(t)^2}{w_0^2}\right)\Theta_2 f(t) \\
&- \frac{q}{c} r(t)\dot{\phi}(t)\cos\phi(t) f_{\ell p} - \frac{\lambda q}{c} r(t)\dot{\phi}(t)\sin\phi(t) E_0\left(\frac{\sqrt{2}r(t)}{w_0}\right)^{\lambda}\exp\left(\frac{-r(t)^2}{w_0^2}\right)\Theta_2 \\
&= -\frac{q}{c} f_{\ell p}\left(r(t)\dot{\phi}(t)\cos\phi(t) + \dot{r}(t)\sin\phi(t)\right) + \frac{\lambda q}{c} E_0\left(\frac{\sqrt{2}r(t)}{w_0}\right)^{\lambda}\exp\left(\frac{-r(t)^2}{w_0^2}\right)\Theta_2 \\
&\times\left(\dot{r}(t)\cos\phi(t) - r(t)\dot{\phi}(t)\sin\phi(t)\right). \qquad \text{(C.16)}
\end{aligned}$$

On substituting Eq. C.15 and Eq. C.16 in Eq. C.14, we get

$$\begin{aligned} r(t)^2\ddot{\phi}(t) = &-2mr(t)\dot{r}(t)\dot{\phi}(t) + \frac{q}{mc}E_0\left(\frac{\sqrt{2}r(t)}{w_0}\right)^{\lambda}\exp\left(\frac{-r(t)^2}{w_0^2}\right)\Theta_2 f(t) \\ &\times\left(\lambda\dot{r}(t)\cos\phi(t) - \lambda r(t)\dot{\phi}(t)\sin\phi(t) + r(t)\sin\phi(t)(\omega + \lambda\phi'(t))\right) \\ &+ \frac{q}{mc}E_0 r(t)\sin\phi(t)\left(\frac{\sqrt{2}}{w_0}\right)^{\lambda}\exp\left(\frac{-r(t)^2}{w_0^2}\right)\Theta_1 f(t) \\ &\times\left([r(t)]^{\lambda}\left(\frac{-2(t-t_0)}{\tau^2}\right) + r'(t)A\right), \end{aligned} \tag{C.17}$$

where $\Theta_2 = \cos(\omega t + \phi_0 + \lambda\phi(t))$.

Appendix D: Calculations on Optical trapping of neutral atoms with the LG beam

The equations of motion for an electron and the ion in the ponderomotive forces i.e $\mathbf{F}_{\rm pe}$ and $\mathbf{F}_{\rm pi}$, respectively can be given as:

$$m_{\rm e}\ddot{\mathbf{r}}_1 = \mathbf{F}_{\rm pe} + \mathbf{F}_{\rm c}, \tag{D.1}$$

$$m_{\rm i}\ddot{\mathbf{r}}_2 = \mathbf{F}_{\rm pi} - \mathbf{F}_{\rm c}. \tag{D.2}$$

where $m_{\rm e}$ ($m_{\rm i}$) is the mass of the electron (ion) and $\mathbf{r}_{\rm e}$ ($\mathbf{r}_{\rm i}$) is the radial coordinate of the electron (ion).

Switching over to a relative and a center of mass $\mathbf{R}$ coordinate and neglecting terms of the order $1/m_{\rm i}^2$, the equation of motion for the drift motion of the atom as a whole can be given as:

$$M\ddot{\mathbf{R}} = -\frac{e^2}{4m_e\omega^2}\nabla|E|^2. \tag{D.3}$$

As the ponderomotive force depends on the gradient of the spatial distribution of the intensity I, therefore for LG_0^1 mode, we have

$$I \propto |\mathbf{E}|^2 = 4E_0^2\frac{2r^2w^2}{w^2(z)}\exp\left(\frac{-2r^2}{w^2(z)}\right), \tag{D.4}$$

where

$$w(z) = w_0\sqrt{1+\left(\frac{z}{z_0}\right)^2} \tag{D.5}$$

is the radius of the beam at z. And $\mathbf{E}$ is given as

$$\mathbf{E}(r,\phi,z,t) = \mathbf{e}\frac{C_p^{|\ell|}}{w(z)}\left(\frac{\sqrt{2}r}{w(z)}\right)^{|\ell|}\exp\left(\frac{-r^2}{w^2(z)}\right) \times L_p^{|\ell|}\left(\frac{2r^2}{w^2(z)}\right)\exp\left[i(kz+\omega t+\phi_0)\right]\exp(i\ell\phi)\,f(t) + \text{c.c.}, \tag{D.6}$$

where r and ϕ are the radial and azimuthal coordinates, respectively, ℓ is the topological charge of the optical vortex, and $\mathbf{e}$ is the polarization vector. $L_p^{\ell}(x)$ is the associated

Laguerre polynomial, C_p^{ℓ} is a normalization constant, w_0 is the half beam width, k is the wave number in vacuum and ϕ_0 is a constant phase and $f(t) = \exp\left(-\frac{t^2}{\tau^2}\right)$ is the laser pulse envelope, τ is the pulse width. On substituting the value of $|E|^2$ from Eq. D.4 in Eq. D.3, we can write now Eq. D.3 as

$$\begin{aligned} M\ddot{\mathbf{R}}(t) &= -\frac{e^2}{4m_e\omega^2}\frac{\partial}{\partial r}\left[4E_0^2\frac{2r^2w^2}{w^2(z)}\exp\left(\frac{-2r^2}{w^2(z)}\right)\right]f(t), \\ \ddot{\mathbf{R}}(t) &= -\frac{e^2E_0^2}{M\omega^2}\frac{\partial}{\partial r}\left[\frac{2r^2w^2}{w^2(z)}\exp\left(\frac{-2r^2}{w^2(z)}\right)\right]f(t) \quad (\because m_e = 1), \\ \ddot{\mathbf{R}}(t) &= -\frac{e^2E_0^2}{M\omega^2}\left[\frac{2r^2}{w^2(z)}\exp\left(-\frac{2r^2}{w^2(z)}\right)\left(-\frac{4r}{w^2(z)}\right) + \exp\left(-\frac{2r^2}{w^2(z)}\right)\left(\frac{4r}{w^2(z)}\right)\right]f(t). \end{aligned} \tag{D.7}$$

Then for the atom center of mass R, Eq. D.7 can be written as

$$\ddot{\mathbf{R}}(t) = -\frac{e^2E_0^2}{M\omega^2}\exp\left(-\frac{2R^2}{w^2(z)}\right)\left(\frac{4R}{w^2(z)}\right)\left(1-\frac{2R}{w^2(z)}\right)\exp\left(-\frac{t^2}{\tau^2}\right). \tag{D.8}$$

The atoms residing at $R = w_0/2$ with $\dot{R}(t=0)$, will experience the maximum laser, thus the maximum velocity can be given as

$$\begin{aligned} \dot{\mathbf{R}}(t) &= -\frac{e^2E_0^2}{M\omega^2}\exp\left(-\frac{2R^2}{w^2(z)}\right)\left(\frac{4R}{w^2(z)}\right)\left(1-\frac{2R}{w^2(z)}\right)\int_0^1\exp\left(-\frac{t^2}{\tau^2}\right)dt \\ &= -\frac{e^2E_0^2}{M\omega^2}\exp\left(-\frac{2R^2}{w^2(z)}\right)\left(\frac{4R}{w^2(z)}\right)\left(1-\frac{2R}{w^2(z)}\right)\frac{1}{2}\sqrt{\pi}\tau. \end{aligned} \tag{D.9}$$

Now on substituting the value of $w(z)$ from Eq. D.5 in above Eq. D.9, we get the expression for maximum velocity as:

$$v_{max} = -\frac{I_0\exp(-0.5)\sqrt{\pi}\tau}{2M\omega^2w_0\left(1+\left(\frac{z}{z_0}\right)^2\right)^{\frac{3}{2}}}, \tag{D.10}$$

where I_0 is the field intensity.

Bibliography

[1] J. F. Nye and M. V. Berry, "Dislocations in wave trains," *Proc. R. Soc. Lond. A*, vol. 336, p. 165, 1974.

[2] L. Allen, M. J. Padgett, and M. Babiker, "The orbital angular momentum of light," *Prog. Opt.*, vol. 39, p. 291, 1999.

[3] L. Allen, M. W. Beijersbergen, R. J. C. Spreeuw, and J. P. Woerdman, "Orbital angular momentum of light and the transformation of laguerre-gaussian laser modes," *Phys. Rev. A*, vol. 45, p. 8185, 1992.

[4] H. He, M. E. J. Friese, N. R. Heckenberg, and H. Rubinsztein-Dunlop, "Direct observation of transfer of angular momentum to absorptive particles from a laser beam with a phase singularity," *Phys. Rev. Lett.*, vol. 75, p. 826, 1995.

[5] R. A. Beth, "Mechanical detection and measurement of the angular momentum of light," *Phys. Rev.*, vol. 50, p. 115, 1936.

[6] G. A. Askar'yan, "Effects of the gradient of a strong electromagnetic beam on electrons and atoms," *Sov. Phys. JETP*, vol. 15, p. 1088, 1962.

[7] B. Zel'dovich, V. Popovichev, V. Ragul'skii, F. Faizullov, and P. Lebedev, "Connection between the wavefronts of the reflected and exciting light in stimulated mandel'stam-brillouin scattering," *Sov. Phys. JETP*, vol. 15, p. 109, 1972.

[8] A. Y. Okulov, "Angular momentum of photon and phase conjugation," *J. Phys. B: At. Mol. Opt. Phys.*, vol. 41, p. 101001, 2008.

[9] M. Woerdman, C. Alpmann, and C. Denz, "Self-pumped phase conjugation of light beams carrying orbital angular momentum," *Opt. Express*, vol. 17, p. 22791, 2009.

[10] U. Eichmann, T. Nubbemeyer, H. Rottke, and W. Sandner, "Acceleartion of neutral atom in strong short pulse laser fields," *Nature*, vol. 461, p. 1261, 2009.

[11] D. J. Griffiths, *Introduction to Electrodynamics*. New Jersey: Prentice Hall, 1999.

[12] M. E. J. Friese, T. A. Nieminen, N. R. Heckenberg, and H. Rubinsztein-Dunlop, "Optical alignment and spinning of laser-trapped microscopic particles," *Nature*, vol. 394, p. 348, 1998.

[13] E. Karimi, *Generation and manipulation of laser beams carrying orbital angular momentum for classical and quantum information applications*. PhD thesis, UNIVERSITÁ DEGLI STUDI DI NAPOLI 'FEDERICO II', 2009.

[14] J. P. Torres and L. Torner, *Twisted Photons*. Weinheim: Wiley-VCH, 2011.

[15] L. Allen, M. W. Beijersbergen, R. J. C. Spreeuw, and J. P. Woerdman, "Orbital angular momentum of light and the transformation of laguerre-gaussian laser modes," *Phys. Rev. A*, vol. 45, p. 8185, 1992.

[16] M. Padgett, J. Courtial, and L. Allen, "Light's orbital angular momentum," *Phys. Today*, vol. 57, p. 35, 2004.

[17] L. Allen, S. M. Barnett, and M. J. Padgett, *Optical angular momentum*. Bristol: Institute of Physics, 2003.

[18] V. Garcés-Chávez, D. McGloin, M. J. Padgett, W. Dultz, H. Schmitzer, and K. Dholakia, "Observation of the transfer of the local angular momentum density of a multiringed light beam to an optically trapped particle," *Phys. Rev. Lett.*, vol. 91, p. 093602, 2003.

[19] D. McGloin and K. Dholakia, "Bessel beam: diffraction in a new light," *Contemporary Phys.*, vol. 6, p. 15, 2005.

[20] J. Courtial, K. Dholakia, L. Allen, and M. J. Padgett, "Second-harmonic generation and the conservation of orbital angular momentum with high-order laguerre-gaussian modes," *Phys. Rev. A*, vol. 56, p. 4193, 1997.

[21] M. A. Bandres and J. C. Gutiérrez-Vega, "Ince-gaussian beams," *Opt. Lett.*, vol. 29, p. 144, 2004.

[22] V. V. Kotlyar, R. V. Skidanov, S. N. Khonina, and V. A. Soifer, "Hypergeometric modes," *Opt. Lett.*, vol. 32, p. 742, 2007.

[23] J. E. Morris, *Studies of Novel beam shapes and applications to Optical Manipulation*. PhD thesis, University of St. Andrews, 2010.

[24] L. C. Dávila-Romero, D. L. Andrews, and M. Babiker, "A quantum electrodynamics framework for the nonlinear optics of twisted beams," *J. Opt. B. Quantum Semiclass. Opt.*, vol. 4, p. S66, 2002.

[25] S. Allen, H. Touchette, S. Moukouri, Y. M. Vilk, and A. M. S. Tremblay, "Role of symmetry and dimension in pseudogap phenomena," *Phys. Rev. Lett.*, vol. 83, p. 4128, 1999.

[26] M. E. J. Friese, J. Enger, H. Rubinsztein-Dunlop, and N. R. Heckenberg, "Optical angular-momentum transfer to trapped absorbing particles," *Phys. Rev. A*, vol. 54, p. 1593, 1996.

[27] N. B. Simpson, K. Dholakia, L. Allen, and M. J. Padgett, "Mechanical equivalence of spin and orbital angular momentum of light: an optical spanner," *Opt. Lett.*, vol. 22, p. 52, 1997.

[28] J. E. Curtis and D. G. Grier, "Structure of optical vortices," *Phys. Rev. Lett.*, vol. 90, p. 133901, 2003.

[29] A. Jesacher, S. Fürhapter, C. Maurer, S. Bernet, and M. Ritsch-Marte, "Reverse orbiting of microparticles in optical vortices," *Opt. Lett.*, vol. 31, p. 2824, 2006.

[30] S. H. Tao, X. C. Yuan, J. Lin, X. Peng, and H. B. Niu, "Fractional optical vortex beam induced rotation of particles," *Opt. Express*, vol. 13, p. 7726, 2005.

[31] M. Dienerowitz, M. Mazilu, P. J. Reece, T. F. Krauss, and K. Dholakia, "Optical vortex trap for resonant confinement of metal nanoparticles," *Opt. Express*, vol. 16, p. 4991, 2008.

[32] A. Ashkin, "Acceleration and trapping of particles by radiation pressure," *Phys. Rev. Lett.*, vol. 24, p. 156, 1970.

[33] K. T. Gahagan and J. G. A. Swartzlander, "Optical vortex trapping of particles," *Opt. Lett.*, vol. 21, p. 827, 1996.

[34] W. M. Lee, V. Garcés-Chávez, and K. Dholakia, "Interference from multiple trapped colloids in an optical vortex beam," *Opt. Express*, vol. 14, p. 7436, 2006.

[35] N. B. Simpson, D. McGloin, K. Dholakia, L. Allen, and M. J. Padgett, "Optical tweezers with increased axial trapping efficiency," *J. Mod. Opt.*, vol. 45, p. 1943, 1998.

[36] K. S. Lee, S. Choi, and S. K. Kim, "Radiation of spin waves from magnetic vortex cores by their dynamic motion and annhilation processes," *Appl. Phys. Lett.*, vol. 87, p. 192502, 2005.

[37] M. P. Macdonald, L. Paterson, K. Volke-Sepulveda, J. Arlt, W. Sibbett, and K. Dholakia, "Creation and manipulation of three dimensional optically trapped structures," *Science*, vol. 296, p. 1101, 2002.

[38] J. Arlt, M. Macdonald, L. Paterson, W. Sibbett, K. Dholakia, and K. Volke-Sepulveda, "Moving interference patterns created using the angular doppler effect," *Opt. Express*, vol. 10, p. 844, 2002.

[39] C. Cohen-Tannoudji, J. Dupont-Roc, and G. Grynberg, *Photons and Atoms: Introduction to Quantum Electrodynamics*. New York: John Wiley and sons, 1989.

[40] G. Gibson, J. Courtial, and M. J. Padgett, "Free-space information transfer using light beams carrying orbital angular momentum," *Opt. Express*, vol. 12, p. 5448, 2004.

[41] A. Aspect, P. Grangier, and G. Roger, "Experimental tests of realistic local theories via bell's theorem," *Phys. Rev. Lett.*, vol. 47, p. 460, 1981.

[42] A. Mair, A. Vaziri, G. Weihs, and A. Zeilinger, "Entanglement of orbital angular momentum states of photons," *Nature*, vol. 412, p. 3123, 2001.

[43] M. W. Beijersbergen, R. P. C. Coerwinkel, M. Kristensen, and J. P. Woerdman, "Helical wavefronts laser beams produced with a spiral phase plate," *Opt. Commun.*, vol. 112, p. 321, 1994.

[44] N. R. Heckenberg, R. McDuff, C. P. Smith, H. Rubinsztein-Dunlop, and M. J. Wegener, "Laser beams with phase singularities," *Optical and Quantum Electronics*, vol. 24, p. S951, 1992.

[45] T. Ando, Y. Ohtake, N. Matsumoto, T. Inoue, and N. Fukuchi, "Mode purities of laguerregaussian beams generated via complex-amplitude modulation using phase-only spatial light modulators," *Opt. Lett.*, vol. 34, p. 34, 2009.

[46] M. W. Beijersbergen, L. Allen, H. van Der Veen, and J. P. Woerdman, "Astigmatic laser mode convertors and transfer of orbital angular momentum," *Opt. Commun.*, vol. 96, p. 123, 1993.

[47] A. M. Yao and M. Padgett, "Orbital angular momentum: origins, behavior and applications," *Advances in Optics and Photonics*, vol. 3, p. 161, 2011.

[48] S. A. Kennedy, M. J. Szabo, H. Teslow, J. Z. Porterfield, and E. R. I. Abraham, "Creation of laguerre-gaussian laser modes using diffractive optics," *Phys. Rev. A*, vol. 66, p. 043801, 2002.

[49] Y. R. Shen, *The Principles of Nonlinear Optics*. London: John Wiley and Sons, 1984.

[50] W. S. Williams, J. T. Hunt, and W. E. Warren, "Light propagation through large laser systems," *IEEE J. Quantum Electron.*, vol. 17, p. 1727, 1981.

[51] A. M. Rubenchik, M. P. Fedoruk, and S. K. Turitsyn, "Laser beam self-focusing in the atmosphere," *Phys. Rev. Lett.*, vol. 102, p. 233902, 2009.

[52] G. G. Luther, J. V. Moloney, A. C. Newell, and E. M. Wright, "Self-focusing threshold in normally dispersive media," *Opt. Lett.*, vol. 19, p. 862, 1994.

[53] E. G. Hanson, Y. R. Shen, and G. K. L. Wong, "Experimental study of self-focusing in a liquid crystalline medium," *Appl. Phys.*, vol. 14, p. 65, 1977.

[54] S. A. Akhmanov, A. P. Sukhorukov, and R. V. Khokhlov, "Self focusing and diffraction of light in a nonlinear medium," *Sov. Phys. Usp.*, vol. 10, p. 609, 1968.

[55] R. Y. Chiao, E. Garmire, and C. H. Townes, "Self trapping of optical beams," *Phys. Rev. Lett.*, vol. 13, p. 479, 1964.

[56] S. D. Patil, M. V. Takale, and M. B. Dongare, "Propagation of hermite-cosh-gaussian laser beams in n-InSb," *Opt. Commun.*, vol. 281, p. 4776, 2008.

[57] S. D. Patil, S. T. Navare, M. V. Takale, and M. B. Dongare, "Self-focusing of cosh-gaussian laser beams in a parabolic medium with linear absorption," *Opt. Laser Eng.*, vol. 47, p. 604, 2009.

[58] A. Thakur and J. Berakdar, "Self-focusing and defocusing of twisted light in non-linear media," *Opt. Express*, vol. 18, p. 27691, 2010.

[59] N. Bloembergen, *Nonlinear Optics*. London: World Scientific, 1996.

[60] M. S. Sodha, A. K. Ghatak, and V. K. Tripathi, *Self-Focusing of Laser Beams in Dielectrics, Plasmas and Semiconductors*. New Delhi, India: Tata McGraw-Hill, 1974.

[61] R. Chiao, E. Garmire, and C. Townes, "Self trapping of optical beams," *Phys. Rev. Lett.*, vol. 13, p. 479, 1964.

[62] G. Molina-Terriza, J. P. Torres, and L. Torner, "Twisted photons," *Nat. Phys.*, vol. 3, p. 305, 2007.

[63] S. Fürhapter, A. Jesacher, S. Bernet, and M. Ritsch-Marte, "Spiral phase contrast imaging in microscopy," *Opt. Express*, vol. 13, p. 689, 2005.

[64] A. T. O'Neil, I. MacVicar, L. Allen, and M. Padgett, "Intrinsic and extrinsic nature of the orbital angular momentum of a light beam," *Phys. Rev. Lett.*, vol. 88, p. 053601, 2002.

[65] A. T. O'Neil and M. J. Padgett, "Three-dimensional optical confinement of micron-sized metal particles and the de-coupling of the spin and orbital angular momentum within an optical spanner," *Opt. Commun.*, vol. 185, p. 139, 2000.

[66] M. P. MacDonald, L. Paterson, W. Sibbett, K. Dholakia, and P. Bryant, "Trapping and manipulation of low-index particles in a two-dimensional interferometric optical trap," *Opt. Lett.*, vol. 26, p. 863, 2001.

[67] G. F. Quinteiro and J. Berakdar, "Electric currents induced by twisted light in quantum rings," *Opt. Express*, vol. 17, p. 20465, 2009.

[68] G. F. Quinteiro and P. I. Tamborenea, "Twisted-light-induced optical transitions in semiconductors: Free-carrier quantum kinetics," *Phys. Rev. B*, vol. 82, p. 125207, 2010.

[69] G. F. Quinteiro, P. I. Tamborenea, and J. Berakdar, "Orbital and spin dynamics of intraband electrons in quantum rings driven by twisted light," *Opt. Express*, vol. 19, p. 26733, 2011.

[70] A. Thakur and J. Berakdar, "Reflection and transmission of twisted light at phase conjugated interfaces," *Opt. Express*, vol. 20, p. 1301, 2012.

[71] R. A. Fischer, *Optical Phase Conjugation*. New York, USA: Academic Press, Inc., 1983.

[72] B. Y. Zel'dovich, N. F. Pilipetsky, and V. V. Shkunov, *Principles of Phase Conjugation*. Berlin: Springer, 1985.

[73] G. S. He, "Optical phase conjugation: principles, techniques, and applications," *Prog. Quantum Electron.*, vol. 26, p. 131, 2002.

[74] P. V. Polyanskiĭ and K. V. Fel'de, "Static holographic phase conjugation of vortex beams," *Opt. Spectrosc.*, vol. 98, p. 913, 2005.

[75] I. G. Marienko, M. S. Soskin, and M. V. Vasnetsov, "Phase conjugation of wavefronts containing phase singularities," *Proc. SPIE*, vol. 3487, p. 39, 1998.

[76] G. C. Valley, M. B. Klein, R. A. Mullen, D. Rytz, and B. Wechsler, "Photo refractive materials," *Ann. Rev. Mater. Sci.*, vol. 18, p. 165, 1988.

[77] T. Geethakrishnan and P. K. Palanisamy, "Optical phase-conjugation in erioglaucine dye-doped thin films," *Pranama-J. Phys.*, vol. 66, p. 473, 2008.

[78] R. K. Jain and R. C. Lind, "Degenerate four-wave mixing in semiconductor-doped glasses," *J. Opt. Soc. Am.*, vol. 73, p. 647, 1983.

[79] T. Bach, K. Nawata, M. Jazbinšek, T. Omatsu, and P. Günter, "Optical phase conjugation of picosecond pulses at 1.06 μm in $Sn_2P_2S_6$: Te for wavefront correction in high-power Nd-doped amplifier systems," *Opt. Express*, vol. 18, p. 87, 2010.

[80] R. S. Cudney and M. Kaczmarek, "Optical poling in Rh : $BaTiO_3$," *Photorefractive Effects, Materials and Devices (PEMD)*, vol. 62, p. 485, 2001.

[81] R. W. Hellwarth, "Generation of time-reversed wave fronts by nonlinear refraction," *J. Opt. Soc. Am.*, vol. 67, p. 1, 1977.

[82] D. M. Bloom and G. C. Bjorklund, "Conjugate wave-front generation and image reconstruction by four-wave mixing," *Appl. Phys. Lett.*, vol. 31, p. 592, 1977.

[83] O. Y. Nosach, B. Y. Zel'dovich, V. I. Popovichev, V. V. Ragul'skii, and F. S. Faisullov, "Cancellation of phase distortions in an amplifying medium with a 'brillouin mirror'," *Sov. Phys. JETP Lett.*, vol. 16, p. 435, 1972.

[84] V. G. Koptev, A. M. Lazaruk, I. P. Petrovich, and A. S. Rubanov, "Wavefront inversion in superradiance," *JETP Lett.*, vol. 28, p. 434, 1978.

[85] G. S. He, Y. Cui, M. Yoshida, and P. N. Prasad, "Phase-conjugate backward stimulated emission from a two-photon-pumped lasing medium," *Opt. Lett.*, vol. 22, p. 10, 1997.

[86] G. S. He and S. H. Liu, *Physics of Non-linear Optics*. Singapore: World Scientific, 1999.

[87] G. Martin and R. W. Hellwarth, "Infrared-to-optical image conversion by bragg reflection from thermally induced index gratings," *Appl. Phys. Lett.*, vol. 34, p. 371, 1979.

[88] V. Wang and C. R. Giuliano, "Correction of phase aberrations via stimulated brillouin scattering," *Opt. Lett.*, vol. 2, p. 4, 1978.

[89] G. S. He, D. Liu, and S. H. Liu, "A new physical explanation of producing phase-conjugate wave process in backward stimulated scattering," *Bull. Am. Phys. Soc.*, vol. 30, p. 1800, 1985.

[90] G. S. He, D. Liu, and S. H. Liu, "New physical explanation of phase-conjugate wave generation in backward stimulated scattering," *Chin. Phys. Lasers*, vol. 13, p. 713, 1986.

[91] M. Born and E. Wolf, *Principles of Optics, 6th Edition*. London: Pergamon, 1983.

[92] W. Nasalki, *Optical Beams at Dielectric Interfaces-Fundamentals*. Warszawa: Institute of Fundamental Technological Research Polish Academy of Sciences, 2007.

[93] W. Szabelak and W. Nasalski, "Transmission of elegant laguerre-gaussian beams at a dielectric interfacenumerical simulations," *Bulletin of the Polish Academy of Sciences: Technical Sciences*, vol. 57, p. 181, 2009.

[94] W. Nasalski, "Polarization versus spatial characteristics of optical beams at a planar isotropic interface," *Phys. Rev. E*, vol. 74, p. 056613, 2006.

[95] J. L. Thomas and R. Marchiano, "Pseudo angular momentum and topological charge conservation for nonlinear acoustical vortices," *Phys. Rev. Lett.*, vol. 91, p. 244302, 2003.

[96] P. N. Lebedev, "Experimental examination of light pressure," *Ann. der Physik*, vol. 6, p. 433, 1901.

[97] A. E. Siegmann, *Lasers*. CA, USA: University Science Book, Mill-Valley, 1986.

[98] V. G. Fedoseyev, "Transformation of the orbital angular momentum at the reflection and transmission of a light beam on a plane interface," *J. Phys A: Math. Theor.*, vol. 41, p. 505202, 2008.

[99] V. G. Fedoseyev, "Reflection of the light beam carrying orbital angular momentum from a lossy medium," *Phys. Lett. A*, vol. 372, p. 2527, 2008.

[100] D. Jackson, *Classical Electrodynamics and Third edition*. London: John Wiley and Sons, 1967.

[101] E. M. Liftshitz, L. P. Pitaevskii, and V. B. Berestetskii, *Quantum Electrodynamics, Landau and Liftshitz Course of Theoretical physics, Vol. 4*. Oxford: Butterworth-Heineman, 1982.

[102] D. Mugnai and P. Spalla, "Electromagnetic propagation of bessel-like localized waves in the presence of absorbing media," *Opt. Commun.*, vol. 282, p. 4668, 2009.

[103] D. Mugnai, "Propagation of bessel beams from a dielectric to a conducting medium," *Appl. Opt.*, vol. 50, p. 2654, 2011.

[104] Y. Kitagawa, T. Matsumoto, T. Minamihata, K. Sawai, K. Matsuo, K. Mima, K. Nishihara, H. Azechi, K. A. Tanaka, H. Takabe, and S. Nakai, "Beat-wave excitation of plasma wave and observation of accelerated electrons," *Phys. Rev. Lett.*, vol. 68, p. 48, 1992.

[105] D. Umstadter, J. K. Kim, and E. Dodd, "Laser injection of ultrashort electron pulses into wakefield plasma waves," *Phys. Rev. Lett.*, vol. 76, p. 2073, 1996.

[106] T. Nubbemeyer, K. Gorling, A. Saenz, U. Eichmann, and W. Sandner, "Strong-field tunneling without ionization," *Phys. Rev. Lett.*, vol. 101, p. 233001, 2008.

[107] S. Chu, "The manipulation of neutral particles," *Rev. Mod. Phys.*, vol. 70, p. 685, 1998.

[108] H. Stapelfeldt, H. Sakai, E. Constant, and P. B. Corkum, "Deflection of neutral molecules using the nonresonant dipole force," *Phys. Rev. Lett.*, vol. 79, p. 2787, 1997.

[109] R. Fulton, A. I. Bishop, and P. F. Barker, "Optical stark decelerator for molecules," *Phys. Rev. Lett.*, vol. 93, p. 243004, 2004.

[110] F. Fabre, G. Petite, P. Agostini, and M. Clement, "Multiphoton above-threshold ionisation of xenon at 0.53 and 1.06 μm," *J. Phys. B: At. Mol. Phys.*, vol. 15, p. 1353, 1982.

[111] G. Petit, F. Fabre, and P. Agostini, "Nonresonant multiphoton ionization of cesium in strong fields: Angular distributions and above-threshold ionization," *Phys. Rev. A*, vol. 29, p. 2677, 1984.

[112] Y. Gontier and M. Trahin, "Energetic electron generation by multiphoton absorption," *J. Phys. B: At. Mol. Phys.*, vol. 13, p. 4383, 1980.

[113] S. H. Lin, A. A. Villaeys, and Y. Fujimura, *Advances in Multiphoton processes and Spectroscopy*. Singapore: Vol. 18, World Scientific, 2008.

[114] P. B. Corkum, "Plasma perspective on strong field multiphoton ionization," *Phys. Rev. Lett.*, vol. 71, p. 1994, 1993.

[115] H. A. H. Boot and R. B. R. S. Harvie, "Charged particles in a non-uniform radio-frequency field," *Nature*, vol. 180, p. 1187, 1957.

[116] V. Gapanov and M. A. Miller, "Potential wells for charged particles in a high frequency electromagnetic field," *J. Exp. Theor. Phys.*, vol. 34, p. 242, 1958.

[117] H. A. H. Boot, S. A. Self, , and R. B. . R. S. Harvie, "Containment of a fully ionized plasma by radio-frequency fields," *J. Electr. Control*, vol. 4, p. 434, 1958.

[118] N. J. Phillips and J. J. Sanderson, "Trapping of electrons in a spatially inhomogeneoeus laser beam," *Phys. Lett.*, vol. 21, p. 533, 1966.

[119] T. W. B. Kibble, "Refraction of electron beams by intense electromagnetic waves," *Phys. Rev. Lett.*, vol. 16, p. 1054, 1966.

[120] T. W. B. Kibble, "Mutual refraction of electrons and photons," *Phys. Rev.*, vol. 150, p. 1060, 1966.

[121] M. J. Hollis, "Multiphoton ionization and em field gradient forces," *Opt. Commun.*, vol. 25, p. 395, 1978.

[122] R. R. Freeman, T. J. McIlrath, P. H. Bucksbaum, and M. Bashkansky, "Ponderomotive effects on angular distributions of photoelectrons," *Phys. Rev. Lett.*, vol. 58, p. 526, 1987.

[123] P. H. Bucksbaum, M. Bashkansky, and T. J. McIlrath, "Scattering of electrons by intense coherent light," *Phys. Rev. Lett.*, vol. 58, p. 349, 1987.

[124] U. Mohideen, H. W. K. Tom, R. R. Freeman, J. Bokor, and P. H. Bucksbaum, "Interaction of free electrons with an intense focused laser pulse in gaussian and conical axicon geometries," *J. Opt. Soc. Am. B*, vol. 9, p. 2190, 1992.

[125] C. I. Moore, "Confinement of electrons to the centre of a laser focus via the ponderomotive potential," *J. Mod. Opt.*, vol. 39, p. 2171, 1992.

[126] Q. Kong, S. Miyazaki, S. Kawata, K. Miyauchi, K. Nakajima, S. Masuda, N. Miyanaga, and Y. K. Ho, "Electron bunch acceleration and trapping by the ponderomotive force of an intense short-pulse laser," *Phys. Plasmas*, vol. 10, p. 4605, 2003.

[127] P. W. Smorenburg, J. H. M. Kanters, A. Lassise, G. J. H. Brussaard, L. P. J. Kamp, and O. J. Luiten, "Polarization-dependent ponderomotive gradient force in a standing wave," *Phys. Rev. A*, vol. 83, p. 063810, 2011.

[128] A. Ashkin, "Trapping of atoms by resonance radiation pressure," *Phys. Rev. Lett.*, vol. 40, p. 729, 1978.

[129] A. Ashkin, J. M. Dziedzic, J. E. Bjorkholm, and S. Chu, "Observation of a single-beam gradient force optical trap for dielectrical particles," *Opt. Lett.*, vol. 11, p. 288, 1986.

[130] A. Ashkin and J. M. Dziedzic, "Optical trapping and manipulation of viruses and bacteria," *Science*, vol. 235, p. 1517, 1987.

[131] A. Ashkin, J. M. Dziedzic, and T. Yamane, "Optical trapping and manipulation of single cells using infrared laser beams," *Nature*, vol. 330, p. 769, 1987.

[132] A. Ashkin, J. M. Dziedzic, J. E. Bjorkholm, and S. Chu, "Observation of a single-beam gradient force optical trap for dielectric particles," *Opt. Lett.*, vol. 11, p. 288, 1986.

[133] D. G. Grier, "A revolution in optical manipulation," *Nature*, vol. 424, p. 810, 2003.

[134] A. Ashkin, "Forces of a single-beam gradient laser trap on a dielectric sphere in the ray optics regime," *Biophys. J.*, vol. 61, p. 569, 1992.

[135] K. C. Neuman and S. M. Block, "Optical trapping," *Rev. Sci. Instrum.*, vol. 75, p. 2787, 2004.

[136] E. Almaas and I. Brevik, "Radiation forces on a micrometer-sized sphere in an evanescent field," *J. Opt. Soc. Am. B*, vol. 12, p. 2429, 1995.

[137] J. P. Barton, "Internal and near surface electromagnetic fields for a spheroidal with arbitrary illumination," *Appl. Opt.*, vol. 34, p. 5542, 1995.

[138] J. P. Barton and D. R. Alexander, "Fifth-order corrected electromagnetic field components for a fundamental gaussian beam," *J. Appl. Phys.*, vol. 66, p. 2800, 1989.

[139] J. P. Barton, D. R. Alexander, and S. A. Schaub, "Theoretical determination of net radiation and torque for a spherical particle illuminated by a focused laser beam," *J. Appl. Phys.*, vol. 66, p. 4594, 1989.

[140] P. Zemánek, A. Jonáš, and M. Liška, "Simplified description of optical forces acting on a nanoparticle in the gaussian standing wave," *J. Opt. Soc. Am. A*, vol. 19, p. 1025, 2002.

[141] D. L. Andrews, *Structured light and its application*. California: Elsevier, 2007.

[142] H. Rubinsztein-Dunlop, T. A. Nieminen, M. E. J. Friese, and N. R. Heckenberg, "Optical trapping of absorbing particles," *Advances in Quantum Chemistry*, vol. 30, p. 469, 1998.

[143] J. E. Molloy and M. Padgett, "Light's action: optical tweezers," *Contemparary Physics*, vol. 43, p. 241, 2002.

[144] K. T. Gahagan and J. G. A. Swartzlander, "Trapping of low index microparticles in an optical vortex," *J. Opt. Soc. Am. B*, vol. 15, p. 524, 1998.

[145] A. T. O'Neil and M. J. Padgett, "Axial and lateral trapping efficiency of laguerre-gaussian modes in inverted optical tweezers," *Opt. Commun.*, vol. 193, p. 45, 2001.

[146] H. S. Chai and L. G. Wang, "Improvement of optical trapping effect by using the focused high order laguerre gaussian beams," *Micron*, vol. 43, p. 887, 2012.

[147] M. Babiker, C. R. Bennett, D. L. Andrews, and L. C. D. Romero, "Orbital angular momentum exchange in the interaction of twisted light with molecules," *Phys. Rev. Lett.*, vol. 89, p. 143601, 2002.

[148] S. Lloyd, M. Babiker, and J. Yuan, "Quantized orbital angular momentum transfer and magnetic dichroism in the interaction of electron vortices with matter," *Phys. Rev. Lett.*, vol. 108, p. 74802, 2012.

[149] M. Abramowitz and I. A. Stegun, *Handbook of mathematical functions*. Washington D. C.: National Bureau of Standards, 1964.

Erklärung

Hiermit erkläre ich, dass ich diese Arbeit selbständig und ohne fremde Hilfe verfaßt, andere als die von mir angegebenen Quellen und Hilfsmittel nicht benutzt und die den benutzen Werken wörtlich oder inhaltlich entnommenen Stellen als solche kenntlich gemacht habe.

Eine Anmeldung der Promotionsabsicht habe ich an keiner anderen Fakultät einer Universität oder Hochschule beantragt.

Anita Thakur

Acknowledgement

This is a matter of great pleasure for me to place on record my heartiest gratitude to all the people who helped me to bring this work to completion. First of all, I would like to express my profound thanks to my supervisor **Prof. Dr. Jamal Berakdar** for his continuous support, encouragement, guidance, ideas and valuable advices. I am indeed indebted to him for giving me the freedom to explore the interesting field of **Twisted Light** and for motivation at utmost needed time.

I would like to acknowledge all the present and former colleagues of the theory group "Non-equilibrium many-body systems" at Martin Luther University. My special thanks to **Dr. Andrey Moskalenko** for his ideas and suggestions over scientific issues, critical comments on thesis work, discussions on the interesting findings related to twisted light and would like to acknowledge for his cooperation on the work of optical trapping of neutral atoms (Chapter 5). I would also like to express my sincere thanks to my officemate **Dr. Yaroslav Pavlyukh** for his critical comments in group seminars, for resolving computer related issues and for all scientific or non-scientific discussions. I would also like to take this opportunity to deeply thanks one of my other colleague **Dr. Koray Koksal** for his guidance while dealing with Mathematica and for his willingness to listen me on all the matters. I would definitely miss his company over the coffee time. I also thanks **Dr. Berlinson Napitu** for his encouragement and appreciation on my work. I also wish to acknowledge **Dr. Guillermo Quinteiro** for sharing his knowledge on twisted light with me at the initial stage of my Ph.D. I am also grateful to **Dr. Levan Chotorlishvili**, **Dr. Alexander Sukhov**, **Dr. Chenglong Jia**, **Dr. Zhen Gang Zhu** , **Dr. Ahsaan**, **Dr. Nicholas Sedlmayr**, **Dr. Oleg Kidun**, **Dr. V. Prasad**, **Johannes Hahn**, **Michael Schüler**, **Jonas Wätzel** and **Prof. Dr. Vitalii Dugaev** for creating a working and friendly atmosphere over the past three years.

My sincere thanks to **Prof. Dr. Jürgen Kirschner** and **Prof. Dr. Eberhard Gross** for providing me financial support to carry out my work as a PhD student at **International Max Planck Research School (IMPRS)**. I would also like to pay my gratitude to all the members of **Administration department**, **Mrs. Ina Goffin** from theory department and librarian **Mrs. Julia Ducke** at Max Planck Institute of Microstructure Physics for their rendered help which i received from them.

Additionally, I would like to thank all my colleagues at the IMPRS for giving interesting talks during the IMPRS seminars and workshops. My special thanks to all the former coordinators of the Research School **Dr. Ksenia Boldyreva**, **Mrs. Maria Santo Quiles**, the current coordinator of IMPRS and my Ph.D mentor **Dr. Arthur Ernst** for their support. Here, I would also like to appreciate **Prof. Dr. Miles Padgett**

& his group for allowing me to visit Optics group at University of Glasgow, Scotland and specially **Dr.Johannes Courtial** for his help during my stay over there.

My greatest thanks to all my **Halle Indian friends** for their constant support and care especially my dear friend **Shilpa Kancherla (Shillu)** for always being with me. Guys, many thanks from bottom of my heart without you all, this journey would not have been possible. And I would be immensely sad while leaving you all!!!

Last but not least my whole family deserve the warmest gratitude, my parents, my brothers and my darling elder sister **Mrs. Geeta Negi** for their compassion, pray and unwavering support over the years. I also wish to express the memory of my dearest uncle **Late Sh. Hansraj Arora** who always supported me for higher education yet could not able to see the end of this work. I also thanks my dear Aunt **Smt. Raj Arora and her two daughters** without whom I would not be at the position where I am today. I also thank those whom I could not explicitly mention here. In the end, all of the above, I want to thank Almighty for illuminating the path of knowledge and for the strength to face all the challenges in my life!!!

Curriculum Vitae

Personal details

- Name: Anita Thakur
- Date of Birth: 30-04-1984
- Place of Birth: Jalandhar City (Punjab), India
- Nationality: Indian
- Sex: Female
- Marital Status: Single

Education & Work Experience

- **2000-2002**: B.S.F Senior Secondary School, Jalandhar City (Punjab), India
- **2002-2005**: Bachelor of Science (Physics), Lyallpur Khalsa College, Jalandhar City (Punjab), India
- **2005-2006**: Bachelor of Education, M.G.N College of Education, Jalandhar City (Punjab), India
- **2006-2008**: Master of Science (Physics), Dr. B.R. Ambedkar National Institute of Technology, Jalandhar (Punjab), India
  Master Thesis: "Theoretical approach to self-focusing by paraxial ray approximation"
  Supervisor: Prof. Dr. Arvinder Singh
- **2008-2009**: Teaching Experience (as a Lecturer), Lovely Professional University, Phagwara (Punjab), India
- **2009-2012**: Ph.D at the International Max Planck Research School (IMPRS), Max Planck Institute of Microstructure Physics, Halle (Saale), Germany
  Ph.D Thesis: "Twisted light: Propagation properties and particle dynamics"
  Supervisor: Prof. Dr. Jamal Berakdar.

List of Publications

- A.Thakur and J.Berakdar, “Self-focusing and de-focusing of twisted light in non-linear media”, *Optics Express*, Vol.18, **No.**26, 27691, 2010.
- A.Thakur and J.Berakdar, “Reflection and transmission of twisted light through phase conjugated interface”, *Optics Express*, Vol.20, **No.**2, 1301, 2012.

Further Publications: A.Thakur and J.Berakdar, “Optical trapping, guiding and acceleration of neutral atoms with structured light”, in preparation, *Optics Letters*, 2013.

Conference Contributions

- A. Thakur and J. Berakdar, “Self-focusing of electromagnetic beams in a non-linear medium”, DPG-Spring Meeting, Regensburg, Germany, March 21 – 26, 2010, *Poster*.
- A. Thakur, “Self-focusing of twisted light”, International Max Planck Research School Workshop, Grimma, Germany, July 15 – 16, 2010, *Talk*.
- A. Thakur and J. Berakdar, “Reflection and transmission of twisted light through phase conjugated interface”, International Conference on ”Photon 10”, Southampton, U.K, August 23 – 26, 2010, *Poster*.
- A. Thakur, “Propagation properties of twisted light”, Optics Group (Prof. Miles Padgett), University of Glasgow, Scotland, September 2, 2010, *Talk*.
- A.Thakur and J.Berakdar, “Self-focusing and de-focusing of twisted light in non-linear media”, International Conference, 42^{nd} Annual Meeting of the American Physical Society (APS) Division of Atomic, Molecular and Optical Physics, Atlanta, USA, June 13 – 16, 2011, *Poster*.
- A.Thakur, “Particle dynamics with twisted light”, International Max Planck Research School Workshop, HalberStadt, Germany, October 15 – 16, 2011, *Talk*.